Fabrication and characterization of permalloy nanostructures

Jeffrey R Bates
Department of Physics
McGill University

August 2013

A thesis submitted to McGill University in partial fulfilment of the requirements of the degree of Ph.D.

Abstract

The range of applied magnetic fields at which an array of magnetic nanostructures reverses magnetization direction is known as the switching field distribution (SFD). Factors that influence the SFD of nanomagnets include edge roughness, aspect ratio, crystallographic orientation, interactions with neighbouring nanomagnets, and temperature. Applications of nanomagnets such as magnetic random access memory and magnetic quantum cellular automata require a narrow, controlled SFD for reliable operation. To achieve such control, the dominant factors influencing the distribution must be known and are studied in this thesis. To this end, indexed arrays of permalloy $(Ni_{81}Fe_{19})$ nanomagnets are made by electron beam evaporation of permalloy through focused ion beam milled nanostencils on electron transparent silicon nitride membranes. The SFD of these structures is studied by magnetic force microscopy, while chemical and structural characterization of the same structures is performed by transmission electron microscopy.

Focused ion beam milled nanostencils are found to influence the growth and structure, chemical composition and subsequently the magnetization behavior of deposited permalloy nanomagnets. This influence is attributed to implantation of gallium ions from the focused ion beam stencil milling process. By thinning the nanostencil using a reactive ion etch, the detrimental influence on magnetic behavior is reduced. A strong correlation is not found between SFD and edge roughness or finite length shape anisotropy factor (perhaps due to the small number of nanostructures investigated), but experiments suggest that increased edge roughness may increase the switching field at constant finite length shape anisotropy factor.

Finally a new technique designed to allow for the measurement of the relative switching field of an array of nanomagnets in a single image is presented. This technique involves applying an AC magnetic field that is larger than the nanomagnet coercivity. The phase between the applied field and the resonant frequency shift of the magnetic cantilever should give a measurement of the coercivity and thus the switching field. By looking at the standard deviation of this signal one should also be able to determine the SFD of an individual nanomagnet. This technique was implemented and preliminary results are presented.

Résumé

La plage de champs magnétiques appliqués pour lesquels un ensemble de nanostructures magnétiques renverse la direction de leur magnétisation est connue sous le nom de distribution du champ de renversement (switching field distribution, SFD). Plusieurs facteurs influencent la SFD des nano aimants, tels que la rugosité des bords, le rapport d'aspect, l'orientation cristallographique, les interactions avec les nano aimants avoisinants et la température. Certaines applications potentielles des nano aimants, notamment la mémoire vive magnétique et les automates cellulaires quantiques magnétiques, nécessitent une SFD qui soit étroite et contrôlée pour assurer une opération fiable. Pour atteindre ce contrôle, les facteurs dominants influençant cette distribution doivent être connus. À cette fin, un arrangement indexé de nano aimants de permalloy $(Ni_{81}Fe_{19})$ est fabriqué le déposant par évaporation par faisceau d'électron au travers d'un nano masque usiné par sonde ionique focalisée (focused ion beam, FIB) sur une membrane de nitrure de silicium transparente aux électrons. Le SFD de ces structures est étudié par microscopie à force magnétique, tandis que la structure et la composition chimique sont caractérisées par microscopie électronique en transmission.

Il est montré que les nano masques usinés par sonde ionique focalisée influencent la structure de la croissance, la composition chimique et le comportement magnétique des nano aimants de permalloy. Cette influence est attribuée à l'implantation d'ions de gallium provenant du processus d'usinage par sonde ionique focalisée. En amincissant le nano masque par gravure ionique réactive, l'influence négative sur le comportement magnétique est réduite. Une forte corrélation n'est pas observée entre le SFD et la rugosité des bords ou le rapport d'aspect (peut-être dû à un échantillonnage limité), mais les expérience suggèrent qu'une augmentation de la rugosité des bords augmente le champ de renversement pour un rapport d'aspect constant.

Finalement, une nouvelle technique, permettant la mesure du champ de renversement relatif d'un ensemble de nano aimants en une seule image, est présentée. Cette technique nécessite l'application d'un champ magnétique alternatif

qui soit plus large que le champ coercitif du nano aimant. La différence de phase entre le champ appliqué et le changement de fréquence de résonance du cantilever magnétique donne une mesure du champ coercitif. Cette technique a été implémentée et des résultats préliminaires sont présentés.

Acknowledgements

I thank my supervisor Peter Grutter for his support, encouragement, and guidance. He provided me with many opportunities, for which I am grateful. I thank Yoichi Miyahara for all of the help that he gave me throughout my time at McGill. It was a pleasure to work with you. I am especially lucky to have worked in such an amazing group. I have learned a great deal from our many discussions, and I appreciate the positive impact you had on my time at McGill. I'd also like to thank Oscar Iglesias-Freire, Aleks Labuda, Jacob Burgess, and Cristian Cojocaru for the impact you had on my research. I really enjoyed working with you.

I was also very fortunate to be able to learn from many people from the McGill community. Thanks to Pascal Bourseguin for teaching me everything that I know about machining. Thanks to David Liu for finding time for my samples and teaching me how to use the TEM. Thanks to Robert Gagnon for all of your help throughout my PhD, your support has been invaluable. Thanks to Juan Gallego for being patient, answering my many computer questions. Thank you to the members of the microfabrication laboratory at McGill Nanotools facility, as well as at the microfabrication laboratory at École polytechnique de Montréal for your help and support. I acknowledge NSERC for their financial support.

I would like to thank all the members, past and present, of the intramural physics hockey and soccer teams. It was a pleasure coaching and playing with you. Thanks also to all of the people that made Montreal such a fun place to be including Kevin, Sarah, Justin, Becky, Olivia, Ashley, James, Audrey, Vance, Bob, Jon, Gil, Jon, Jess, Dylan, Jody and Phil.

I am so lucky to have such caring parents. I know I would not be where I am today without their love and support. I wish my Mom was still here to read this. Thanks to my brother Tim for always pushing me to be better, and for being such a great friend. I'd also like to thank the rest of my family and my in-laws for their support. Finally, I'd like to thank my wife, Jessica Topple. I am so lucky to have married my best friend. I couldn't have done this without your love, support and encouragement.

Statement of Originality

The author, JB, claims the following aspects of the work contained herein constitute original scholarship and an advancement of knowledge. Some results have led to publications, noted with corresponding citations. Specific contributions include:

- A home built magnetic force microscope was updated to apply in-plane magnetic fields without heating the sample in vacuum. A new microscope head was built with a fiber walker to better control the fiber-cantilever separation under vacuum. An insulating Delrin microscope head and a high frequency AC inductor coil were fabricated so that a variable field magnetic force microscope technique could be tested.
- Unique data of the switching field of an array of permalloy nanomagnets was compared to the finite length shape anisotropy factor and edge roughness measured using a transmission electron microscope. Magnetization reversal simulations were also made to test the influence of large defects using object oriented micromagnetic framework.
- The effect of using silicon nitride stencil masks made by focused ion beam milling on permalloy nanostructures was investigated [J.R. Bates, Y. Miyahara, J.A.J. Burgess, O. Iglesias-Freire and P. Grutter, *Effect of using stencil masks made by focused ion beam milling on permalloy ($Ni_{81}Fe_{19}$) nanostructures*. Nanotechnology 24 115301 (2013)].
- A magnetic force microscopy tip was investigated that caused artifacts in the dissipation and frequency shift channels in a magnetic force microscopy experiment. [O. Iglesias-Freire, J.R. Bates, Y. Miyahara, A. Asenjo and P. Grutter, *Tip-induced artifacts in magnetic force microscopy images*. Applied Physics Letters 102 022417 (2013)].

Contributions of Co-authors

The contributions of all parties in the collaborative works presented in this thesis are as follows:

- All instrumentation and microscope design was done with the help of Dr. Y. Miyahara.
- The general design of the apparatus, discussed in appendix A, that applied a DC magnetic field was done by Dr. J. Sandther and Dr. H. Bleuler from the Institute de microtechnique, École Polytechnique Federale de Lausanne.
- Nanostructures made by sputtering permalloy though FIB milled nanostencils (shown in chapter 1) were fabricated by Dr. C.V. Cojocaru.
- For the FIB stencil mask paper discussed in chapter 2, this author made all samples except one of the two control samples, and performed AFM, MFM, KPFM measurements. The author also discovered that the FIB milled process was causing the change in the structure and function of the nanomagents. The author, JB, wrote the manuscript but all co-authors gave feedback, editing, and suggestions during the writing of the article. J.A.J. Burgess fabricated one of the control samples. O. Iglesias-Freire, Dr. Y. Miyahara and Prof. P. Grutter helped in the understanding of the phenomenon. The EELS data was performed at the Canadian Centre for Electron Microscopy at McMaster University.
- Investigations of the effect of cantilever coating on noise in atomic force microscope systems are discussed briefly in section 2.1. [A. Labuda, J.R. Bates and P.H. Grutter, Nanotechnology 23 025503 (2012)]. This author milled the Fresnel lenses on the back of commercially available cantilevers using focused ion beam. A. Labuda did the majority of the work and wrote the manuscript. All authors provided feedback, editing, and suggestion on the manuscript.
- For the artifacts in MFM paper discussed in section 4.1, this author made the samples, shared in the characterization, identified the unique phe-

nomenon observed, and performed analysis. O. Iglesias-Freire shared in the characterization, analysis, and the simulations as well as wrote the manuscript. All authors provided feedback, editing, and suggestions to the manuscript, and helped in the characterization and analysis of the phenomenon.

Contents

List of Figures

List of Tables

1

Introduction

1.1 Motivation

The study of magnetic nanostructures is important for technological applications such as magnetoelectronics [1], magnetic tunnel junctions (MTJ) [2–5], magnetic random access memory (MRAM) [6], and magnetic quantum cellular automata (MQCA) [7–10].

MRAM is a non-volatile RAM that stores information (bits) in the magnetization direction of magnetic nanostructures. A bit can be written to a magnetic nanostructure (changing the magnetization direction) using the induced magnetic field from a series of current carrying wires. The magnetic field at which the magnetization direction changes must be controlled to allow reliable mass production of MRAM components. To improve error tolerance limits for MRAM devices, the distribution of switching fields of all components must be narrowed [11].

MQCA uses identically designed magnetic nanostructures to transmit information (bits) and perform logic operations on these bits. To transmit information, chains of nanomagnets are magnetically coupled [7, 10]. Using an input bit and a clocking magnetic field, information can be transmitted down a chain of nanomagnets. Similarly, logic gates can be made using a specific arrangement of nanomagnets that are magnetically coupled [10]. To properly design the coupling between nanomagnets and avoid errors, the field at which the magnetic nanostructures reverse magnetization must be well known and have a narrow distribution [10].

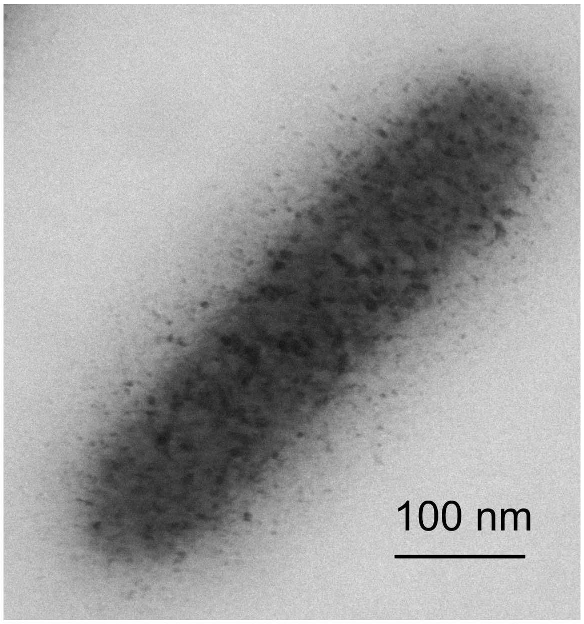

Figure 1.1: Permalloy ($Ni_{81}Fe_{19}$) nanostructure fabricated by magnetron sputtering permalloy through a focused ion beam (FIB) milled nanostencil. Structure is 20 nm thick, and 480 ± 10 nm by 120 ± 10 nm as measured by half of structure contrast in transmission electron microscopy (TEM). Error is given by length and width at $\pm$ 10% from the midpoint.

A single domain magnetic nanostructure (nanomagnet) made of permalloy ($Ni_{81}Fe_{19}$, which is ferromagnetic), like the one shown in figure 1.1, has a bistable magnetization configuration. It is energetically favorable for the magnetization to be oriented along the long axis of the structure in the plane of the image, resulting in two stable configurations, depending on the magnetization direction. The magnetization direction can be reversed by applying an external magnetic field. Magnetization reversal has two regimes: quantum mechanical tunneling through an energy barrier and classical transition over a barrier [12]. In this thesis, due to the temperature and size of the nanomagnets studied, quantum mechanical tunneling will be neglected and classical barrier transition will be assumed.

The magnetization of a nanomagnet may be simulated as a function of an applied magnetic field, as shown in figure 1.2. The external applied magnetic field at which the nanomagnet reverses its magnetization direction is known as the coercive field (coercivity or switching field) and is labeled H_c. As the magnetization becomes more aligned in the applied magnetic field, it approaches the saturation magnetization, labeled M_s. Permalloy is a particularly interesting material for many applications due to its low coercivity (magnetically soft), meaning that the energy required to reverse magnetization is low.

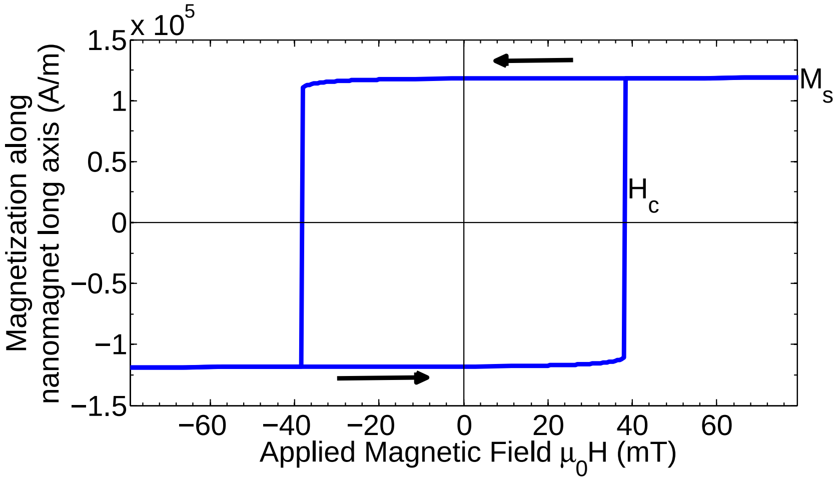

Figure 1.2: Object oriented micromagnetic framework (OOMMF) simulation of a nanomagnet coercivity and saturation magnetization.

An array of nanomagnets that are identically designed will have a switching field distribution (SFD). Figure 1.3 shows a hypothetical curve of magnetization as a function of applied magnetic field (blue) and the corresponding SFD (red) for an array of nanomagnets. The distribution in switching field results in a smoother transition in the total magnetization of the sample when compared to the magnetization reversal of an individual nanomagnet.

Factors affecting the SFD include differences in magnetic nanostructure aspect ratio [13, 14], edge roughness [15–19], temperature [20–22], interactions with neighbours [23], and crystallographic orientation of grains [24]. However, the relative importance of these factors is not generally known. A wider SFD can lead to reduced reliability of devices [25] and therefore the dominant factor influencing SFD warrants further study.

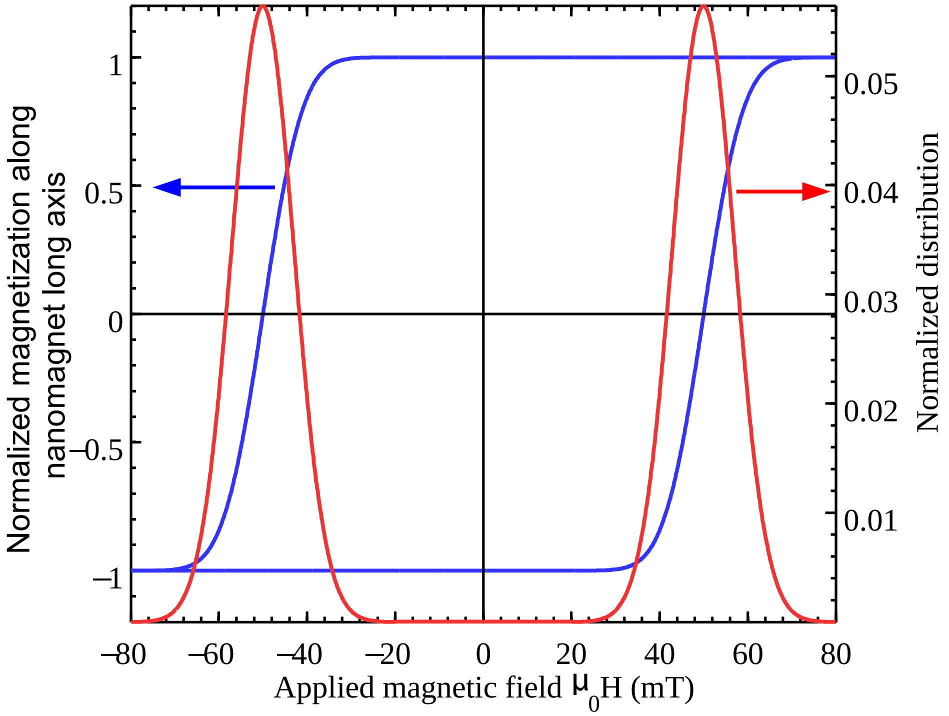

Figure 1.3: Magnetization of a hypothetical array of identically designed nanomagnets. The magnetization of each nanomagnet doesn't reverse at the same external applied field, resulting in the distribution of switching fields.

Although much can be learned from simulations of the switching field, experimental measurements are necessary to account for imperfections such as simulation overestimation of the switching field described by Brown's paradox [26]. This overestimation is possibly due to deviations from the perfect ellipse structure [27], but more likely due to domains being nucleated at lower magnetic fields near defects [28,29].

This thesis includes both experimental data and simulations of arrays of permalloy nanostructures like the one shown in figure 1.1.

1.2 Atomic force microscopy

The SFD of magnetic nanostructures will be characterized using magnetic force microscopy (MFM), a mode of atomic force microscopy (AFM). AFM is a scanning probe microscopy technique where a micron sized cantilever with a sharp tip is brought in close proximity with a sample. Interaction forces lead to a status change of the cantilever, which here is detected by an interferometer. A piezoelectric tube is used to control the tip-sample separation as well as raster scan the sample under the tip. The net interaction force between the tip and sample is kept constant using a feedback loop that adjusts the tip-sample separation as the tip is scanned over the sample. By recording the z position of the sample as a function of the x-y tip position, a topography map of the sample can be obtained.

In contact mode AFM, the cantilever tip is brought into contact with the sample where there is a repulsive interaction. The cantilever deflection is maintained constant during scanning, corresponding to a constant repulsive force between tip and sample.

In dynamic modes of AFM, the cantilever is oscillated at a frequency near or at the first resonant frequency, which for a rectangular cantilever is given by

[30,31],

$$f_0 = 0.162\frac{t}{L^2}\sqrt{\frac{E_Y}{\rho}}, \tag{1.1}$$

where t is the thickness of the cantilever, L is the length, E_Y is the Young's modulus of the cantilever and ρ is the density. Higher modes may also be used [32], but won't be discussed further as only the first modes is used in this work. The stiffness (spring constant) k of the cantilever is given by [31],

$$k = \frac{E_Y w t^3}{4L^3}, \tag{1.2}$$

where w is the width of the cantilever.

In tapping mode AFM (a dynamic mode) the cantilever is excited near its resonance frequency. The cantilever tip is then brought close to the sample so that they interact. The interaction causes the cantilever oscillation to be damped, producing a smaller oscillation amplitude. This smaller amplitude is kept constant as the tip is scanned over the sample. Tapping mode is advantageous over contact mode AFM in that it reduces the degradation of the cantilever tip and sample surface [33].

1.2.1 Amplitude modulated AFM

In amplitude modulated AFM (AM-AFM), the cantilever is oscillated near its resonant frequency with a constant drive amplitude. As the cantilever tip is brought close to the sample there is initially an attractive interaction (which will be discussed in detail below), causing the resonant frequency to be reduced as shown in figure 1.4. Because the cantilever is driven at a constant frequency (as

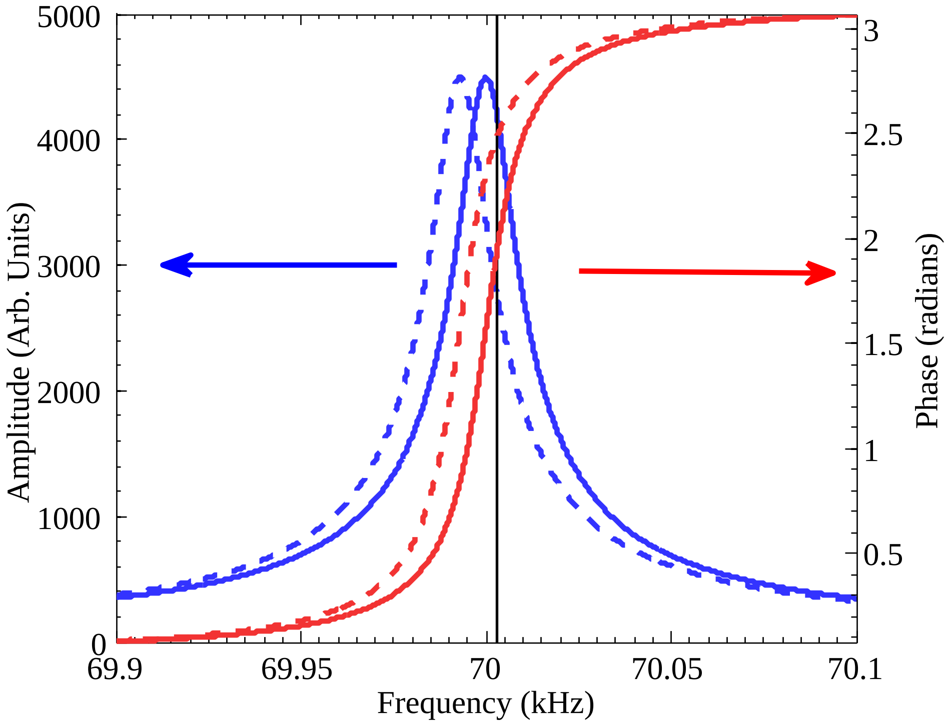

Figure 1.4: Cantilever amplitude and phase as a function of drive frequency for a cantilever with a Q factor of 4500. Solid blue and red line are free oscillation. Dotted lines represent cantilever with an attractive tip-sample interaction. Blue represents the amplitude and red represents the phase.

shown by the vertical black line in figure 1.4), this reduction of resonant frequency causes a reduction in the cantilever oscillation amplitude. This can be measured using a lock-in amplifier or an RMS to DC converter. A feedback loop is used to maintain a constant oscillation amplitude by adjusting the sample height as the cantilever tip is scanned over the sample. This results in a constant tip-sample separation as the tip is scanned. Again, by looking at the height of the sample as a function of x and y cantilever position, a map of the surface topography can be made. The settling time (τ_{AM}) for a change in amplitude to occur in AM-AFM is proportional to [31],

$$\tau_{AM} \propto 2Q/f_0 \tag{1.3}$$

where Q is the quality factor of the cantilever. The signal to noise ratio of AM-AFM can be increased by increasing the Q factor [34], but because of equation 1.3 the tip would be required to scan at extremely slow rates.

1.2.2 Frequency modulated AFM

An alternative to AM-AFM is frequency modulated AFM (FM-AFM) which avoids the quality factor dependence on settling time. As in AM-AFM, an oscillating cantilever is brought close to a sample where there is an interaction between the tip and sample. This interaction causes the cantilever's resonant frequency to change as shown in figure 1.4. A constant frequency shift is maintained by a feedback loop as the sample is raster scanned under the cantilever tip. A map of the sample height as a function of x-y position is obtained and is called the frequency mode atomic force microscopy topography.

For small cantilever oscillations (when compared to the change in the force gradient [35]), the frequency shift is given by [31],

$$\Delta f = \frac{f_o}{2k} k_{ts}, \tag{1.4}$$

where Δf is the frequency shift, k is the cantilever spring constant (defined in equation 1.2) and $k_{ts} = \partial F/\partial z$ is the effective spring constant between the tip and sample which is equal to the force gradient. For larger oscillation amplitudes (where the majority of the tip-sample interaction takes place at only the closest approach of the cantilever), the frequency shift is given by [31],

$$\Delta f(z) = \frac{f_0}{2k} \int_{-A}^{A} k_{ts}(z - q') \frac{\sqrt{A^2 - q'^2}}{\pi A^2/2} dq', \tag{1.5}$$

where A is the oscillation amplitude of the cantilever, z is the tip-sample distance.

The benefit of FM-AFM is that the settling time (τ_{FM}) for a change in frequency to occur is proportional to [31],

$$\tau_{FM} \propto 1/f_0, \tag{1.6}$$

which is independent of quality factor. This allows FM-AFM systems to be operated in vacuum conditions [34] and even at cryogenic temperatures [36]. Such conditions provide vastly improved quality factors, improving the signal to noise ratio while maintaining a reasonable scan speed.

1.2.3 Non-contact AFM

A regime of FM-AFM that we will use is non-contact AFM (nc-AFM). In this regime the forces on the cantilever are always attractive, resulting in a minimal interaction and minimal damage caused to the sample. The tip-sample force as a function of tip-sample separation is shown in figure 1.5 and is equal to the gradient of the potential energy with respect to z. The chemical forces can be approximated by the Lennard-Jones potential ($V_{Lennard-Jones}$) [31] given by,

$$V_{Lennard-Jones} = -E_{bond} \left(2\frac{z^6}{z_0^6} - \frac{z^{12}}{z_0^{12}} \right), \tag{1.7}$$

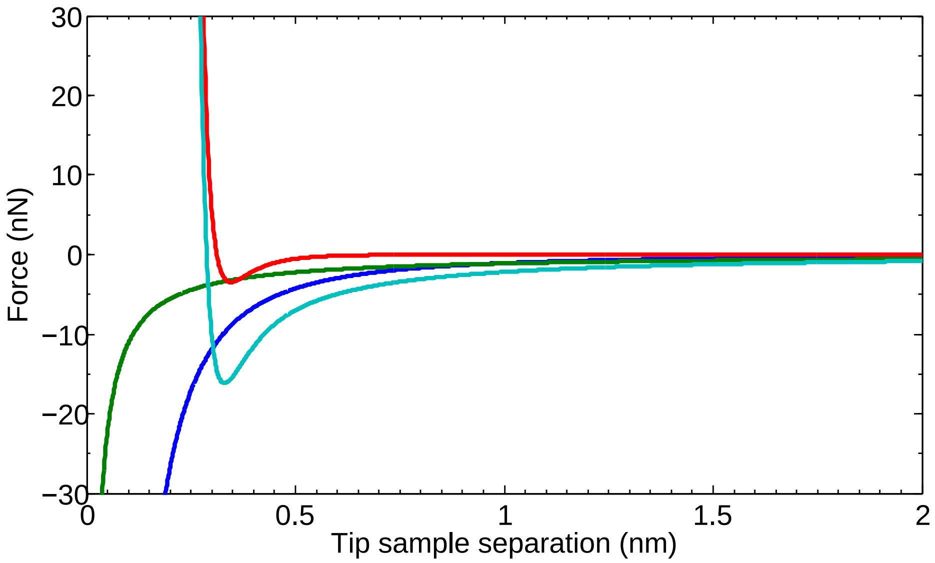

Figure 1.5: Force-distance curve of typical forces in AFM. The red curve represents chemical forces, the green curve represents electrostatic forces, the blue curve represents Van der Waals forces and the cyan curve represents the sum of the 3 curves. In nc-AFM the instrument is operated in the attractive (negative force) regime with the positive slope.

where z is the tip-sample separation, E_{bond} is the bonding energy and z_0 is the equilibrium distance. Van der Waals forces (caused by electric fluctuations of the dipole moment in the atoms in the tip and sample) can be calculated from the Van der Waals potential [31] given by,

$$V_{VDW} = -\frac{A_H R}{6z}, \tag{1.8}$$

where R is the tip radius and A_H is the Hamaker constant which depends on the atomic polarizability and density of the material. V_{VDW} is on the order of 1 eV between most materials in vacuum [31]. The electrostatic forces ($F_{electrostatic}$) are given by [31],

$$F_{electrostatic} = -\frac{\pi \epsilon_0 R V^2}{z}, \tag{1.9}$$

where ϵ_0 is the permittivity of free space, and V is given by,

$$V = V_{t-s} - \frac{\Phi_t - \Phi_s}{e}, \tag{1.10}$$

where the second term on the right hand side of the equation is the contact potential difference [37] and is the result of work function differences between the tip and sample.

1.2.4 Detection of cantilever deflection

The deflection of the cantilever can be detected using an optical beam deflection system, fiber optic interferometry, piezoresistive or piezoelectric systems [31]. The work presented in this thesis was performed on an AFM system with a fiber optic interferometer setup, as described in appendix A.

The cantilever is oscillated by applying an AC voltage at the desired frequency to a shaker piezo that is located under the cantilever chip. In nc-AFM, this frequency is the resonance frequency of the cantilever. To measure the cantilever's resonant frequency change (Δf) upon interaction with a sample, the interferometer signal (deflection signal) goes to a phase-locked loop (PLL) which is described in appendix A. Another control loop maintains a constant oscillation amplitude of the cantilever by exciting the shaker piezo. When energy is dissipated though tip-sample interactions, this loop will drive the shaker piezo stack harder to transfer more energy to the cantilever in order to maintain a constant amplitude of oscillation. The drive signal output can be monitored and is related to the tip-sample dissipation [38,39].

1.3 Magnetic force microscopy

Magnetic force microscopy [34,40,41] (MFM) is a version of dynamic mode AFM in which the cantilever tip is coated with a magnetic material in order to probe magnetic sample properties. The two main operation modes of magnetic force microscopy are constant force gradient imaging (constant frequency shift) [42] and constant height imaging. In constant height mode (the mode used for this work), the tilt of the sample relative to the scan plane is removed. The actual height of the sample (z') is adjusted so that,

$$z' = z + ax + cy, \tag{1.11}$$

where x and y are the lateral position of the sample and constants a and b are adjusted externally to compensate for the unavoidable tilt of the sample plane. This method attempts to make the tip scan plane and the sample plane as parallel as possible. It is not perfect as the tip does not scan in a perfect plane, but rather a slightly spherical surface.

1.3.1 Forces in MFM

The electrostatic force arising from the contact potential difference is minimized using the applied voltage between tip and sample in equation 1.10. The cantilever is then lifted above the surface with topographic feedback turned off. The sample is imaged again. The magnetic force between tip and sample is longer range than Van der Waals and chemical interactions [42]. Therefore, with the contact potential difference minimized, the magnetic interaction between the magnetic tip and sample can be measured at a tip-sample separation large enough that the other forces are negligible.

The magnetic interaction force (F_x, F_y, F_z) between the magnetic sample and the cantilever are given by the volume integral [43],

$$F_i = \mu_0 \iiint\limits_V \vec{M}_{tip} \cdot \frac{\partial \vec{H}_{sample}}{\partial x_i}\, dV = \mu_0 \iiint\limits_V \vec{M}_{sample} \cdot \frac{\partial \vec{H}_{tip}}{\partial x_i}\, dV, \tag{1.12}$$

where μ_0 is the permeability of free space, $\vec{M}$ is the magnetization of the tip or sample and $\vec{H}$ is the magnetic field of the sample or tip.

The frequency shift between magnetic tip and magnetic sample is related to $\partial F/\partial z$ (for small oscillation amplitudes, as shown in equation 1.4). The z direction is the component of interest because the cantilever oscillates in this dimension (in the small angle approximation). The gradient of force in the z direction ($\partial F/\partial z$) is given by,

$$\frac{\partial \vec{F}}{\partial z} = \mu_0 \iiint\limits_V \vec{M}_{tip} \cdot \frac{\partial^2 \vec{H}_{sample}}{\partial z^2}\, dV = \mu_0 \iiint\limits_V \vec{M}_{sample} \cdot \frac{\partial^2 \vec{H}_{tip}}{\partial z^2}\, dV. \tag{1.13}$$

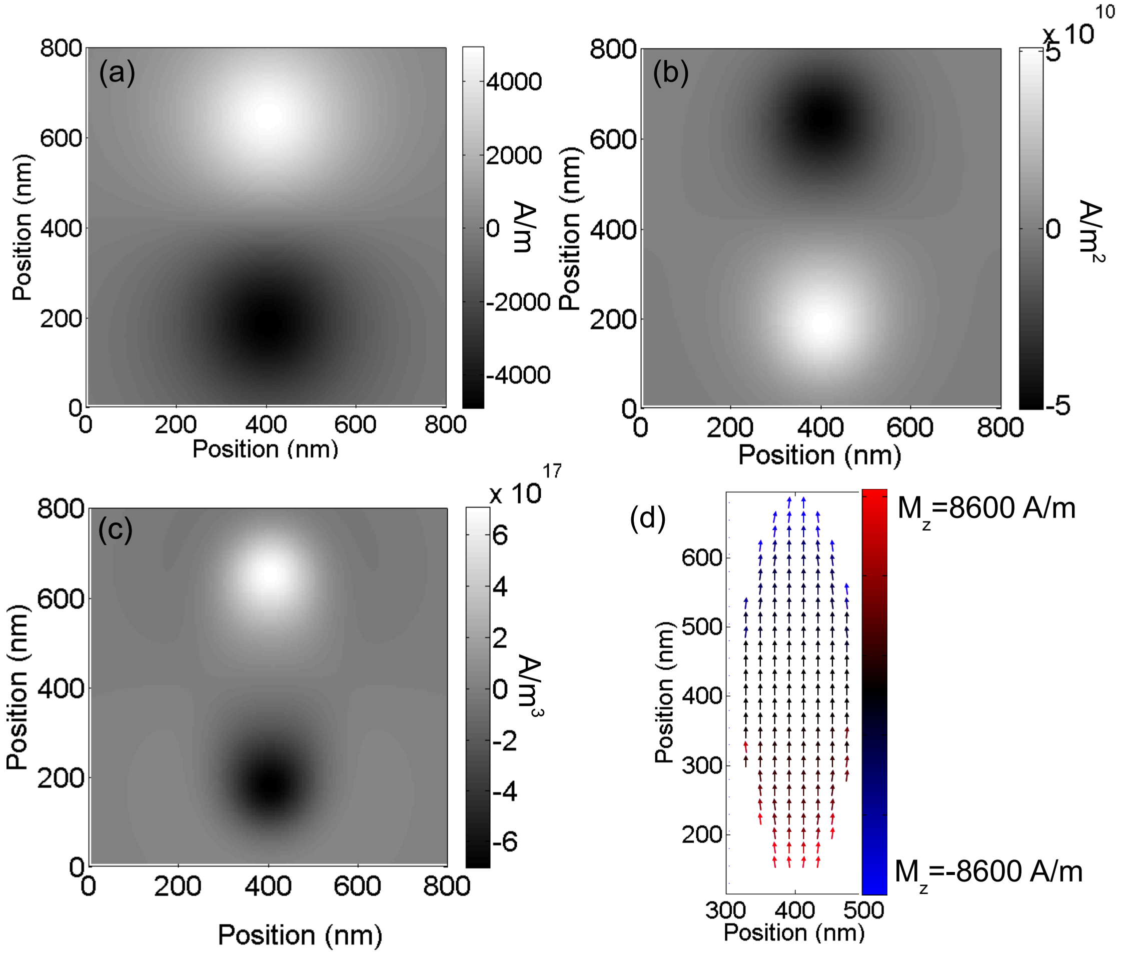

Figure 1.6: OOMMF simulation of permalloy ellipse nanomagnet that is 600 nm × 200 nm × 20 nm. (a) z component of magnetic field 200 nm above the nanomagnet (H_z). (b) z component of the gradient of the magnetic field in the z direction ($\partial H_z/\partial z$). (c) z component of the gradient of (b) ($\partial^2 H_z/\partial z^2$). (d) Vectors indicate magnetization distribution of nanomagnet producing magnetic field, colour indicates component of magnetization in z direction. Note the opposite sign of the magnetic field and derivatives depending on the end of the magnet.

1.3.2 Contrast in MFM images

Figure 1.6 shows a simulation (as described in section 1.4) of the magnetic field 200 nm above a permalloy nanomagnet as well as its gradients in the z direction. From equation 1.13, the frequency shift measured by MFM is related to

$\partial^2 H_z/\partial z^2$, shown in figure 1.6c. Many magnetization configurations can create the same stray magnetic field [44]. Stray field is the result of magnetic charge ($\rho_M = \nabla \cdot \vec{M}$) and there are an infinite arrangements of magnetization ($\vec{M}$) producing the same magnetic charge configuration. A basic knowledge of the sample magnetization is required in order to be able to infer magnetization from frequency shift data [42]. For the nanostructures described in this thesis, a 60 mT magnetic field is applied to samples prior to imaging in order to remove any domain walls in the sample and set the nanostructures to a known initial magnetization configuration. OOMMF simulations (described in section 1.4) then allow for an understanding of the reversal mechanism.

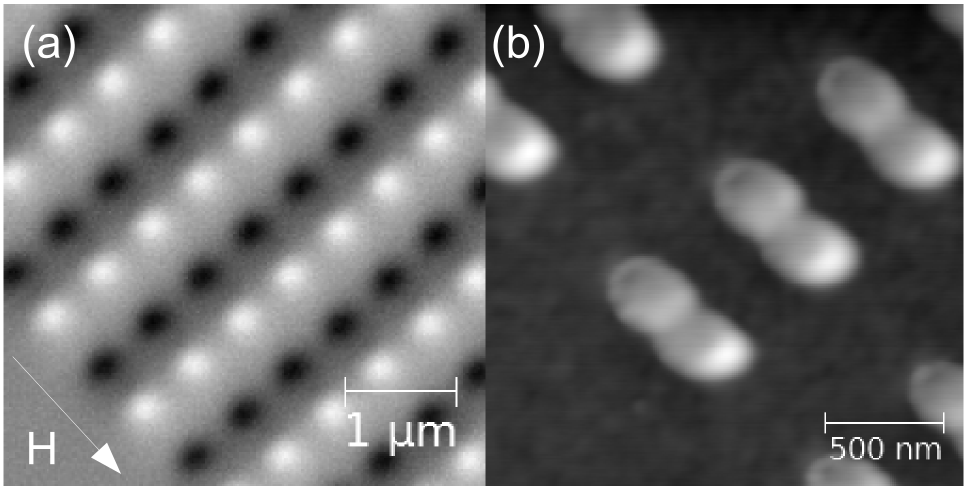

Figure 1.7: (a) MFM image taken of 20 nm thick peanut shaped permalloy nanostructures on silicon substrate (fabricated at University of Sherbrooke using electron beam lithography and electron beam evaporation), in a 60 mT field, at a lift height of 100 nm. The z scale is 3.3 Hz. (b) nc-AFM topography with a frequency shift set point of -2 Hz of some of the structures shown in (a). The z-scale is 50 nm.

Figure 1.7 shows experimental data where the applied magnetic field is aligned along the long axis of the nanomagnet and the tip magnetization is aligned along the z-axis (normal to the plane of the sample). The derivative of the gradient of the stray field with respect to the z-axis has a positive sign or a negative sign, depending on which end of the nanomagnet the cantilever is over (shown in figure 1.6). Because this structure is saturated in a 60 mT applied field, the magnetization direction of the nanomagnet can be determined from this image.

1.3.3 MFM imaging considerations

The magnetic field from the MFM tip can influence the magnetization of the sample [45] and vice versa, so care must be taken to minimize this interaction. By optimizing the magnetic force microscope to improve signal to noise [46], the separation between tip and sample can be increased while still obtaining the magnetization direction of the sample. These optimizations include operating in vacuum, increasing the cantilever oscillation amplitude, and selecting the appropriate cantilever design [46]. By operating in vacuum, the cantilever Q factor can be improved relative to atmospheric pressure, due to a reduction in damping from the transition between viscous and free molecular flow [47]. As mentioned in section 1.2, the signal to noise ratio is improved by increasing the Q factor (equation 1.6). In our experiments we operate at pressures between 1×10^{-5} mbar and 6×10^{-6} mbar, but any pressure below 1×10^{-4} mbar is sufficient to minimize viscous damping effects [47]. The decrease in pressure improves the Q factor in our experiment from on the order of 100 to approximately 10000. Increasing the cantilever oscillation amplitude also increases the signal to noise in MFM [46]. By increasing the amplitude of oscillation, the cantilever interacts with a larger force gradient over the oscillation, which increases the frequency shift of the cantilever as shown in equations 1.4 and 1.5. Typical oscillation amplitudes used in our experiments are between 10 nm and 20 nm.

1.3.4 Measuring switching field using MFM

MFM can be used to spatially resolve the switching field distribution in an array of nanomagnets by taking MFM images of a sample in the presence of different externally applied magnetic fields. The magnetization direction of each nanomagnet can be determined at each applied magnetic field, making it effectively an imaging magnetometer. Because MFM is used only to determine the magnetization direction of a nanomagnet in this work, it allows the lift height to be much higher than typical MFM imaging. The higher lift height reduces the influence of the magnetized MFM cantilever on the nanostructure.

1.3.5 External magnetic field

The external magnetic field applied to the sample using electromagnets [46] or permanent magnets, as described in appendix A. The benefit of using permanent magnets over electromagnets is that the heat generated by the current needed to produce the magnetic field can be avoided. Heat is not dissipated by convection under vacuum, and can result in sample heating as well as thermal microscope drift [48, 49]. There are also drawbacks to using a permanent magnet. As described in appendix A, motors are used to rotate permanent magnets to vary the amount of magnetic flux that passes though the soft iron poles. The actuation of these motors causes vibrations in the AFM setup, which, if the tip and sample are in close proximity, could cause them to collide. To prevent damage from an un-controlled collision, the sample is retracted from the tip before the motors are used to change the magnetic field. After the field is set, the sample is approached to the tip. The change in tip-sample separation is typically around 4 μm (half of the range of the piezo tube).

1.3.6 Piezo creep

After the applied magnetic field is changed and the sample is re-approached to the tip, the piezo will start to creep so that the sample extends towards the cantilever. Piezo creep is the slow change in piezo extension that occurs after the bias across a piezoelectric material is changed in order to change its displacement. The piezo creep displacement depends on the magnitude of the desired change of displacement as given by [50],

$$z(t) = z_0 \left(1 + \gamma log_{10}\left(\frac{t}{t_0}\right)\right), \tag{1.14}$$

where z_0 is the desired displacement, $z(t)$ is the actual displacement as a function of time, γ is the rate of creep, t_0 is is the time at which the fast change in position has finished. The piezo creep over time in our system is shown in figure 1.8, following a 3.5 μm change in piezo height. For the experiment shown in figure 1.8, γ = -0.0633 $\pm$ 0.0001.

The data from figure 1.8 indicates that a lower voltage applied to the piezo tube is required to keep the sample at the same position. If topography feedback is turned off (a constant voltage is applied to the piezo tube) and the MFM tip is lifted to perform an MFM scan, immediately after the sample is re-approached, the sample will slowly creep towards the tip during the scan. This results in a tip-sample distance that decreases during a scan. To avoid a change in the tip-sample separation during a MFM scan, topography feedback is kept on with the sample approached to the cantilever for 10 to 15 min before the MFM scan is started. To

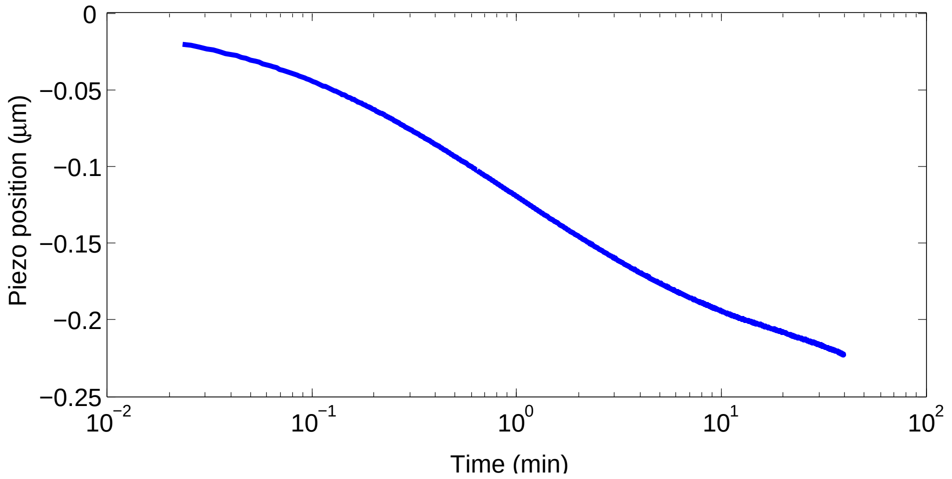

Figure 1.8: Cantilever z position with feedback on as a function of time after a 3.5 μm change in piezo extension at t=0 min.

avoid influencing the magnetization of the sample with the magnetic tip during the 10 to 15 min wait time, the cantilever is approached at a lateral distance of more than 5 μm from the nanostructures.

1.4 Simulation of magnetic nanostructures

Nanomagnets have been shown to reverse magnetization direction by nucleation and propagation of a domain in the nanomagnet, rather than coherent magnetization rotation, for nanomagnets of less than 100 atoms [51]. Publicly available software called Object Oriented MicroMagnetic Framework (OOMMF) from the National Institute of Standards and Technology [52] will be used for the simulation of the complex reversal mechanism of nanomagnets. OOMMF uses a finite difference method which stores the magnetization, ($\vec{M}$), and the effective field, ($\vec{H}_{eff}$), at each voxel of the nanomagnet. OOMMF then evolves the magnetization in a series of applied magnetic fields, to determine the reversal mechanism and the coercive field at zero temperature [53].

To simulate the magnetic reversal of nanomagnets, a mean field theory that assumes magnetization, exchange field and demagnetizing field change slowly on the atomic length scale is necessary [53]. These assumption are necessary because at the length scales of interest in this work (∼600 nm × 200 nm × 20 nm), *ab initio* simulation of the magnetization of each atom is not currently feasible [53]. The exchange length (l_{ex}) is the length over which the exchange energy dominates other interactions, such as anisotropy, demagnetization, Zeeman and magnetoelastic energies (described below). Over the length scale of the exchange length the magnetization is constant. This means that provided a good choice of voxel (volumetric pixel) size is made by the user, the assumption of slowly varying fields is a good one. The exchange length is given by,

$$l_{ex} = \sqrt{\frac{2A}{\mu_0 M_s^2}}, \tag{1.15}$$

where A is the exchange stiffness (13×10^{-12} J/m in permalloy [19]), μ_0 is the permeability of free space, and M_s is the saturation magnetization (860×10^3 A/m in permalloy [19]). The typical voxel size for our simulations is 5 nm × 5 nm × 5 nm, which is approximately equal to the exchange length of permalloy (calculated using equation 1.15 and the exchange stiffness and saturation magnetization given above).

The rate of change of the magnetization direction ($\frac{d\vec{M}}{dt}$) of a magnetic volume in a magnetic field (which is also sometimes referred to as the stray field or demagnetizing field), $\vec{H}_{eff}$, is given by,

$$\frac{d\vec{M}}{dt} = -\gamma[\vec{M} \times \vec{H}_{eff}], \tag{1.16}$$

where $|\gamma|$ is the gyromagnetic ratio. Gilbert damping [53, 54] is added as an effective field proportional to $\frac{d\vec{M}}{dt}$ which is given by,

$$\vec{H}_{eff_{damping}} = \vec{H}_{eff} - \alpha\frac{1}{\gamma_0 M_S}\frac{d\vec{M}}{dt}, \tag{1.17}$$

Where α is the damping constant (α was set to 0.5 [55]). Gilbert damping describes damping that is not attributed to eddy currents such as coupling of the magnetization to spin waves and lattice vibrations [54]. By substituting the new effective field with damping into equation 1.16, one arrives at the Landau Lifshitz Gilbert (LLG) equation given by [54],

$$\frac{d\vec{M}}{dt} = -|\gamma|\vec{M} \times \vec{H}_{eff} + \frac{\alpha}{M_s}(\vec{M} \times \frac{d\vec{M}}{dt}), \tag{1.18}$$

where $\vec{H}_{eff}$ is the effective field given by [56],

$$\vec{H}_{eff} = -\frac{1}{\mu_0}\frac{\partial E_{density}}{\partial \vec{M}}. \tag{1.19}$$

$E_{density}$ is the sum of the magnetic energy terms given by [53],

$$E_{density} = E_{exchange} + E_{anisotropy} + E_{demag} + E_{Zeeman} + E_{Magnetoelastic}. \tag{1.20}$$

The energy terms in equation 1.20 are defined below. The magneto-elastic energy, due to the interaction between the magnetization direction and stresses in the material [57], will be neglected because it is negligible in permalloy [58]. The exchange energy ($E_{exchange}$), which is the result of the quantum mechanical exchange interaction, is given by [53],

$$E_{exchange} = \int_V \frac{A}{M_s^2}(|\nabla\vec{M}|)^2 d^3r, \tag{1.21}$$

where A is the exchange constant in J/m ($A = 13 \times 10^{-12}$ J/m for permalloy [19]). The exchange energy is responsible for the exchange length, given by equation 1.15. The magnetocrystalline anisotropy is the result of differences in spin orbit coupling depending on the crystal axis [57, 59]. Because of the difference in spin orbit coupling there is a difference in energy depending on the magnetization direction, which can result in what is called an easy or a hard axis [57]. A material with an easy axis has an axis where the magnetization is energetically favorable to align, and a material with a hard axis has an axis where it is energetically favorable to align the magnetization with the plane normal to the hard axis. The magnetocrystalline anisotropy energy, $E_{anisotropy}$, is given by,

$$E_{anisotropy} = \sum_V \left[\frac{K_1}{M_s^4}(M_x^2M_y^2 + M_y^2M_z^2 + M_z^2M_x^2) + \frac{K_2}{M_s^6}(M_x^2M_y^2M_z^2)\right] V_{cell}, \tag{1.22}$$

where K_1 and K_2 are the first and second material anisotropy coefficients respectively [53] (which are both close to zero Jm^{-3} for permalloy and randomly oriented because permalloy is polycrystalline [19]). The Zeeman energy is the energy that a magnetic moment has in an external applied magnetic field ($\vec{H}_{ext}$). Interaction between neighbouring nanomagnets that cause an increase in the SFD are a result of this energy term. The Zeeman energy (E_{Zeeman}) is given by,

$$E_{Zeeman} = -\mu_0 \vec{M} \cdot \vec{H}_{ext}. \tag{1.23}$$

The demagnetization energy, E_{demag}, is the result of long range dipolar interactions [59] and can be thought of as the self energy of the magnetization configuration. Differences in shape anisotropy and edge roughness cause changes in the demagnetizing energy [59]. Demagnetization energy is given by,

$$E_{demagnetization} = -\frac{\mu_0}{2} \sum_i \vec{M}_i \cdot \vec{H}_i V_{cell}, \tag{1.24}$$

where H_i is the demagnetizing field, which is calculated assuming that the magnetization is constant in each voxel [60]. The calculation of the demagnetization field exploits the fact that there are no free currents in a magnet such that,

$$\nabla \cdot \vec{B} = 0,\ and\ \nabla \times \vec{H} = 0. \tag{1.25}$$

We can then use a magnetic scalar potential, Φ_M, such that [61],

$$\vec{H} = -\nabla \Phi_M, \tag{1.26}$$

where Φ_M at a position $\vec{x}$, is given by,

$$\Phi_M(\vec{x}) = -\frac{1}{4\pi}\left[\int_V \frac{\nabla' \cdot \vec{M}(\vec{x}')}{\mid \vec{x} - \vec{x}' \mid} d^3x' + \int_S \frac{\vec{n}' \cdot \vec{M}(\vec{x}')}{\mid \vec{x} - \vec{x}' \mid} d^2x'\right]. \tag{1.27}$$

The primes are the integration volume, resulting in a demagnetization field equal to,

$$\vec{H}_{demag} = -\frac{1}{4\pi}\left[\int_V \frac{(\vec{x}-\vec{x}')\nabla'\cdot\vec{M}(\vec{x}')}{\mid \vec{x}-\vec{x}' \mid^3} d^3x' + \int_S \frac{(\vec{x}-\vec{x}')\vec{n}'\cdot\vec{M}(\vec{x}')}{\mid \vec{x}-\vec{x}' \mid^3} d^2x'\right], \qquad (1.28)$$

where the first term is the result of magnetic volume charges, and the second term is the result of magnetic surface charges. Because equation 1.28 is of the form of a convolution integral ($\int f(x')g(x-x')dx'$), a fast Fourier transform can be used to compute it, drastically reducing computation time [53, 62, 63].

OOMMF accepts a black and white image as an input with user defined length, width and thickness. This allows for the simulation of a wide variety of nanomagnet shapes. The user then defines the saturation magnetization of the black and white regions (the location of the magnetic material). The image is divided into voxels, which are chosen to be smaller than the exchange length. The user specifies a list of applied magnetic fields at which the simulation will be carried out and then defines an initial magnetization state of the structure to be simulated.

Typically, the magnetization is initially assigned randomly and then is allowed to relax in a large applied field. The simulation is then carried out as follows: first the field is applied and the structure magnetization state evolves according to equation 1.18. Once the voxel with the highest rate of change of magnetization direction with respect to time, given by equation 1.18, drops below a user defined threshold (0.01°/ns for the simulations presented here), OOMMF saves the sample magnetization configuration as well as any other user defined fields and then moves on to the next user-defined applied magnetic field. In magnetic simulations it is important that the structure is not symmetric about the axis along which the field is applied. This is because of the lack of imperfections in the simulation; there is nothing to break the horizontal symmetry, which results in an artificially high switching field. This issue is circumvented by slightly rotating the simulated structure relative to the applied field [64].

OOMMF can be used to simulate the magnetization configuration of a nanomagnet in an externally applied magnetic field, simulate the stray field from a nanomagnet and most importantly for this work, simulate the switching field of a nanomagnet so that factors influencing the switching field can be better understood.

Stoner-Wohlfarth analysis estimates how the coercivity changes with shape for an ellipse with thickness (t) less than the exchange length (equation 1.15) assuming coherent rotation of the magnetization. Stoner-Wohlfarth estimates the coercivity (H_c in SI units) [65,66],

$$H_c = \frac{2M_s t}{\pi W} \cdot S, \tag{1.29}$$

where W is the width and S is the finite-length shape anisotropy factor given by,

$$S = \frac{\rho - 1/\rho}{\sqrt{1+\rho^2}}, \tag{1.30}$$

where ρ is the aspect ratio of the ellipse ($\rho = \frac{length}{width}$). The exchange length of permalloy is approximately 5 nm. This is less than the simulated ellipse thickness shown in figure 1.6, but three dimensional switching mechanisms are avoided as long as the thickness is less than 25 nm in permalloy [65,67]. Assuming three dimensional switching mechanisms are avoided, Stoner-Wohlfarth analysis should allow for an approximation of the switching field dependence on shape. For a permalloy nanostructure that is 540 nm × 180 nm × 20 nm (the shape that will be studied in this thesis), Stoner-Wohlfarth analysis predicts a coercivity of 64 mT.

1.5 Magneto-optical Kerr effect measurement

The magneto-optical Kerr effect (MOKE) is used for the study of thin magnetic films [68]. When linearly polarized light is reflected off of a magnetic sample, rotation or ellipticity is induced in the light depending on the magnetization direction. This rotation or ellipticity change can be used to measure the coercivity of thin films and micron size structures [69]. There are three different MOKE modes, illustrated in figure 1.9. Each MOKE type is sensitive to a different magnetization direction.

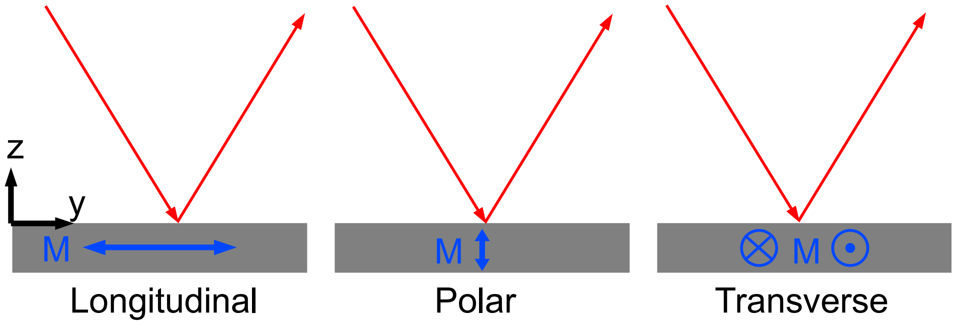

Figure 1.9: Three different MOKE configurations indicating the magnetization direction they are sensitive to.

MOKE is understood by looking at the antisymmetric portion of the dielectric tensor ($\bar{\bar{\epsilon}}$) given by [70–73],

$$\bar{\bar{\epsilon}} = \epsilon_r \begin{bmatrix} 1 & iQm_z & -iQm_y \\ -iQm_z & 1 & iQm_x \\ iQm_y & -iQm_x & 1 \end{bmatrix}, \tag{1.31}$$

where ϵ_r is the dielectric constant, Q is the magneto-optic constant (which is material dependent) and $\vec{m} = (m_x, m_y, m_z)$ is the magnetization unit vector [73]. Because permalloy has magnetization in-plane, longitudinal MOKE (which is sensitive to the magnetization in the m_y direction) is of particular interest.

Linearly polarized light can be decomposed into right hand circularly polarized (RHCP) light and left handed circularly polarized (LHCP) light. It is therefore helpful to look at the dielectric constants of RHCP and LHCP light given by [72],

$$\epsilon_{RHCP} = \epsilon_r(1 - Qm \cdot \hat{k}), \tag{1.32}$$

$$\epsilon_{LHCP} = \epsilon_r(1 + Qm \cdot \hat{k}), \tag{1.33}$$

where $\hat{k}$ is the unit vector in the direction of light propagation. RHCP and LHCP light can travel though the sample at different speeds depending on the sample magnetization and the magneto-optic constant, resulting in a rotation of the polarization.

The apparatus for performing longitudinal MOKE measurements is shown in figure 1.10. Longitudinal MOKE is sensitive to the magnetization in the direction that intersects the optic plane with the plane of the sample surface (see figure 1.9). By reflecting linearly polarized light off of the magnetic sample, the differ-

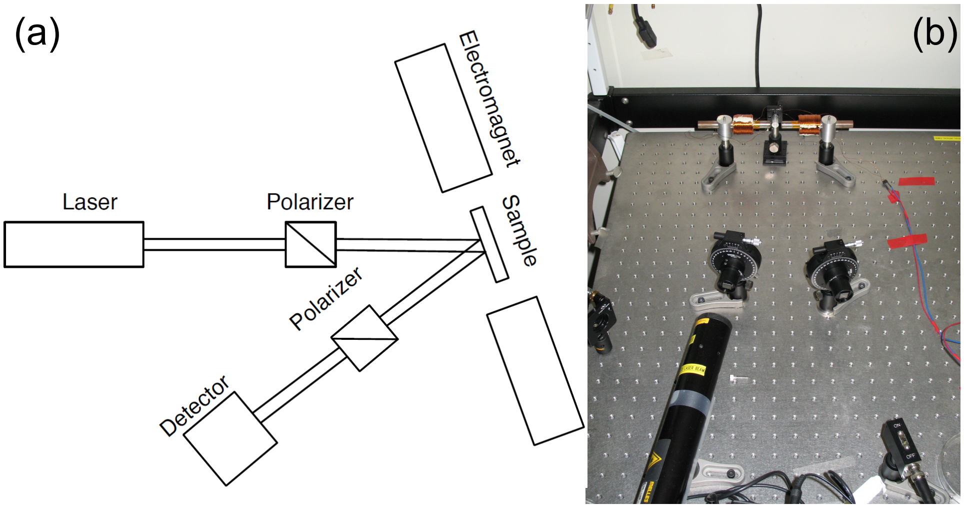

Figure 1.10: (a)MOKE schematic for longitudinal MOKE. (b) MOKE apparatus using a 5 mW He Ne laser from Melles Griot (05-LHR-151).

ences in velocity of RHCP and LHCP cause a rotation in the polarization of the reflected light. This rotation can be detected by placing another polarizer at an angle of 45° with respect to the initial polarizer. The magnetization of the sample is then reversed by sweeping an external applied magnetic field. When the magnetization reverses, the sign of the polarization rotation also reverses, and the hysteresis loop of the magnetic film can be measured.

For example, the magnetization reversal of a 20 nm permalloy film deposited by magnetron sputtering is shown in figure 1.11. The coercivity of the film shown in figure 1.11 is approximately 160 A/m. The coercivity of permalloy films can be as low as 4 A/m [58] depending on the thickness, grain size and the substrate used [74].

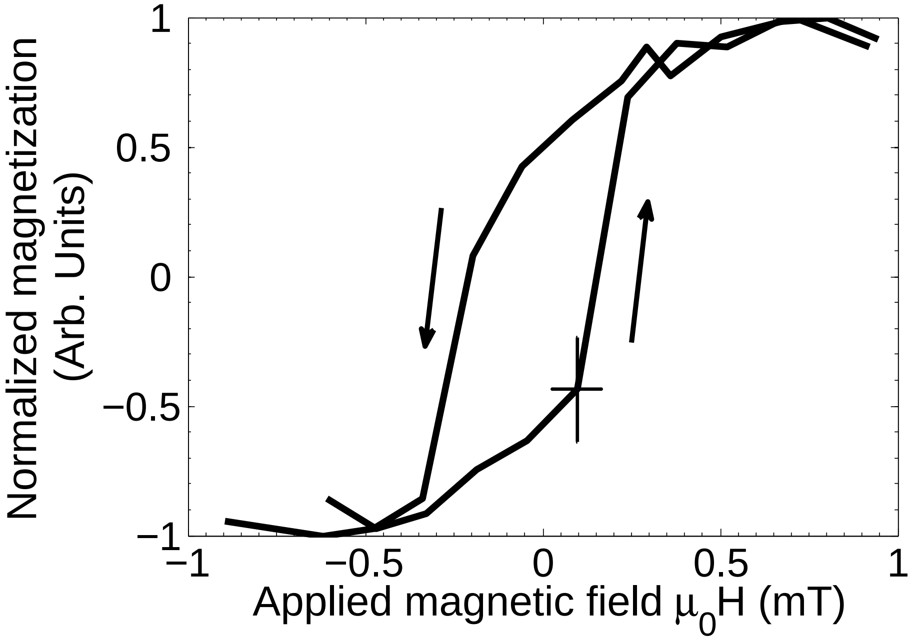

Figure 1.11: MOKE data of a 20 nm permalloy film on a silicon oxide substrate deposited by magnetron sputtering. Data points represent an average of 10 reversal cycles. The error in normalized magnetization is the standard deviation of these data points. The error for the data point with the largest error is shown.

1.6 Transmission electron microscopy

Imaging small structures is an important capability in understanding the function of nanostructures. Optical measurements are limited by the far field resolution limit (d), which is given by,

$$d = \frac{\lambda}{2n\sin\theta}, \tag{1.34}$$

where λ is the wavelength of the light or particle used to image, $nsin\theta$ is known as the numerical aperture, where n is the refractive index of the medium between the lens and sample and θ is half the maximum acceptance angle of light from the sample. To improve the resolution of an optical microscope, light with a smaller wavelength can be used or the numerical aperture of the lens can be increased by increasing the refractive index of the medium between the sample and the lens.

If decreasing the wavelength of light is insufficient, another option is to exploit the fact that matter has a wavelength that depends on its momentum, called the de Broglie wavelength (λ),

$$\lambda = \frac{h}{p}, \tag{1.35}$$

where h is Planks constant and p is the particle momentum. Electrons with higher velocity have higher momentum and therefore lower wavelength. An electron that is accelerated though a 200 kV electric field has a wavelength of approximately 3 pm. This results in a drastically smaller resolution limit for imaging with electrons when compared to visible light, which ranges from 380 nm to 740 nm in wavelength.

Transmission electron microscopy (TEM) is a high resolution electron imaging technique that makes use of this smaller diffraction limit. It is therefore ideal for imaging magnetic nanostructures that could not be resolved optically. Electrons with energy in the keV range typically have sample penetration distances of several μm [75]. An image is formed when electrons pass through a thin sample and are collected using a charge-coupled device (CCD) camera.

In order for electrons to pass though a sample, it is important that the sample is thin enough to avoid excessive absorption and scattering. The main source of contrast in TEM is the result of electrons elastically scattering. The differential scattering cross section for electron energies under 300 keV and atomic number under

30 is given by the screened, relativistic differential Rutherford cross section [76].

$$\sigma_R(\theta) = \frac{Z^2 \lambda_R^4 d\Omega}{64\pi^4 a_0^2 \Big[\sin^2\left(\frac{\theta}{2}\right) + \frac{\Theta_0^2}{4} \Big]^2}, \tag{1.36}$$

where Z is atomic number, λ_R is the electron wavelength that has been relativistically corrected, θ is the scattering angle, Ω is the solid angle made by θ and a_0 is the Bohr radius of the atom that is scattering the electron. Θ_0 is the screening parameter and is equal to [76],

$$\Theta_0 = \frac{0.117 Z^{1/3}}{E_0^{1/2}}, \tag{1.37}$$

where E_0 is the energy of the electrons in keV. By integrating over an area from θ to π, one arrives at the scattering cross section for scattering into an angle greater than θ, which is given by [76],

$$\sigma_{nucleus} = 1.62 \times 10^{-24} \left(\frac{Z}{E_0} \right)^2 \cot^2 \frac{\theta}{2}. \tag{1.38}$$

It is important to note the dependence of scattering on atomic number. This will influence the choice of substrates that samples may be imaged on as well as restrict the use of protective metal coatings. SiN membranes are a common TEM substrate due to the low atomic numbers of silicon and nitrogen.

Electrons that are used to image in TEM are ejected from a cathode (electron gun) and accelerated through an electric field to an anode. These electrons are then focused onto the sample using a series of lenses. The electrons that aren't scattered or absorbed passing though the sample are then focused onto a CCD camera [75].

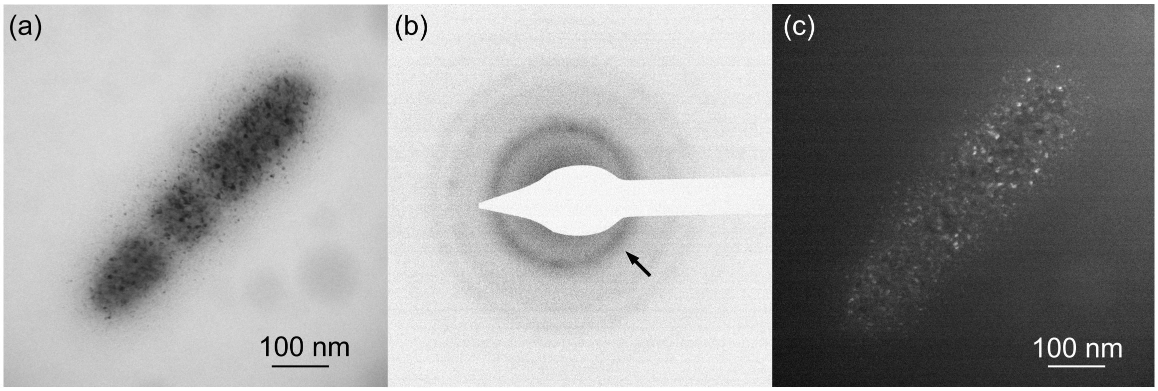

Figure 1.12: (a) Bright field TEM image of permalloy nanostructure fabricated by magnetron sputtering though a FIB milled nanostencil. (b) diffraction pattern from a region in (a) with contrast inverted. Scale for image is 13.2 mmÅ. The central spot of un-diffracted electrons has been blocked so the image isn't saturated (white region). (c) Dark field TEM image of diffraction ring (111) indicated by an arrow in (b).

1.6.1 Bright field TEM

To project a real space image of electrons that pass though a sample (called bright field (BF) TEM image) onto the CCD camera, the intermediate lens is adjusted so that the image plane of the objective lens is the intermediate lens' object plane [76]. The resulting real space image is an image of unscattered electrons, as shown in figure 1.12a.

1.6.2 Diffraction

To project a diffraction pattern onto the CCD camera, the intermediate lens is adjusted so that the back focal plane of the objective lens is the intermediate lens' object plane [76]. The diffraction pattern gives structural information about the sample, as shown in figure 1.12b.

1.6.3 Dark field TEM

In dark field (DF) TEM imaging, a diffraction spot or region in the diffraction pattern is selected (using a diaphragm) rather than using the direct beam to produce a spatial image of the sample. The intermediate lens is adjusted again so that the image plane of the objective lens is the intermediate lens' object plane (called imaging mode), which projects a real space image onto the CCD camera [76]. This real space image is made using electrons that are diffracted from the selected diffraction spot or region, as shown in figure 1.12c.

1.6.4 Energy dispersive x-ray spectroscopy

Energy dispersive x-ray (EDX) spectroscopy is used for chemical identification as well as measuring relative chemical composition for atomic numbers over 11 [75]. In EDX, electrons from the TEM are focused onto a small spot ($\sim$20 nm) on the sample. These electrons have a small probability of interacting with the sample inelastically, exciting electrons in the sample to higher energy levels [75]. When the atom relaxes to its ground state, it can emit a photon. The energy of this photon is the difference in energy between the excited and relaxed state, both of which depend on the atomic number of the atom and on the specific orbitals involved. It can therefore be used to determine the chemical composition of a sample.

A spectrum is obtained by counting the number of incoming photons at a given energy, as shown in figure 1.13. Peaks in the spectrum are then compared to the known energy transitions [77]. Typical semiconductor based detectors have resolution of 135 ± 10 eV [76], which can cause peaks to overlap. Peak overlap is a problem when the elements of interest have peaks in close proximity to each other.

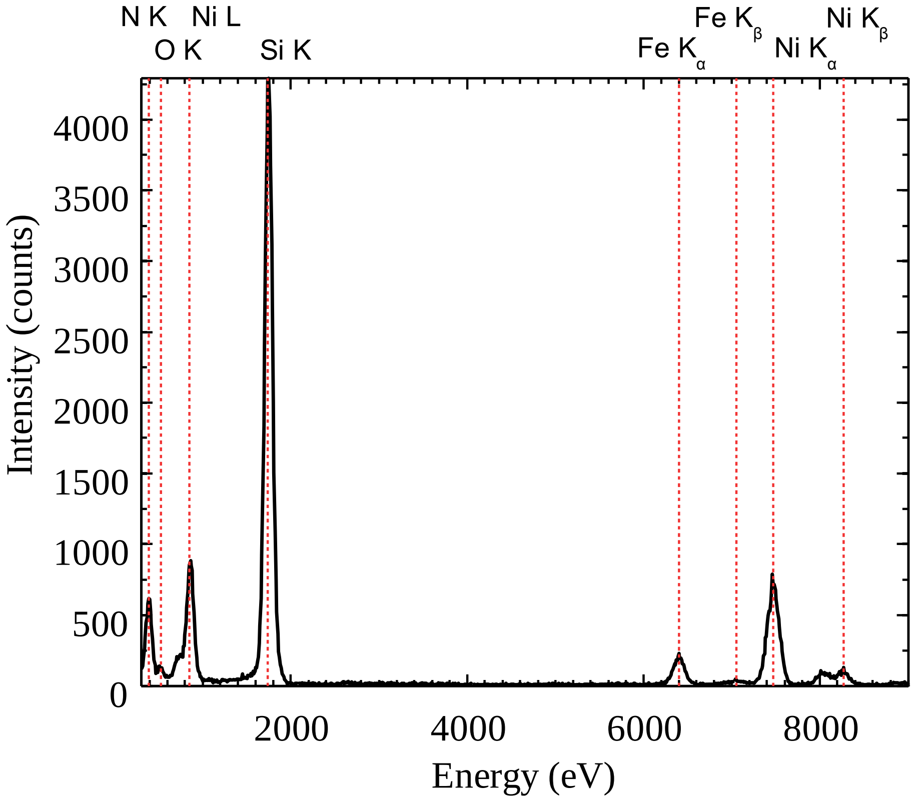

Figure 1.13: EDX of electron beam evaporated permalloy on a SiN membrane. Red dotted lines represent peaks from labeled transitions. Resulting composition is $Ni_{88\pm2}Fe_{12\pm2}$.

Nickel and iron have EDX peaks that are sufficiently spaced that deconvolution is not necessary.

Comparing the relative number of photon counts per energy does not allow direct measurement of relative chemical composition because of several factors, including the ionization cross sections of the elements in the sample, fluorescence of the sample and the probability that emitted photons are re-absorbed by the sample [78]. These factors must be accounted for before the relative concentration can be determined. This can be accomplished using a ZAF (atomic number (Z), absorption (A), fluorescence (F)) standard-less quantification which estimates the influence of these factors to estimate the relative composition [75]. After the ZAF corrections are made, the relative composition must be compared to the minimum mass fraction, $C_B(MMF)$, that can be detected given by [76],

$$C_B(MMF) = \frac{3(2I_B^b)^{1/2}C_B}{I_B - I_B^b}. \tag{1.39}$$

I_B^b is the background intensity for element B, C_B is the measured concentration of B and I_B is the integrated intensity of peak B, including the background.

1.6.5 Electron energy loss spectroscopy

Instead of measuring photons emitted from excited atoms, electron energy loss spectroscopy (EELS) measures the energy of the TEM electron beam after it passes though the sample [75]. EELS is advantageous over EDX in terms of chemical composition mapping for lower atomic numbers [79]. Some electrons that pass though the sample have a slightly lower energy due to inelastic collisions with the sample. By passing these transmitted electrons though a uniform magnetic field (which acts as a prism due to the Lorentz force) the electrons can be separated by energy. A CCD array then records the dispersed electrons [75]. There is a sharp increase in electron intensity at the energy required to create an excitation. These excitation energies have been cataloged for each atom and therefore chemical identification and composition measurements can be made. To calculate relative concentration ratios, a correction for the ionization cross section is made.

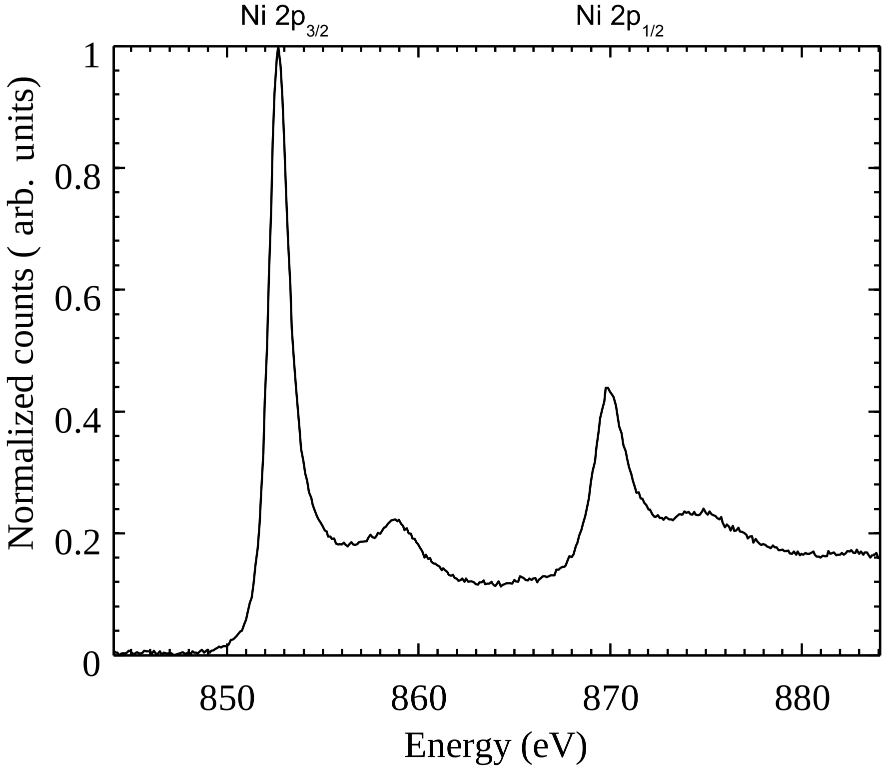

Figure 1.14: XPS of a thin film (20 nm thick) of electron beam evaporated permalloy on a silicon oxide substrate.

1.7 X-ray photoelectron spectroscopy

X-ray photoelectrons spectroscopy (XPS) is a surface science technique that allows chemical composition and information about atomic bonds to be measured. By directing monochromatic x-ray photons (from the Al K_α transition, Mg K_α transition or using a synchrotron radiation source [80]) at a sample, core electrons are ejected due to the photoelectric effect. The energy of these electrons can be measured and related to the electron's binding energy [80],

$$E_B = h\nu - E_K - \Phi, \tag{1.40}$$

where E_B is the binding energy of the electron before it is ejected, $h\nu$ is the energy of the incident x-ray photon, E_K is the measured kinetic energy of the electron after it is ejected and Φ is the work function of the material. By comparing the binding energy with an XPS database [81], the chemical composition of the sample can be determined as well as the chemical environment of the atoms. XPS is a surface sensitive technique that generally probes a depth of less than 10 nm [80], but it can be combined with sputtering to measure depth profiles. Figure 1.14 is a typical XPS scan of an electron beam evaporated permalloy sample on a silicon oxide substrate. The absence of peaks between 854 eV and 857 eV (the location of nickel oxide peaks) confirms that the film does not have nickel oxide within experimental error.

1.8 Characterization facilities

All MFM, AFM and MOKE measurements presented in this thesis were performed at McGill University by the author of this thesis. TEM imaging and EDX measurements were made by Dr. David Liu and the author of this thesis at the facility for Electron Microscopy Research at McGill University using a Philips CM200 TEM. EELS measurements were made at the Canadian Centre for Electron Microscopy at McMaster University. XPS measurements were made at the McGill Institute for Advanced Materials by Robert Gagnon and the author of this thesis.

2

Preparing Magnetic Nanostructures

2.1 Focused ion beam

Focused ion beam (FIB) is a useful tool in which a beam of ions are focused onto a surface to sputter (mill) away that region of the sample. In a high vacuum chamber, a liquid metal ion source is formed by connecting a tungsten tip to a resevoir of gallium. The gallium is heated to above its melting temperature to wet the surface of the tungsten tip. An electric field of approximately 10^8 V/cm [82] is applied to the tungsten tip so that the liquid gallium sharpens the source apex to a diameter of 2 to 5 nm [82]. An extraction voltage then field evaporates gallium ions from the tip. A constant ion current is maintained using a suppressor voltage. The extracted gallium ions pass though a condenser lens and an aperture with a diameter selected based on the desired ion current. The gallium ions then pass though a series of lenses that deflect the beam and adjust the astigmatism and alignment. Finally, another lens focuses the beam on to the sample.

When the gallium ions bombard the sample surface they can sputter both neutral and ionized atoms and molecules from the sample, as well as create secondary electrons [83]. Gallium ions may become implanted in the sample [84–86]. Besides sputtering, the FIB can be used to image the surface by collecting the secondary electrons produced upon beam exposure, similar to a scanning electron microscope (SEM). The drawback to imaging using a FIB is that it is usually destructive to the sample [82]. A better alternative is to use a dual column FIB, which contain SEM and FIB columns that are commonly oriented at 52° with respect to each other. This requires that the sample stage be able to both translate in 3 dimensions as well as rotate in 2 axes so that milling and imaging can both be done at normal incidence. When using the dual column FIB/SEM, the SEM is used to locate the desired milling location. The stage is then rotated to face the FIB column for milling. The milling rate of a FIB depends on the dwell time, beam current, acceleration voltage, pixel spacing and the size of the aperture used [83]. All focused ion beam work in this thesis was done at École Polytechnique de Montréal using a dual column FEI strata DB-235 by the author of this thesis.

The FIB is a versatile tool that can be used in lithography [87], material removal [83, 88], ion implantation [89] and deposition of material [90] for applications such as preparation of TEM cross sections [91] and repairing of masks [92,93]. FIB is also a convenient tool for making custom alterations on commercially available products [88]. For example, in figure 2.1, gold was milled away on the bottom cantilever to make a Fresnel pattern on commercially available gold-coated 500 μm long arrow TL2 cantilevers (beam current 30 pA, acceleration voltage 30 kV). The top cantilever was left untouched so that the effects of the pattern could be determined. Both cantilevers baseline power spectral densities were measured before and after FIB milling. The gold Fresnel pattern succeed in reducing classical and shot noise by two times in an optical beam deflection system. The gold layer causes stress induced bending due to differences in the thermal expansion coefficient between gold and silicon. Temperature changes of the cantilever are generally caused by fluctuating laser power, used to detect the cantilever position [88].

Because 75% of the gold layer was removed, the amplitude of the stress induced bending was reduced. The Fresnel lens also maximizes the peak laser intensity located at the centre of the photodiode by removing light that destructively interferes at the photodiode [88].

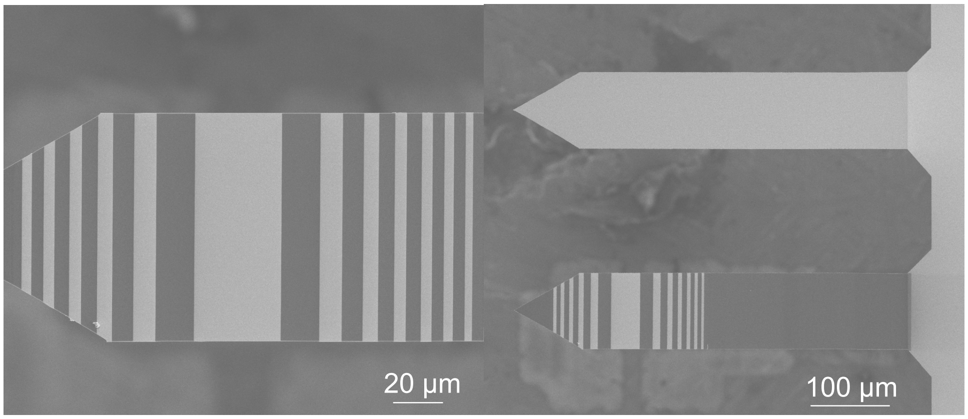

Figure 2.1: SEM image of Fresnel cantilever. Gold coating is milled away on the bottom cantilever using focused ion beam milling. The top cantilever is left unaltered. The brighter colour is gold and the darker region is the milled area exposing the silicon cantilever.

2.2 Nanostructure fabrication

The use of nanostencil lithography for depositing patterned films has advantages over standard lithography techniques in that possible sources of contamination such as etching, solvents, and resists can be avoided [94,95]. Other artifacts, such as side rims in electron beam lithography and redeposition of etched material during reactive ion etching, can be avoided by depositing though a nanostencil [96]. There are several techniques used to fabricate nanostencils, including electron beam lithography [97, 98], interferometric lithography [98, 99], extreme ultraviolet and x-ray lithography [98] as well as FIB milling [100].

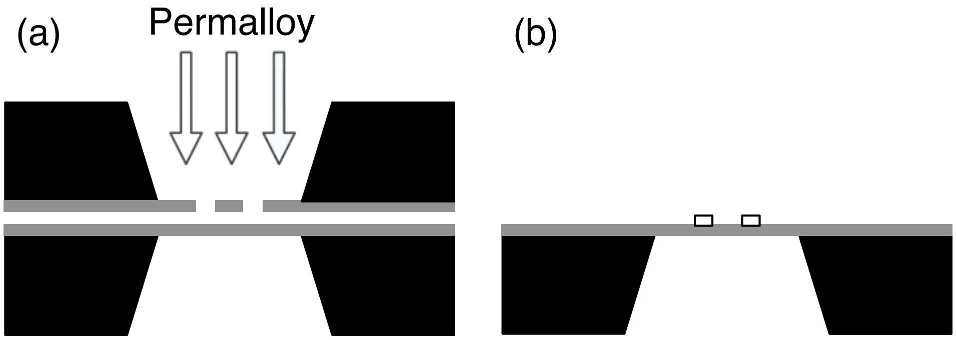

Figure 2.2: Schematic of the sample preparation (not to scale). Black, grey and white represent silicon, silicon nitride, and permalloy respectively. (a) A FIB milled nanostencil is placed on top of a SiN membrane. Permalloy ($Ni_{81}Fe_{19}$) is evaporated though the holes. (b) The FIB milled nanostencil is removed, leaving nanostructures where the nanostencil holes were located.

FIB was used to fabricate the stencils in this work (unless otherwise specified) due to its versatility, ease of use, and availability. The alternate method of spin coating photoresist onto free standing SiN membranes can cause problematic deformation of the free standing membrane and non-uniformities in the resist coating due to edge effects of the 3 mm SiN sample. There are two different modes for stencil lithography: static [101–104] and dynamic [105–108]. We will use static mode as it does not require control of the stencil position during evaporation. Static mode stencil lithography is illustrated in figure 2.2.

Commercially available SiN membranes with a SiN thickness of 100 nm (Norcada NT025C) are sputtered with 10 nm of gold palladium ($Au_{60}Pd_{40}$ by weight) on both sides prior to FIB milling. This coating is done to prevent charging effects during FIB milling and SEM imaging. The SiN membrane is attached to the sample holder using a pressure mounted leaf spring. This avoids the use of double sided copper or carbon tape that can leave residues, which can clog the back side of the SiN wafer. The sample holder is then mounted in a dual column FIB/SEM

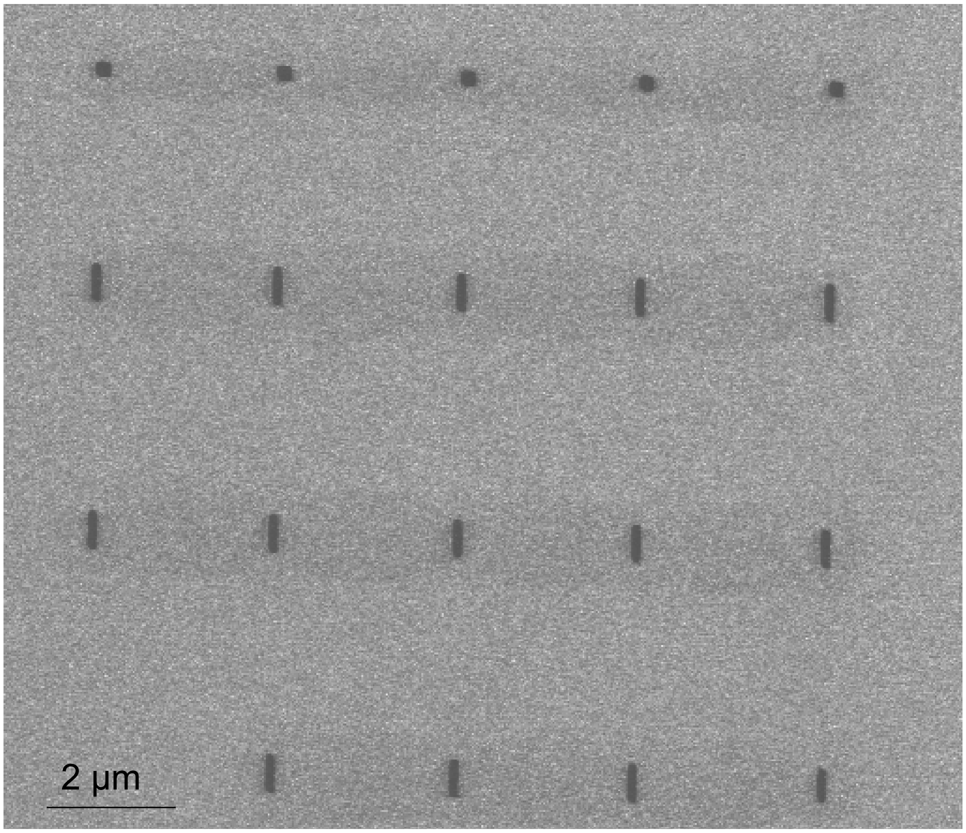

Figure 2.3: SEM image of stencil fabricated by FIB. The darker regions are the milled holes.

(FEI strata DB-235, 30 kV) and allowed to reach a base pressure of $\sim 5.5 \times 10^{-7}$ mbar. The electron column is turned on and the free standing SiN membrane is positioned under the dual column. The SEM is focused onto the SiN surface using a piece of dust or debris and the astigmatism is minimized. The FIB column is turned on, and the sample height adjusted so that the plane of the ion focus matches the plane of the electron focus at the sample surface. The sample is then tilted ($52°$) so that it is at normal incidence to the ion column. The desired milling region is located and the pattern is milled, as shown in figure 2.3. Generally beam currents of 10 and 30 pA are used with dwell times of 12 and 4 s/μm^2 respectively.

The substrate upon which nanostructures are deposited was chosen to be a free standing SiN membrane so that TEM can be performed on the samples. Permalloy ($Ni_{81}Fe_{19}$) is used due to its excellent magnetic properties. It has a high saturation magnetization ($M_S = 860$ kA/m) and a low coercivity (as low as 4 A/m) due to its near-zero magnetostriction [58].

The nanostructure shape was selected so that the magnetization is bistable, pointing in one of two orientations along the long axis. The nanostructures were designed to be 600 nm × 200 nm × 20 nm. For this shape, the magnetization should be confined to the plane of the substrate along the long axis of the nanostructure due to shape anisotropy (demagnetizing field).

Arrays were chosen to be approximately 10 μm × 10 μm so as to fit well within the piezo scan range (40 μm × 40 μm) for MFM imaging. The arrays are indexed with some of the elements missing so that individual structures can be identified and different arrays can be distinguished, as seen in figure 2.4. Arrays are separated by approximately 30 μm (as shown in figure 2.5) because the maximum scan range of the AFM is 40 μm. In a 40 μm × 40 μm scan it is impossible to have an empty image as long as the tip is positioned within the patterned area. This drastically reduces the time spent searching for the patterned area.

Individual element separation was determined using an analytical model for the interaction between neighbouring nanomagnets [109]. The magnetostatic energy per unit volume was calculated for different element separations as shown in figure 2.6. A structure is considered isolated when the magnetostatic energy per unit volume is 90% of the magnetostatic energy per unit volume of an isolated structure [109,110]. Due to potential broadening of the structures, 2 μm is used for the fabrication process. 2 μm is closer to 99% of the isolated magnetostatic energy per unit volume, which in retrospect, might have been larger than necessary.

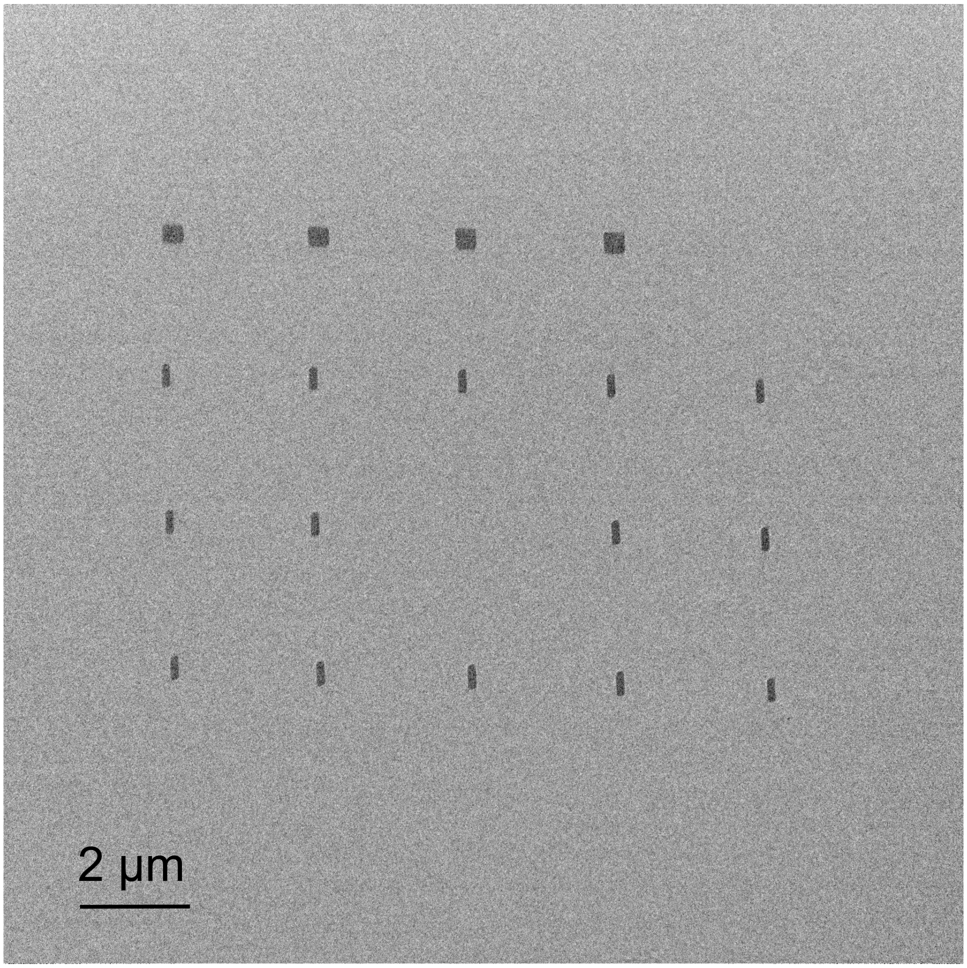

Figure 2.4: TEM image of an individual array of permalloy nanostructures (the darker features) showing indexing. Note that left and right, top and bottom can be distinguished even if sample is rotated or flipped.

After the milling is complete, the stencil is removed from the vacuum chamber and mounted on the sample membrane. To mount the stencil on top of another SiN membrane (as illustrated in figure 2.2), vacuum tweezers are attached to a micro manipulator stage that can move in x, y and z axes. The FIB fabricated nanostencil is flipped nitride side down onto a piece of filter paper. The vacuum tweezers are turned on, and the nanostencil is picked up from the silicon base using the vacuum tweezers. Two microscopes are used, along with the micro manipulator

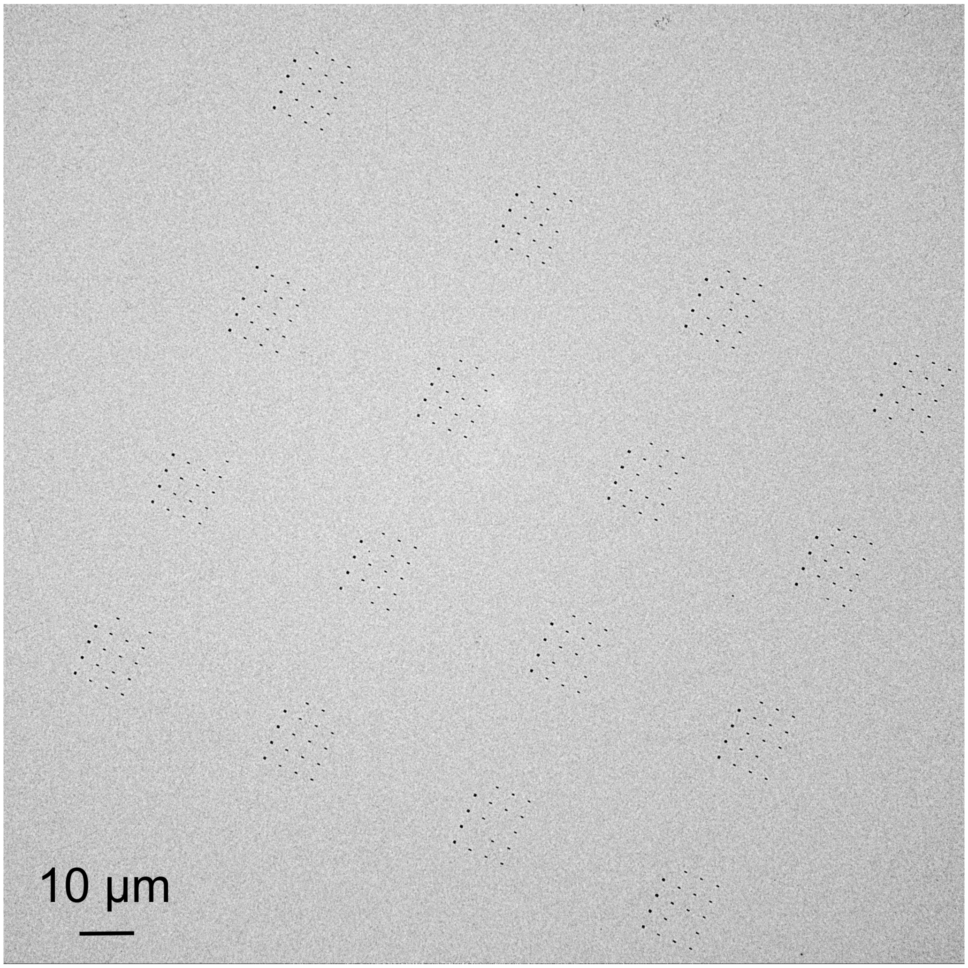

Figure 2.5: TEM image of a sample showing many arrays.

to position the nanostencil. One microscope gives a top view so that the stencil region can be aligned with the free standing portion of the SiN substrate, and the other is used to monitor the gap between the stencil and the substrate. When the stencil is properly positioned, the vacuum tweezers are turned off, allowing the stencil to fall onto the SiN membrane. This step is the largest source of error in the procedure as the stencil can move horizontally in an uncontrolled direction upon dropping. Despite the horizontal movement, misalignment is typically between 30 μm to 100 μm. This is an acceptable degree of misalignment as it allows the

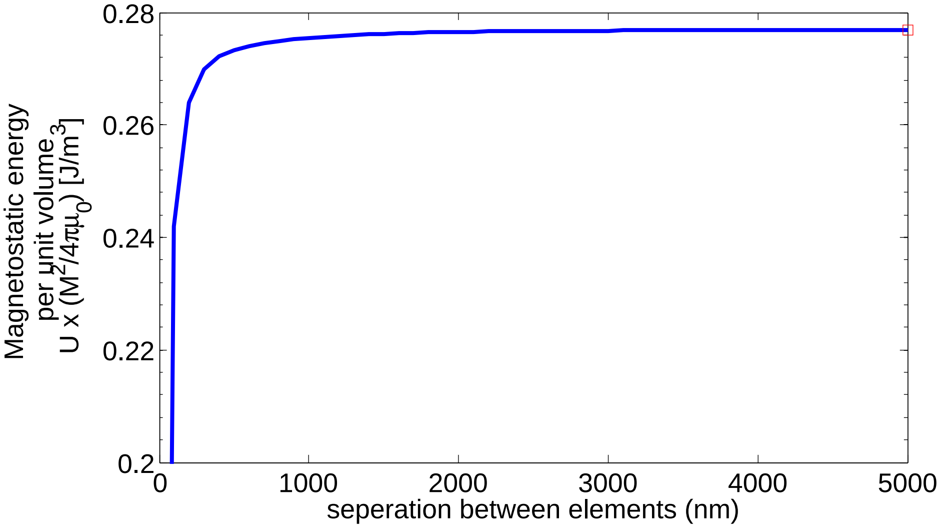

Figure 2.6: Magnetostatic energy per unit volume of an array of 600 nm × 250 nm × 25 nm element with 30 nearest neighbours. The red square represents a structure in isolation.

majority of the nanostructures to be located over the free standing portion of the SiN membrane. Tiny metal clamps are used to hold the nanostencil onto the SiN substrate. Figure 2.7 shows a typical alignment of the nanostencil over an unused clean SiN membrane.

The stencil and substrate assembly is taken to an electron beam evaporator where 20 nm of permalloy ($Ni_{81}Fe_{19}$) is evaporated, as illustrated in figure 2.2a. Before evaporation, the vacuum chamber is evacuated to a pressure of $\sim 6 \times 10^{-7}$ torr. An electron beam evaporator (BJD 1800, or an Omicron EFM3 electron beam evaporator) accelerates electrons onto an evaporation source (in this case a permalloy target). The source heats up, causing the material to evaporate, coating all objects in line of sight of the source. An evaporation rate of ~1 Å/s for the BJD 1800 evaporator and ~0.05 Å/s for the Omicron evaporator was used. The rate is measured using a quartz crystal microbalance. After deposition, the chamber is allowed to cool for an hour before it is vented to atmospheric conditions.

The stencil mask is removed from the SiN substrate by lifting the clamps holding the stencil on top of the substrate. The resulting permalloy nanostructures deposited on the lower membrane are shown in figure 2.4.

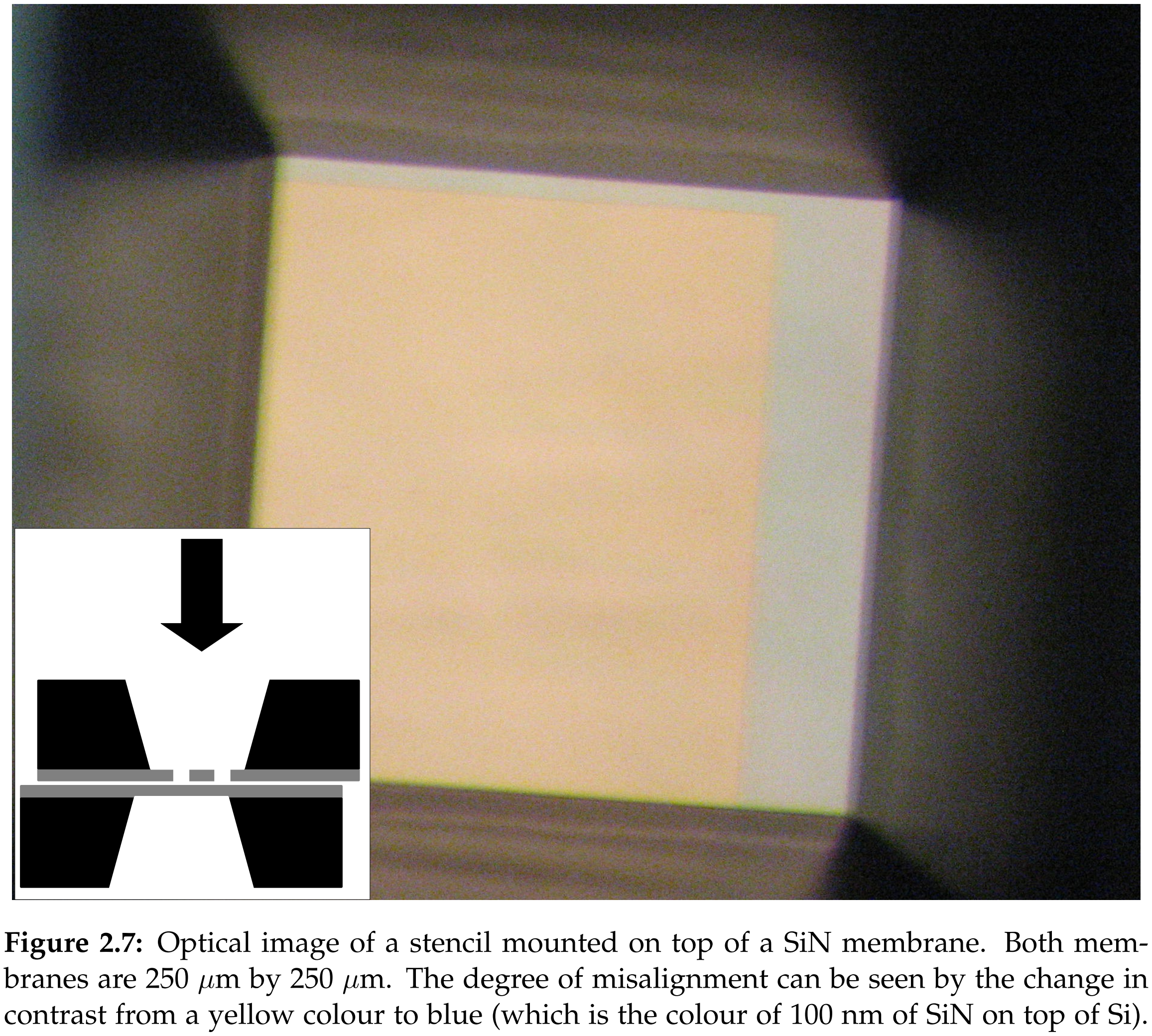

Figure 2.7: Optical image of a stencil mounted on top of a SiN membrane. Both membranes are 250 μm by 250 μm. The degree of misalignment can be seen by the change in contrast from a yellow colour to blue (which is the colour of 100 nm of SiN on top of Si). Inset is a schematic of the image.

2.3 Sample characterization

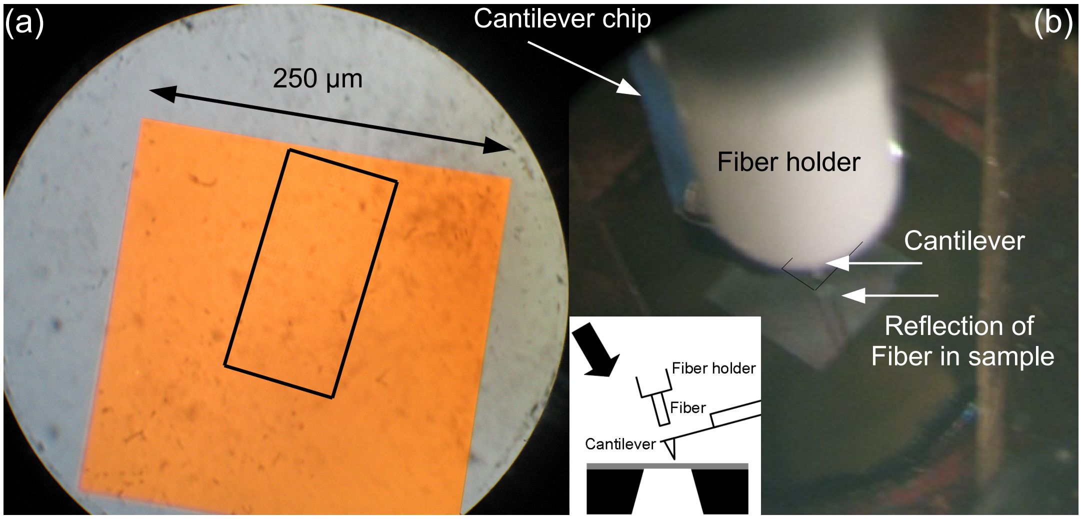

Figure 2.8: (a) Top view optical microscope image of nanostructure arrays with an outline to indicate the location of the nanostructures. The yellow region is the free standing SiN membrane and the blue region is SiN on top of silicon. (b) Sample in AFM/MFM with cantilever and fiber optic interferometer. This view is used to position cantilever in desired location. The white cylinder is the fiber optic interferometer holder (labeled fiber holder) at the bottom of which the end of the cantilever can be seen. The fiber optic interferometer can be seen in the reflection of the SiN membrane. The inset of (b) is a schematic of the picture shown in (b) with the arrow indicating the picture direction. This process is important for the proper positioning of the cantilever so days are not spent searching blindly for the desired areas.

The sample is placed in the MFM apparatus and a magnetic cantilever is positioned over the approximate region of the nanostructures by adjusting the stage position while monitoring the cantilever position using an optical microscope. This is an important step because after the chamber is evacuated an optical microscope can not be used to position the cantilever. Figure 2.8a shows an optical image of the approximate location of the arrays of nanostructures on a SiN membrane. The fiber optic interferometer is retracted so that the cantilever can be seen, as indicated by the arrow in figure 2.8b. The cantilever is then coarsely approached to $\sim$20 μm from the sample while visually monitoring the gap with an optical microscope. The fiber is re-approached to the cantilever using the fiber optic interferometer walker described in appendix A. A fine approach is then done to bring the cantilever into close proximity with the sample surface without damaging it. This involves retracting the sample and then approaching the microscope head by approximately half of the sample piezo range ($\sim$ 4 μm). The sample is then approached with the topography feed back turned on using the piezo tube that controls the sample position. If the cantilever does not interact with the sample, the piezo tube will be fully extended and the fine approach procedure is repeated until the cantilever is interacting with the sample.

After evacuating the system to a pressure between 1×10^{-5} mbar and 6×10^{-6} mbar to increase the Q factor of the cantilever, nc-AFM is used to find the nanostructures. To efficiently locate the nanostructures, large scans of the sample surface are made (40 μm $\times$ 40 μm) while minimizing the necessary number of scan lines. If the nanostructures are not within the initially imaged area, the x-y position of the sample is adjusted to an adjacent location, with each iteration spiraling out from the initial location. This search strategy maximizes the chances of finding the nanostructures, assuming that the initial alignment is reasonable. After the nanostructures are located, the sample tilt is corrected and an MFM scan is performed at a typical lift height of 70 nm.

2.3.1 Unexpected lack of magnetic force microscopy contrast

Figure 2.9 shows AFM and MFM images of an early permalloy nanostructure sample. The MFM image unexpectedly shows no magnetic contrast. MFM was repeated for many lift heights, cantilevers, applied magnetic field and sim-

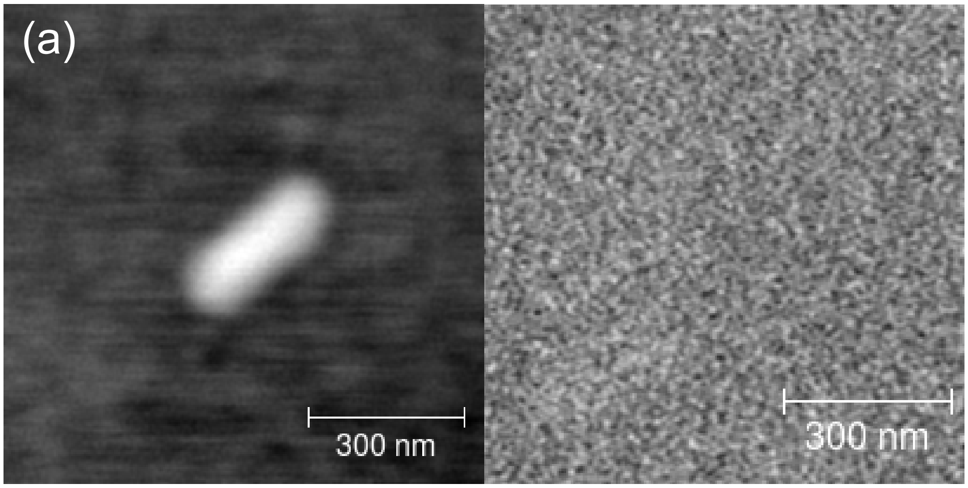

Figure 2.9: (a) AFM image of permalloy nanostructure fabricated by electron beam evaporation of permalloy though a FIB milled nanostencil. (b) MFM image of same structure. Note lack of contrast described in section 1.3.

ilarly prepared samples to rule out these factors influence on the MFM contrast. MFM cantilevers were also used to image a control MFM sample both before and after imaging to rule out the possibility of cantilever damage causing the lack of magnetic contrast. Every nanomagnet that was fabricated using electron beam evaporation of permalloy though a FIB milled nanostencil (more than 30 samples with more than 10 nanostructures measured per sample) showed no MFM contrast.

Understanding the cause of the absence of MFM contrast when imaging these permalloy nanostructures took a great deal of time and many different experimental techniques.

2.3.2 X-ray photoelectron spectroscopy

XPS was used to rule out the possibility that the lack of MFM contrast on permalloy nanostructured array samples was caused by oxidation of the depos-

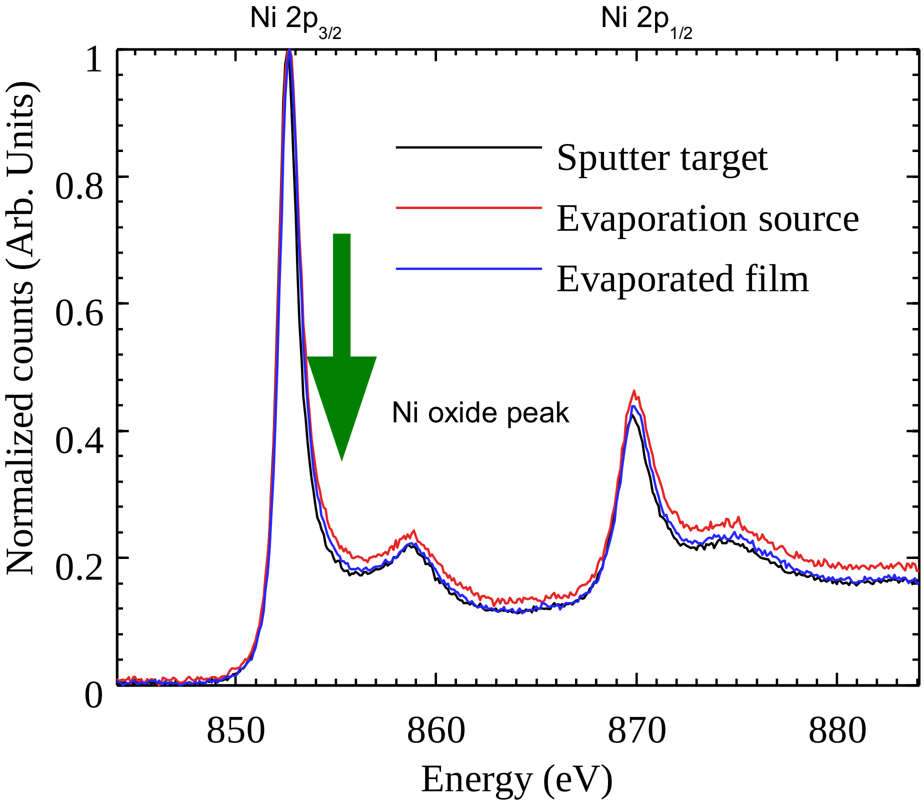

Figure 2.10: Nickel XPS of three different samples. A sputter target, evaporation source and a film made using electron beam evaporation are represented by the black, red and blue lines respectively. The width of the green arrow represents the location of nickel oxide peaks but none are present within the error of the measurement.

ited film either during or after deposition. A 20 nm permalloy film deposited on a piece of silicon oxide at the same time as a sample deposition was analyzed. Figure 2.10 shows that both nickel peaks (Ni $2p_{3/2}$ and Ni $2p_{1/2}$) are clearly visible without any nickel oxide peaks above the noise level. The surface contamination is sputtered away prior to the XPS measurement, as permalloy is known to have a protective oxide layer at the surface that is not representative of the bulk properties [111]. Similarly, figure 2.11 shows both iron peaks (Fe $2p_{3/2}$ and Fe $2p_{1/2}$) as well as a nickel Auger peak. There are no iron oxide peaks above the noise level of the measurement. The lack of iron and nickel oxide peaks indicates that the bulk permalloy film has not oxidized during or after film deposition and therefore is not the cause of the lack of MFM contrast in figure 2.9.

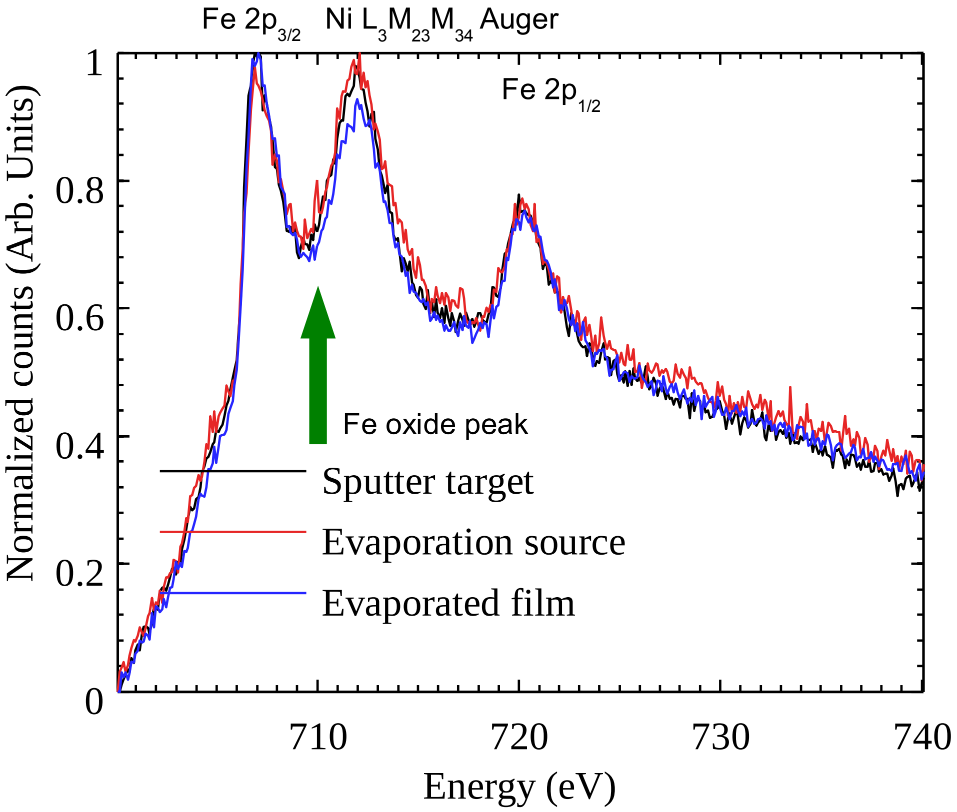

Figure 2.11: Iron XPS of three different samples. A sputter target, evaporation source and a film made using electron beam evaporation are represented by the black, red and blue lines respectively. The width of the green arrow represents the location of iron oxide peaks but none are present within the error of the measurement.

2.3.3 Magneto-optic Kerr effect

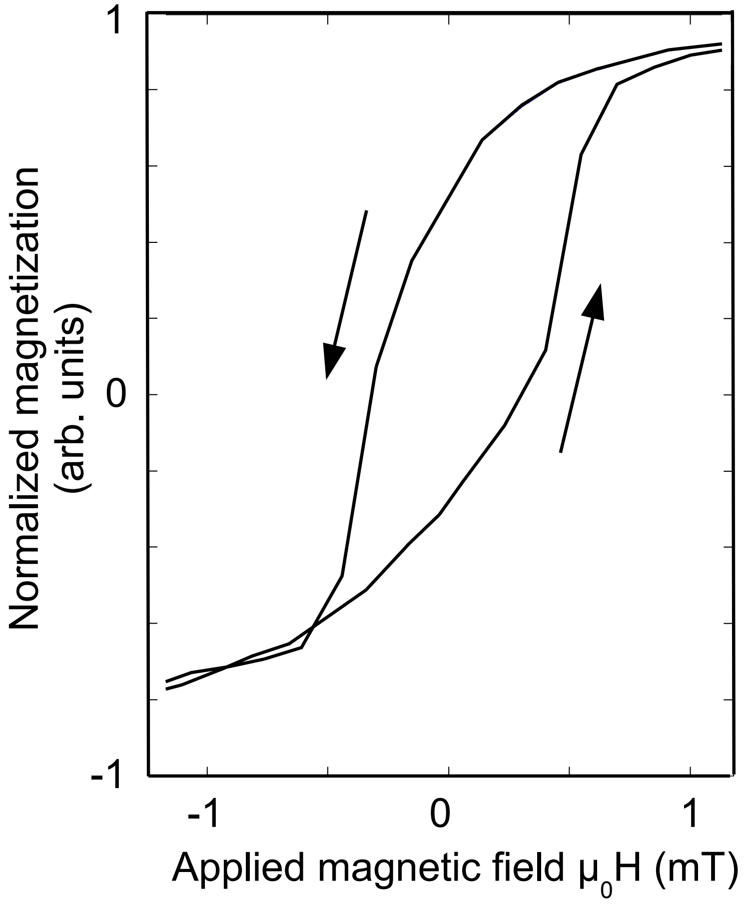

Figure 2.12: MOKE measurement of a 20 nm electron beam evaporated permalloy film on silicon oxide substrate. Only data near the switching field is shown.

The bulk film was also analyzed using MOKE to confirm that the permalloy film was magnetic. Figure 2.12 shows a MOKE curve of a 20 nm permalloy film on silicon oxide, deposited at the same time as nanostructures made using a FIB milled stencil that showed no MFM contrast. A coercivity of 275 A/m was measured, which is close to the expected coercivity of permalloy on silicon (160 ± 30 A/m [112]). The MOKE data shows that the bulk film is magnetic and has a reasonable coercivity, but MFM measurements (shown in figure 2.9) of nanostructures made during the same deposition have no contrast. This suggests that something unique occurs to the permalloy that passes through the nanostencil mask.

2.3.4 Transmission electron microscopy

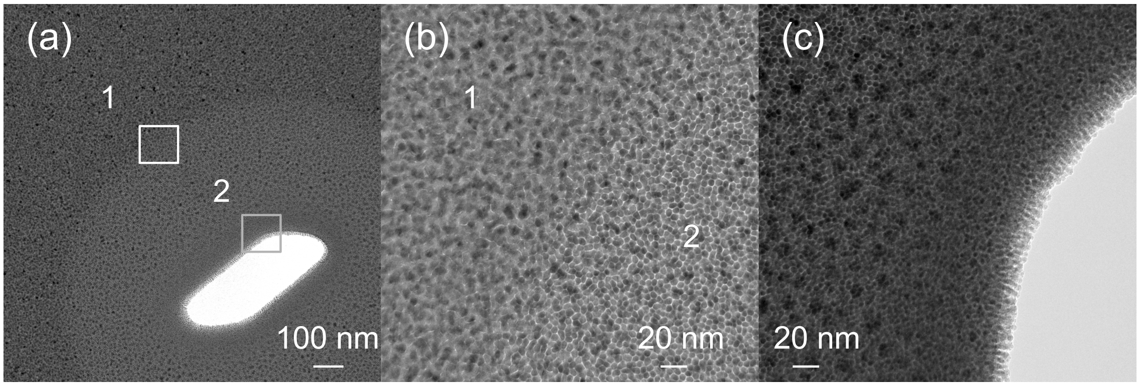

Figure 2.13: TEM images of nanostencil mask made by FIB milling after deposition of 20 nm of permalloy. (a) Shows a hole in the SiN membrane (white region) and two distinct permalloy growth regions labeled zones 1 and 2. (b) is a zoom in on the white box in (a). (c) is a zoom in on the gray box in (a). Note that the columnar growth can be seen along the edge of the hole.

The nanostencil and nanostructures that showed a lack of contrast in MFM were then analyzed by TEM. Surprisingly, TEM of the the nanostencil revealed two very distinct growth modes of the permalloy film, labeled zones 1 and 2, shown in figure 2.13. Zone 2 appears to be a non-continuous film of columnar grains grown perpendicular to the SiN surface plane, whereas zone 1 appears to consist of polycrystalline grains that are in contact with one another. The nanostructures that were fabricated by deposition through this nanostencil are shown in figure 2.14. These nanostructures have the same growth structure as zone 2 of the film deposited on the stencil mask shown in figure 2.13.

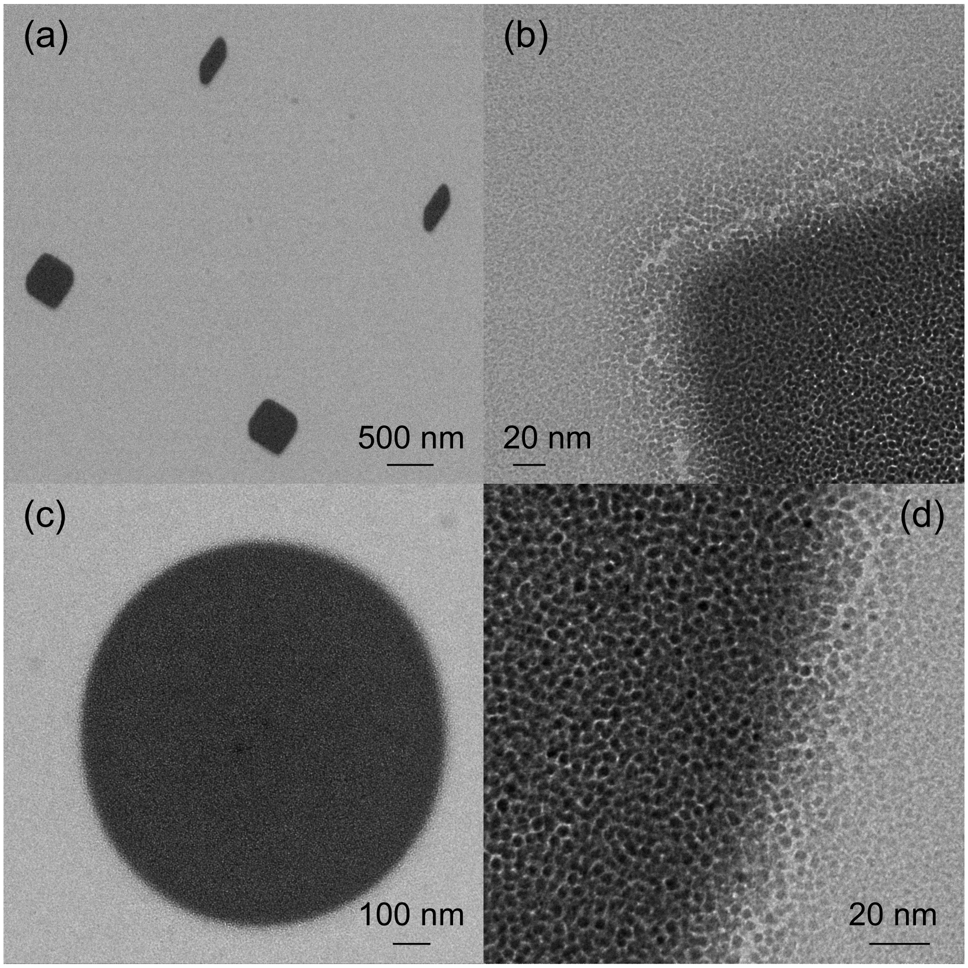

Figure 2.14: Bright field TEM image of permalloy nanostructures on SiN membrane made using nanostencil shown in figure 2.13. (b) is a zoom in on a structure shown in (a). (c) is a 1 μm diameter permalloy dot. (d) is a zoom in on the structure shown in (c).

A 1 μm diameter circular hole was included in the nanostencil so that a proper comparison could be made between the resulting deposited permalloy dot and a control sample (figure 2.14c). A control permalloy nanostructure sample was made by electron beam evaporating permalloy though a commercially available SiN nanostencil (Protochips DTM-25232, SiN thickness 200 nm) that was fabricated using conventional photolithography (PL) instead of FIB. The control stencil consists of 1 μm diameter holes in a SiN membrane. A TEM image of the control

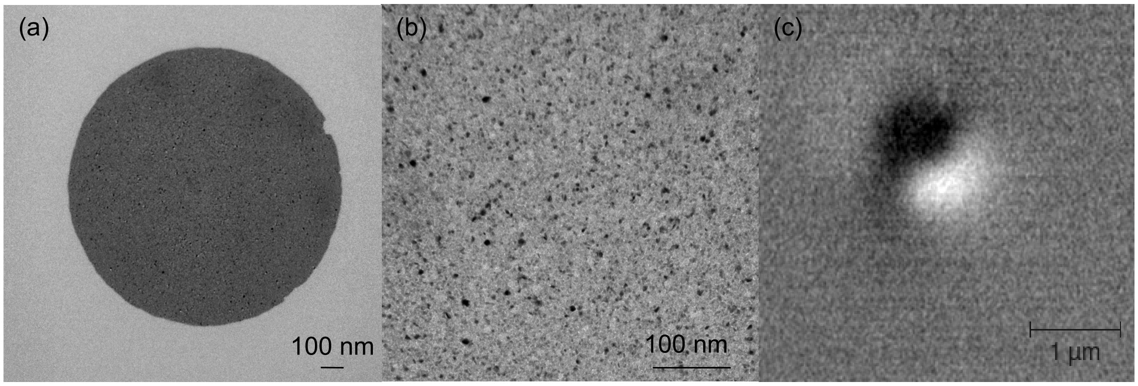

Figure 2.15: (a)Bright field TEM images of a 1 μm diameter, 20 nm thick permalloy structure on SiN membrane, fabricated using stencil mask made by conventional photolithography. (b) zoom in on (a), note the permalloy growth mode is similar to zone 1 shown in figure 2.13 (far from the milled area). (c) MFM image of structure in (a). The external applied in-plane magnetic field was 60 mT and a lift height of 100 nm. The z-scale frequency shift is -5.5 Hz to 6.5 Hz.

sample (shown in figure 2.15b) reveals similar permalloy growth structure as in zone 1 of the stencil shown in figure 2.13. The control sample was imaged with MFM and clear magnetic contrast was obtained, as shown in figure 2.15c.

Because the control sample shows clear MFM contrast and the XPS of the permalloy film shows the expected composition, we may conclude that the surprising structure and magnetic behaviour of permalloy nanostructures deposited though a FIB milled nanostencil is not due to the e-beam evaporation source (or nanostencil lithography deposition in general). Instead, it seems to depend upon the technique with which the nanostencil mask was fabricated. Commercially available PL stencils are not available in the shape and layout necessary for our experiment therefore, the mechanism by which FIB milled nanostencils influence permalloy growth must be investigated and mitigated.

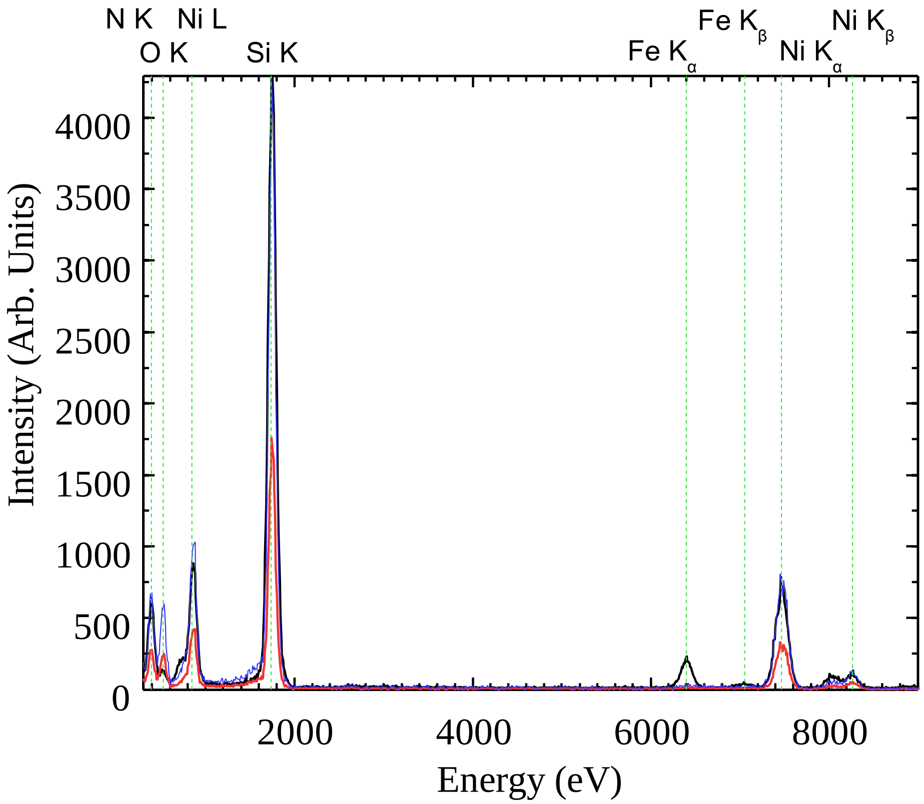

Figure 2.16: EDX data of (red) permalloy nanostructures evaporated though a FIB milled stencil, (black) permalloy nanostructures evaporated through a PL stencil. Blue represents the data from the FIB milled stencil scaled so that the silicon peak matches that of the PL stencil. The green vertical dashed lines represent known element transition [77]. The nanostructure made with the FIB milled stencil shows significantly less iron than the nanostructure made using the PL stencil.

2.3.5 Energy-dispersive X-ray spectroscopy

To understand the differences between the nanostructures made using FIB and those made using a PL stencil, the chemical composition was measured using EDX, as shown in figure 2.16. The resulting chemical composition is shown in table 2.1. The chemical composition of the evaporation source used was $Ni_{81}Fe_{19}$. Note that the chemical composition of the nanostructures made using the FIB milled stencil is equal (within error) to the chemical composition of the permalloy film near the milled hole on the FIB milled stencil (zone 2). The iron content is much lower than expected. The chemical composition of the nanostructure made with a PL stencil is equal (within error) to the permalloy film on the FIB milled stencil far from the milled hole (zone 1).

All of the EDX measurements detect iron above the minimum mass fraction calculated using equation 1.39. Therefore, not all iron is removed when using the FIB milled nanostencil. Notably, EDX measurements taken directly adjacent to the milled hole also detect that gallium is implanted in the FIB-milled SiN membrane.

Table 2.1: Relative composition of nickel to iron, measured using EDX of nanostructure and nanostencil after permalloy deposition using two different fabrication techniques. The composition of the permalloy evaporation source was $Ni_{81}Fe_{19}$.

Measurement location	FIB-milled	Photolithography
Stencil close to hole	$Ni_{97\pm2}Fe_{3\pm2}$	$Ni_{88\pm4}Fe_{12\pm4}$
Stencil far from hole	$Ni_{88\pm2}Fe_{12\pm2}$	$Ni_{88\pm3}Fe_{12\pm3}$
Structure	$Ni_{98\pm3}Fe_{2\pm3}$	$Ni_{88\pm3}Fe_{12\pm3}$

2.3.6 Electron energy loss spectroscopy

To verify the low iron content of the permalloy nanostructure made using a FIB milled nanostencil, EELS was also used, as shown in figure 2.17. Iron was not detected (within error) in the nanostructures deposited though a FIB milled stencil. The chemical composition of the nanostructures made with a PL stencil was found to be $Ni_{77\pm3}Fe_{23\pm3}$. This nickel deficiency is expected for electron beam evaporated permalloy due to differences in the partial pressures of permalloy vapor compared to bulk permalloy [114].

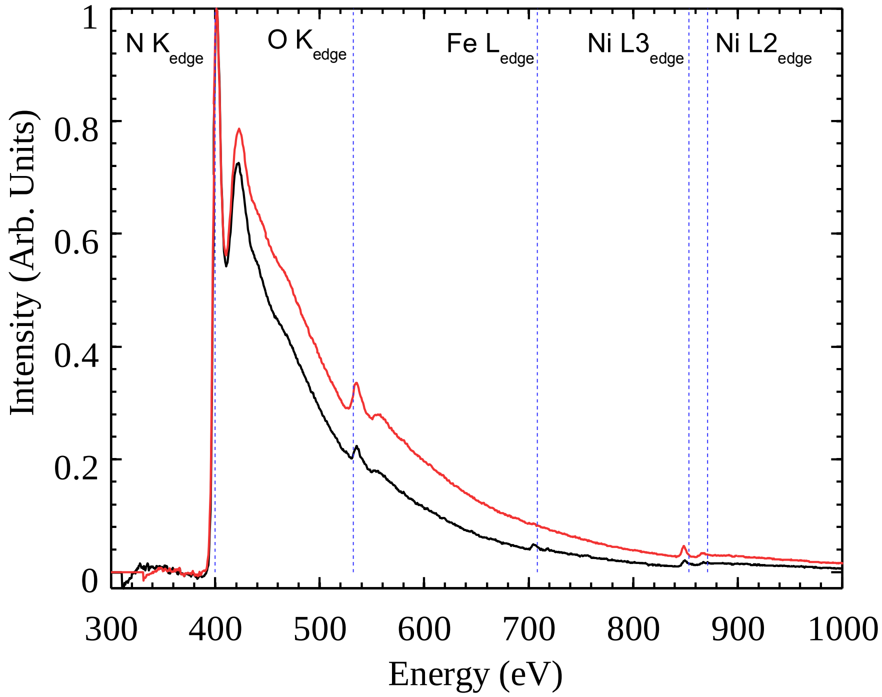

Figure 2.17: EELS with background subtracted of: red permalloy nanostructures evaporated through a FIB milled stencil, black permalloy nanostructures through a stencil made using a PL stencil. Blue represents location of labeled elements [113]. Measurement and background subtraction done at the Canadian Center for Electron Microscopy at McMaster University.

EELS also revealed that the nanostructures made with the FIB milled stencil have approximately 3 times the oxygen content of those made with the PL stencil. The oxygen content measured on the bare silicon nitride sample substrate was identical for the two samples within error. The presence of additional oxygen in the nanostructure fabricated using a FIB milled stencil suggests that the lack of magnetic contrast may be the result of partial oxidization of the remaining Ni, because NiO is antiferromagnetic.

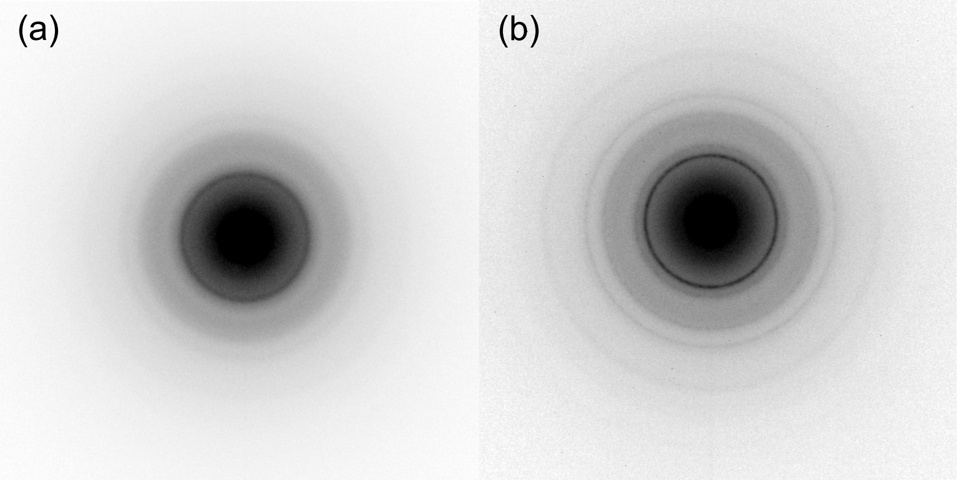

Figure 2.18: Selected area electron diffraction with contrast inverted. Scale for each image is 16.5 mmÅ(a) SAED of nanostructure made with FIB milled stencil. (b) SAED of nanostructure made with PL fabricated stencil.

2.3.7 Electron diffraction

To analyze the film structure, selected area electron diffraction (SAED) images of permalloy nanostructures made using FIB and PL nanostencils are shown in figure 2.18. Figure 2.19 shows the SAED image radially averaged with the background subtracted. The (1,1,1) peak of each line in figure 2.19 is fit to a Lorentzian function. The full width at half max (FWHM) of the nanostructure made with the FIB nanostencil is similar to that of the permalloy film deposited on the nanostencil near the milled holes, at 0.070 ± 0.001 Å^{-1} and 0.067 ± 0.001 Å^{-1} respectively. The FWHM of the nanostructure made with the PL stencil is close to that of the permalloy film deposited on the FIB milled nanostencil far from the milled holes, at 0.034 ± 0.001 Å^{-1} and 0.038 ± 0.001 Å^{-1} respectively.

The increase in FWHM of the (1,1,1) peaks could be a result of a decrease in grain size [115] of the permalloy grains, or a result of the presence of NiO, which has peaks within 0.03 Å^{-1} on both sides of the permalloy (1,1,1) peak. The

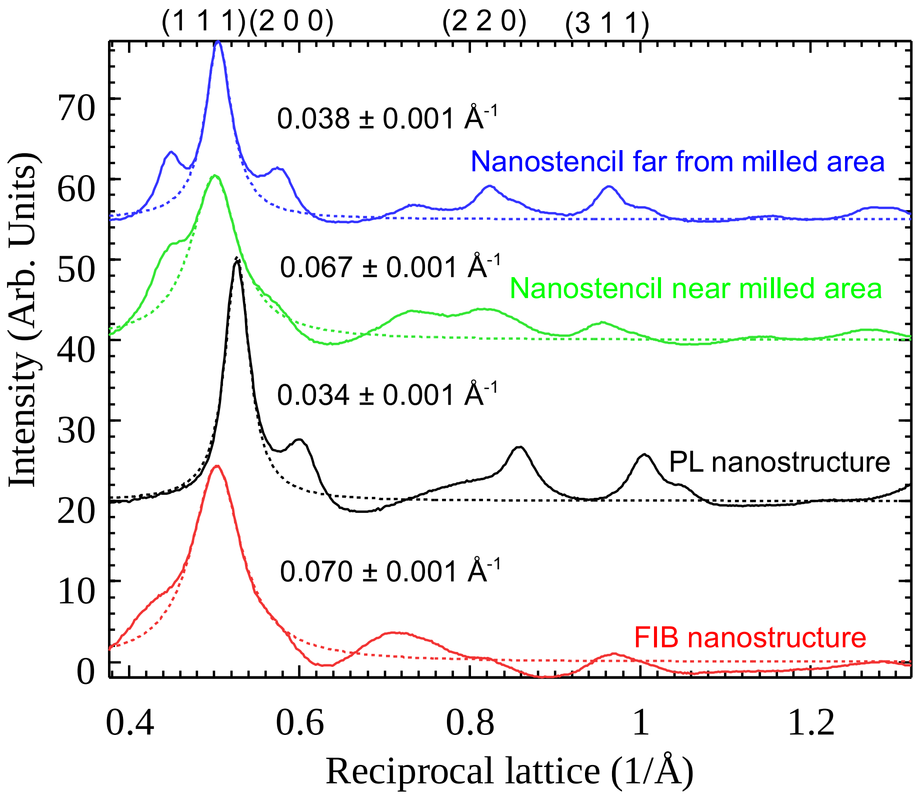

Figure 2.19: Selected area electron diffraction, radially averaged with background subtracted. Dotted lines represent fit to 111 peak. FWHM values of dotted lines are displayed next to each fit. The crystallographic planes corresponding to each peak is labeled at the top of the figure.

increased oxygen content measured with EELS also suggests that the broadening may be due to the presence of NiO. Because NiO is antiferromagnetic this could also explain the lack of magnetic contrast in the nanostructures made with a FIB milled nanostencil.

2.3.8 The possible influence of implanted gallium ions

An electric field surrounding milled features in the FIB milled nanostencil may cause the drastic change in structure and function of the deposited permalloy nanostructures. Electric fields are known to influence permalloy film growth [116] and gallium ions have been shown to implant around FIB milled areas [85,86]. We propose that an electric field may originate from the implanted gallium ions that are found around the edges of FIB milled regions. This possibility is supported by the fact that the structure of the deposited permalloy film on the nanostencil around regions that are milled using the FIB (zone 2) is comparable to that of nanostructures deposited though the FIB milled nanostencil. Both are deposited in close proximity to the Ga ions.

To confirm that the implanted gallium is ionized, and therefore able to create such an electric field around the FIB milled nanostencil features, Kelvin probe force microscopy (KPFM) was used [37, 117]. KPFM is a dynamic AFM mode wherein the tip-sample bias is adjusted during imaging such that the contact potential difference between the tip and sample is minimized at each point (minimization done using another control loop and a lock-in amplifier). This produces a map of local contact potential difference (LCPD) on a surface, which relates to work function [31].

Simultaneously acquired nc-AFM topography and KPFM LCPD are shown in figure 2.20. A variation in the LCPD can be observed in a circular area 1.1 ± 0.2 μm in diameter surrounding the FIB milled area shown in figure 2.20b. The dark region is attributed to positive gallium ions (implanted during the FIB milling process) and the white ring is attributed to electrons screening the gallium ions in the 10 nm thick AuPd layer.

We propose that unscreened the gallium ions surrounding FIB milled nanostencil features create an electric field that is perpendicular to the plane of the stencil. Because electron beam evaporation is not a neutral process [118, 119], we sug-

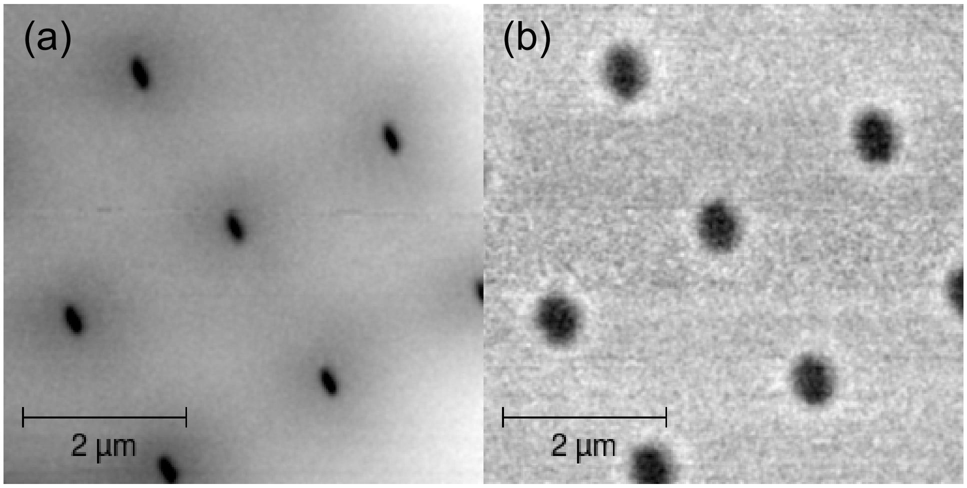

Figure 2.20: Simultaneously acquired (a) nc-AFM topography image of nanostencil with a z-scale of 150 nm and (b) KPFM image with a z-scale of 1 V. Black represents positive charges and white represents negative charges in the KPFM image.

gest that charged evaporated species are affected by the electric field, causing the difference in permalloy growth observed for FIB nanostencil deposited nanostructures and of the film on FIB milled nanostencils surrounding milled features.

This electric field could also induce polarization in the film and depositing permalloy during deposition. Such polarization may encourage growth along the electric field direction, perpendicular to the surface. Figures 2.13 and 2.14 support this claim as the grains of the affected regions appear to be circular, indicating columnar growth of the permalloy film perpendicular to the substrate.

Oxidization in nickel thin films is normally a self-limiting process [120]. The increased oxidization of FIB stencil deposited nanostructures observed by EDX and EELS may be the result of increased oxygen and nickel cation diffusion along the boundaries of the permalloy columns. Oxygen and nickel cation diffusion rates are known to be higher along grain boundaries and cracks [121]. The increased mobility may have allowed the formation of additional antiferromagnetic NiO and the resulting lack of MFM contrast.

2.4 FIB workaround

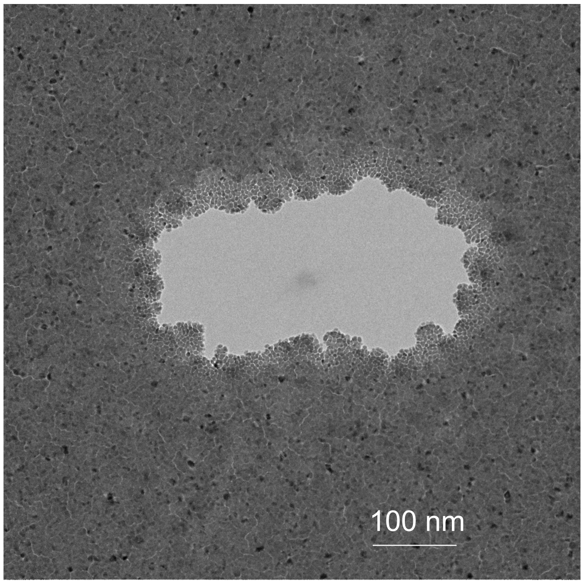

Figure 2.21: TEM image of stencil after reactive ion etching and permalloy deposition.

In an attempt to remove some of the implanted Ga, SiN nanostencils were reduced in thickness using a reactive ion etch (RIE) [122]. Before nanostencils are introduced into the RIE chamber, the chamber is cleaned with an oxygen plasma etch. After cleaning the chamber, the SiN stencil is placed so that it straddles two small pieces of double sided Kapton tape. This is done so that the space behind the free standing membrane is not sealed with air at atmospheric pressure before the chamber pressure is reduced to 50 mTorr, potentially rupturing the stencil. The chamber pressure and plasma are allowed to equilibrate while Ar is introduced at 100 standard cubic centimeters per min (sccm). Next, CHF_3 and O_2 gas are introduced at rates of 50 sccm and 6 sccm respectively. This results in a stencil etching rate of approximately 1.6 nm/s. After etching for 37 seconds, the SiN membrane is approximately 40 nm thick. The remainder of the procedure described in section 2.2 is repeated to deposit permalloy nanostructures.

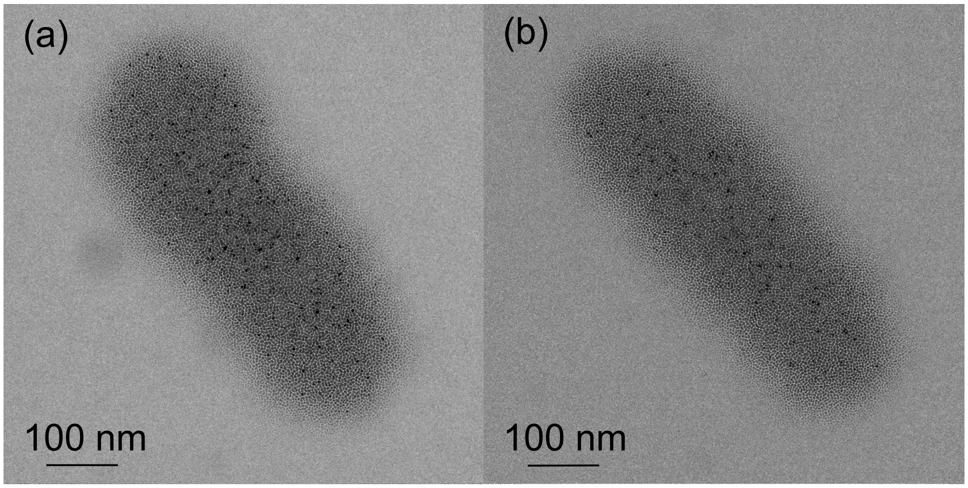

Figure 2.22: TEM images of permalloy nanostructures deposited though a FIB milled nanostencil that was thinned using RIE. Non-uniform etching of the stencil mask during RIE results in structures (a) and (b).

Figure 2.21 shows an RIE thinned nanostencil after permalloy deposition. Unfortunately, the etching is not uniform. This results in the deposition of nanostructures that are far from identical, as shown in figure 2.22. The etching non-uniformity may also be related to the presence of gallium, which has previously been shown to resist etching in silicon [123]. The RIE procedure does not change the permalloy film structure mode from the previous columnar growth in affected areas shown in figure 2.14, most likely because not all Ga is removed. Fortunately, the chemical composition measured by EDX is found to be $Ni_{89\pm4}Fe_{11\pm4}$, which is equal (within error) to the composition of the film far from the milled areas in table 2.1.

The deposited nanostructure sample was then imaged in MFM (as shown

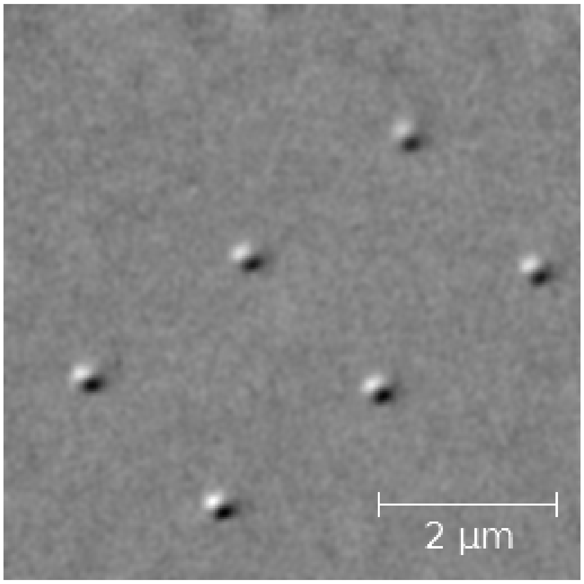

Figure 2.23: MFM image of permalloy nanostructures. Nanostructures are fabricated by electron beam evaporation of permalloy though a FIB milled stencil that is thinned using a reactive ion etch. Cantilever lift heigt was 120 nm in a 60 mT applied magnetic field.

in figure 2.23). At long last, clear MFM contrast is revealed.

The goal in thinning the SiN membranes was to reduce the amount of implanted gallium in hopes that it would reduce the influence on permalloy nanostructure growth though FIB milled nanostencils. The resulting deposited nanostructures were found to have a chemical composition that was equal (within error) to the chemical composition of the bulk film and showed magnetic contrast in MFM. However, the grain structure of the nanostructures still appeared similar to the previous FIB deposited structures, rather than the uninfluenced growth demonstrated by the nanostructures made with the PL stencil. It is therefore unclear if the proposed model is the correct one, but having finally developed a procedure for fabricating magnetic permalloy nanostructures, we now move on to SFD characterization.

3

Switching field distribution of permalloy nanostructure arrays

3.1 Results

The switching field distribution of permalloy nanostructures deposited through a FIB milled, RIE thinned nanostencil was measured using magnetic force microscopy. A TEM image of the analyzed array is shown in figure 3.1.

The procedure for measuring the switching field is as follows: A field of 60 mT was applied to the nanostructures along their long axis so that the magnetization of the structures was saturated and well-defined. An MFM image was taken and the magnetization direction of each nanostructure was recorded. The field was decreased and another image was taken, recording the magnetization direction of each nanostructure and the applied magnetic field. Hall probes measure the amplitude of the applied magnetic field. This process was repeated until all the nanostructures were saturated in the opposite direction they started in. The field was then saturated in a -60 mT field and the procedure was repeated but in the opposite direction.

The lift height of each image was as high as possible (while still having enough signal to noise to determine the magnetization direction) so as to minimize

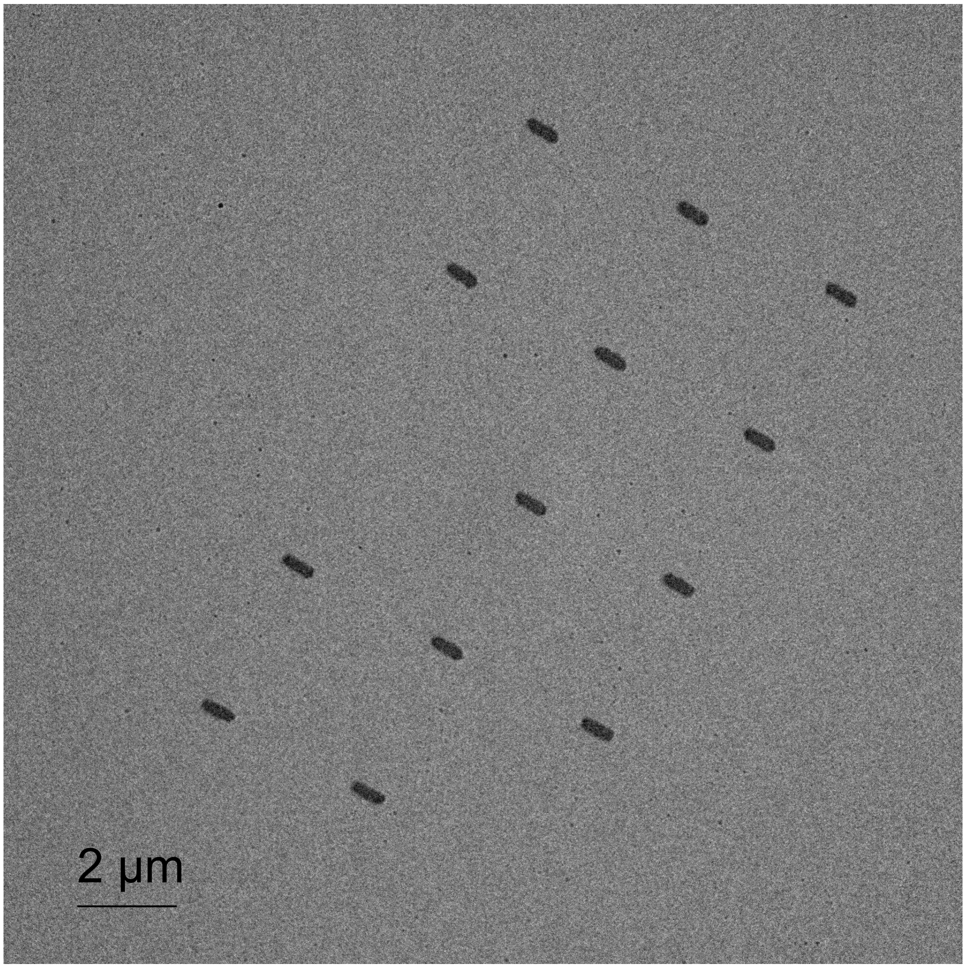

Figure 3.1: Transmission electron microscopy image of array of permalloy nanomagnets. Some structures are missing by design to help identify the array as well as the individual structures.

the influence of the tip on the nanostructures. A lift height of 400 nm was used as this was the highest lift height that the magnetization direction could be reliably inferred from the MFM scans after image processing (shown in figure 3.2).

The hysteresis loop of the array shown in figure 3.1 was done 4 times and the resulting data for the array of nanostructures is shown in figure 3.3. In figure 3.3, $M = 1$ indicates that the magnetization direction of all 13 nanostructures is pointing in one direction and $M = -1$ indicates that the magnetization direction

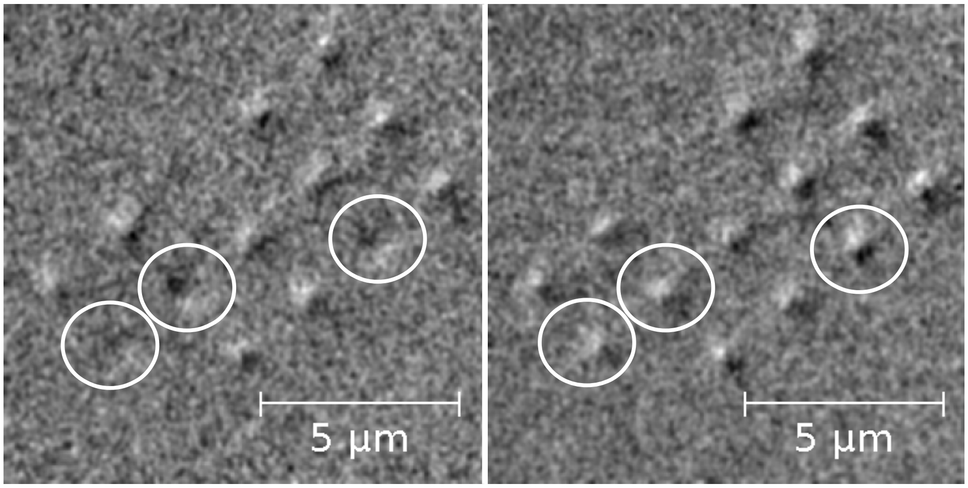

Figure 3.2: Magnetic force microscopy images show 3 structures, circled in white, switch their magnetization direction between images as the applied magnetic field is increased. Lift height of both images is 400nm.

of all 13 nanostructures is pointing in the opposite direction. The magnetization reversal order was identical for each loop. In other words, the same nanostructure switched first in each loop and the same structure switched last in each loop. A variation of switching field of an individual magnets was not observed. To observe such a distribution the size of the applied magnetic field steps would have to be drastically reduced while taking many more hysteresis loop cycles. The coercivity of the 13 nanostructures (measured values and error in these values are obtained from the fit shown in figure 3.3) was found to be 0.72 ± 0.03 mT with a switching field distribution of 0.40 ± 0.07 mT. A thin film that was deposited at the same time as the 13 nanostructures had a coercivity of 0.2 mT, as measured by MOKE. The switching field of an individual nanostructure is shown in figure 3.4.

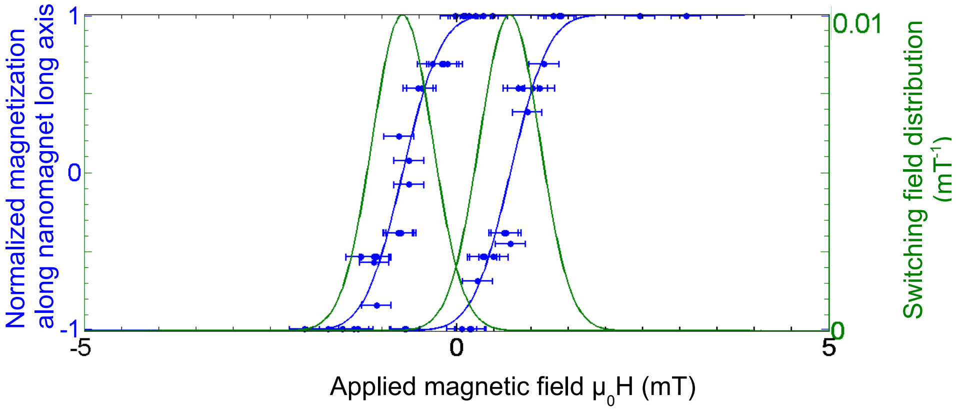

Figure 3.3: Normalized mean magnetization as a function of applied field for 13 nanostructures shown in figure 3.1 (blue data points). Error bars are from the uncertainty in the measurement of the applied field. The blue curve is an error function fit to the blue data points. The green curve is the switching field distribution.

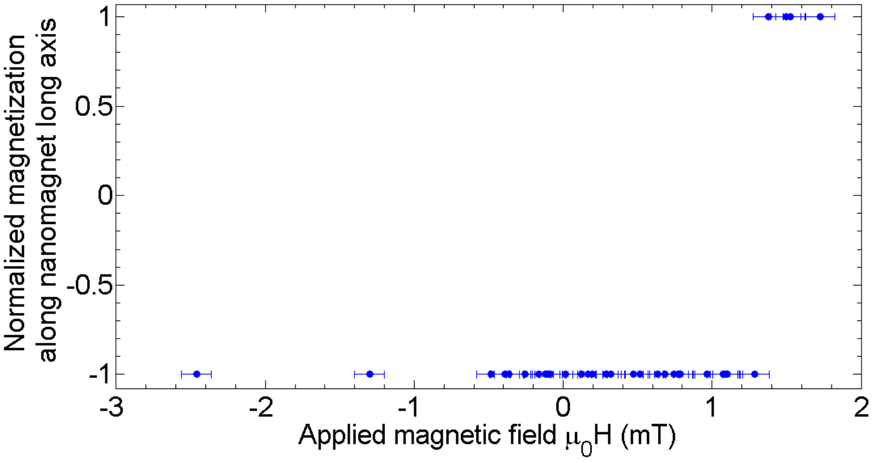

Figure 3.4: Normalized magnetization as a function of applied field for nanostructure in row 2 column 2 shown in figure 3.1. Error bars are from the uncertainty in the measurement of the applied field. This nanostructure has a coercivity of 1.3 ± 0.1 mT.

3.2 Analysis of nanostructure SFD

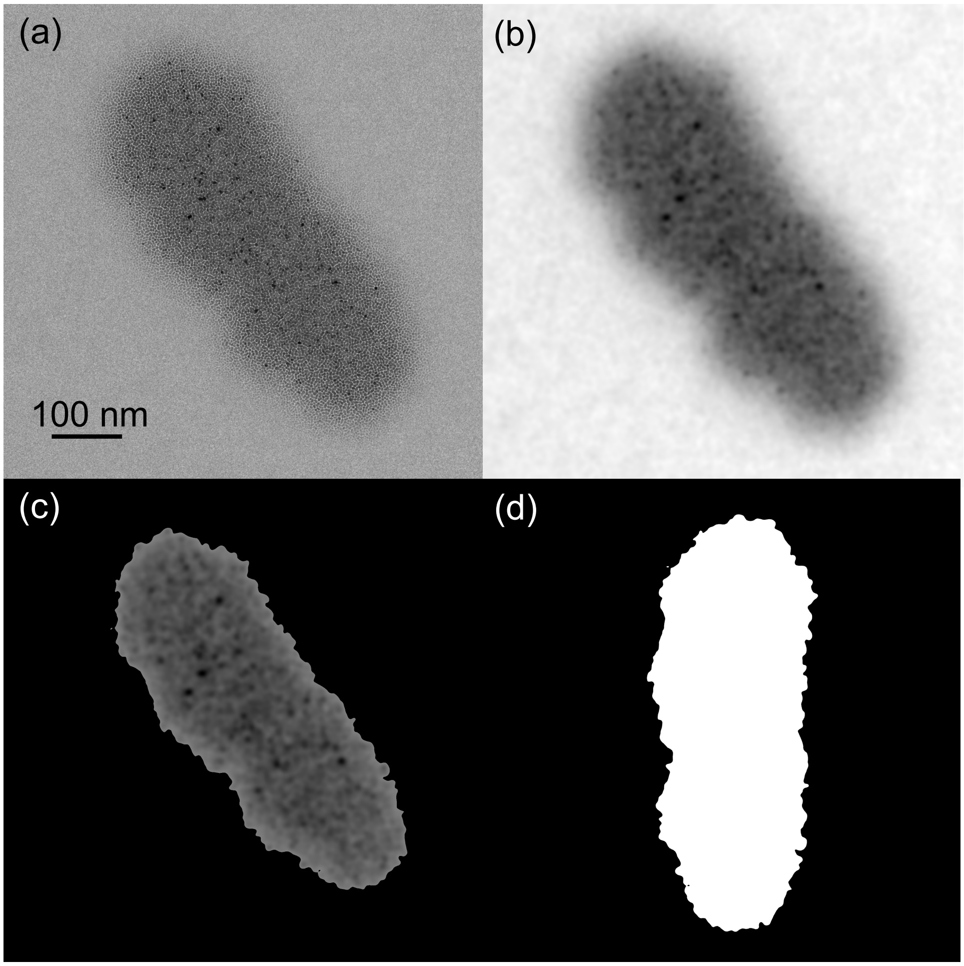

Figure 3.5: (a) TEM image of a permalloy nanostructure. (b) TEM image convolved with Gaussian with width approximately equal to the exchange length in permalloy. (c) Result of edge finding algorithm performed on (b). (d) The length, width and roughness was measured and calculated. Horizontal field of view is 675 nm for each image.

Now that we have measured the switching fields of an array of nanomagnets, we seek to understand what causes the distribution in switching field. Bright field, diffraction and dark field TEM images were taken for each nanostructure (shown in figure 3.1) so that physical characteristics of the nanomagnets could be compared to the switching field.

To determine the shape of each nanomagnet, bright field TEM images were used. The TEM images shown in figure 3.5a were smoothed by convolving the TEM image with a Gaussian with a width approximately equal to the exchange length in permalloy, resulting in an image shown in figure 3.5b. This was done so that the edges of the nanostructures could be reliably located. The nanostructure was defined as the region with more than half of the contrast in the smoothed TEM images. This region is shown in figure 3.5c for one of the nanostructures. These images were then used to estimate the length, width and edge roughness of each structure (described in detail below). All bright field TEM images as well as edge detection are given in appendix B.

3.2.1 Influence of shape on switching field

The aspect ratio (length/width) was calculated and compared to the switching field for each nanomagnet as shown in figure 3.6. The slope of the best fit line is 1.3 ± 0.5 mT with an offset of -3 ± 1 mT. The aspect ratio data does not depend directly on the demagnetizing field, and as a result, does not capture the reversal mechanism properly, and should only be used as a estimate of how aspect ratio influences switching field.

A better comparison of the influence of shape (length and width) on magnetic reversal behaviour is to use Stoner-Wohlfarth analysis (equation 1.30). The finite length shape anisotropy factor was calculated for each structure. The reliability of the shape anisotropy factor measurement was determined by calculating the shape anisotropy factor at a series of thresholds for each nanostructure, as shown in figure 3.7. The finite length shape anisotropy factor was found to change uniformly for each nanostructure. The error in finite length shape anisotropy factor

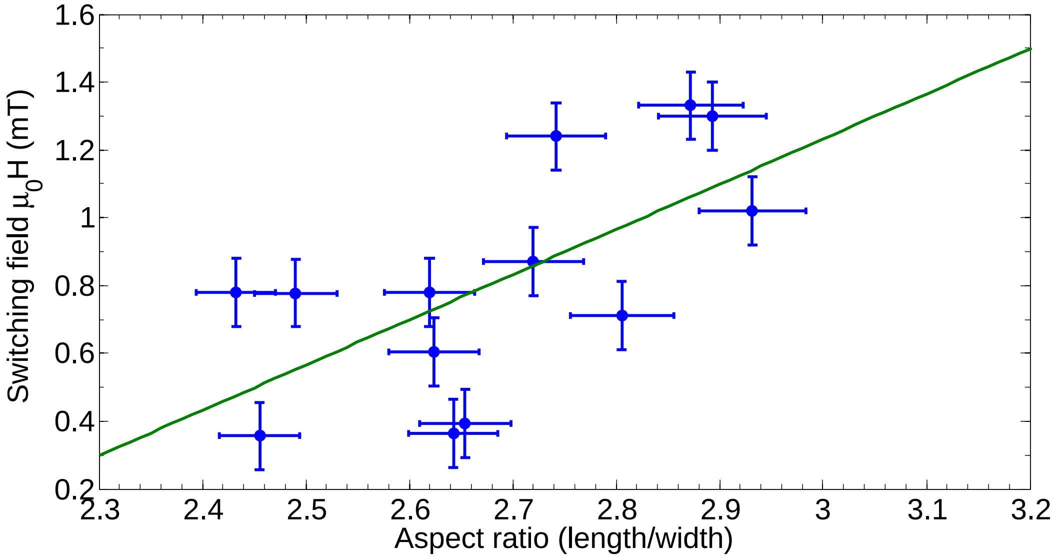

Figure 3.6: Switching field vs. Aspect ratio (length/width) of permalloy nanostructures.

was calculated assuming that the error on the length and width was the width of the Gaussian used to smooth the images (4 nm).

The switching field was plotted versus the finite length shape anisotropy factor as shown in figure 3.8. The colours in figure 3.8 indicate structures with similar finite length shape anisotropy factors. According to Stoner-Wohlfarth analysis (equation 1.29), the data in figure 3.8 should be linear, passing though the origin. While more data is clearly needed for a robust analysis, the slope and y-intercept of the data in figure 3.8 are 1000 ± 400 mT nm and -3 ± 1 mT respectively.

Stoner-Wohlfarth analysis assumes coherent rotation of the magnetization during magnetization reversal. This assumption does not hold for the room temperature nanostructures studied here. It has been previously shown by Schneider et. al. [124] that when the reversal is not coherent rotation, the coercivity remains linearly related to the Stoner-Wohlfarth calculated coercivity but with a different proportionality. They found that this proportionality was approximatly 0.55 for

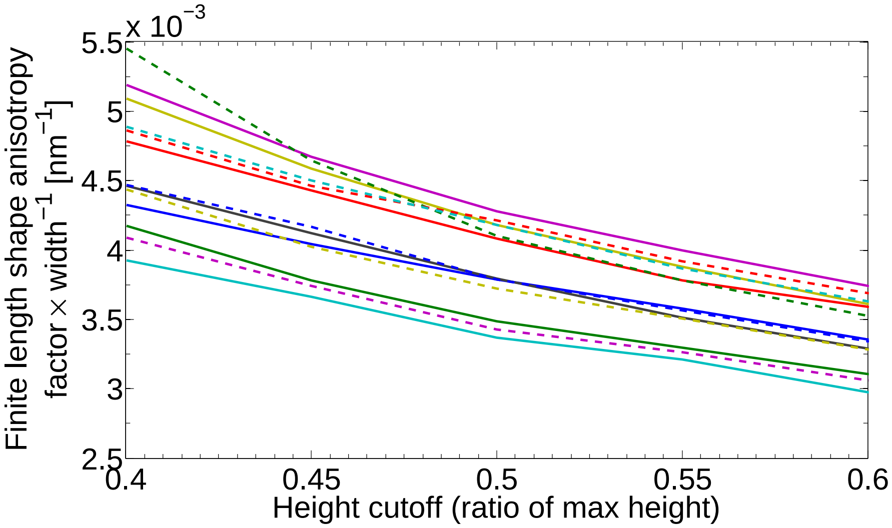

Figure 3.7: Finite length shape anisotropy factor of nanostructures for different threshold values of the edge detection algorithm.

permalloy ellipses that were 15 nm thick [124].

OOMMF was used to estimate the tip stray field, which is a possible cause of the measured offset in y-intercept of figure 3.8. A rectangular NiCo structure, 12.5 μm long (the length of the tip), 35 nm thick (thickness of the NiCo coating) and 80 nm wide (from the approximate tip radius [125]) was simulated with the tip magnetization along the length. The stray magnetic field 400 nm below the tip is found to have a maximum of ±1.5 mT along the cantilever axis (x-axis) and 3.5 mT along the long axis of the tip (z-axis). These values agree within two standard deviations to the y-intercept in figure 3.8.

When the saturation magnetization is calculated from the slope of the fit to figure 3.8 using Stoner-Wohlfarth analysis (equation 1.29), a value of 60 ± 20 kA/m is obtained. This is drastically less than the saturation magnetization value of permalloy, which is 860 kA/m and can not be explained by deviation from Stoner-Wohlfarth type switching, because it differs by more than an order of mag-

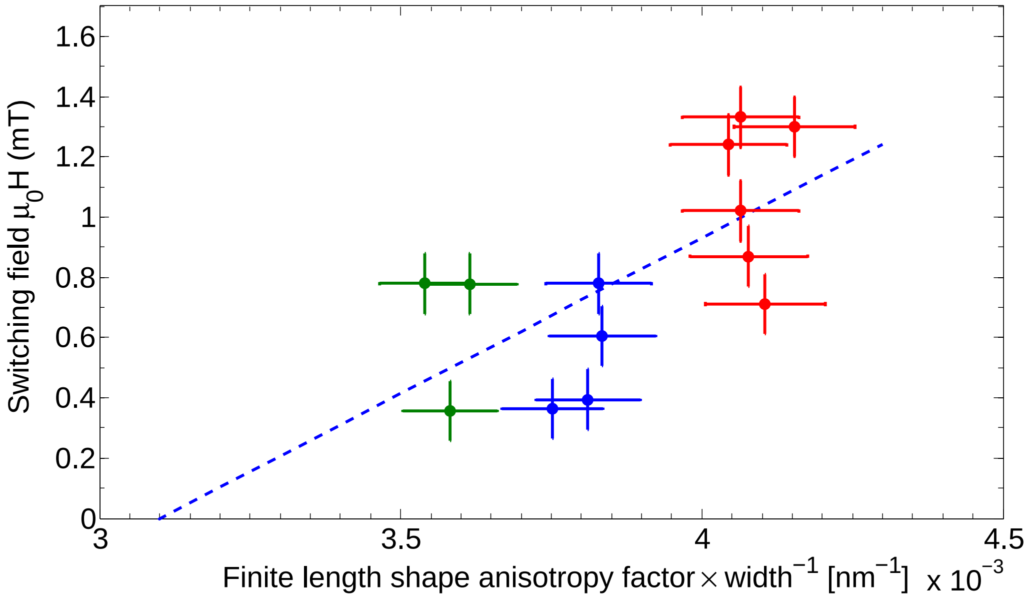

Figure 3.8: Switching field vs. finite-length shape anisotropy factor/width. Colour indicates structures with similar finite length shape anisotropy factors.

nitude. The calculated value of the saturation magnetization is further evidence that thinning the membrane by RIE does not completely resolve the issues caused by FIB milled nanostencils, but more data is required to be certain.

The linear relationship between switching field and finite length shape anisotropy factor indicates that variations in the length and width influence the demagnetizing field, which in turn influences the switching field.

3.2.2 Edge roughness

To determine the influence of edge roughness on the switching field, the edge roughness was estimated for each structure. The edge of the nanostructures was measured using the bright field TEM images (shown in appendix B) and the edge detection procedure described above in section 3.2. The roughness was obtained by measuring the RMS edge deviation from a rectangular element nano-

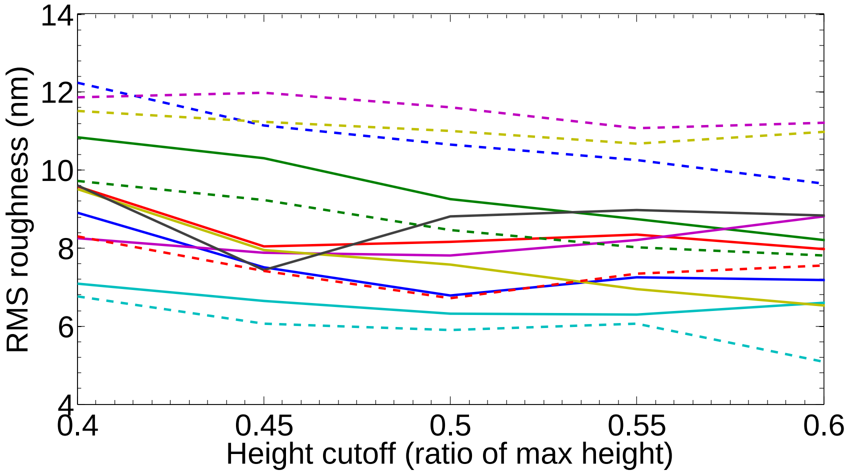

Figure 3.9: RMS edge roughness of nanostructures for different threshold values of the edge detection algorithm.

structure. Figure 3.9 shows the nanostructure roughness for each structure in the array (shown in figure 3.1) calculated at different height thresholds. The error in edge roughness was estimated from the variation in the RMS edge roughness over the threshold range 0.4 to 0.6.

The structures were sorted into colour-coded groups with constant (within experimental error) shape anisotropy factors and the switching field was plotted versus the RMS edge roughness, shown in figure 3.10. The two structures with the highest roughness and lowest switching fields circled in figure 3.10 are shown in figure 3.11. Note that each structure has a large defect along the right edge.

To study the influence of large defects on the side of elliptical magnetic nanostructures on switching field, many OOMMF simulations were performed with defects of various sizes at different locations on the edge of the ellipse. Circular defects of 10 nm, 20 nm and 40 nm in diameter at 11 different locations on the edge of the ellipse (starting at the left side and finishing on the right side, with

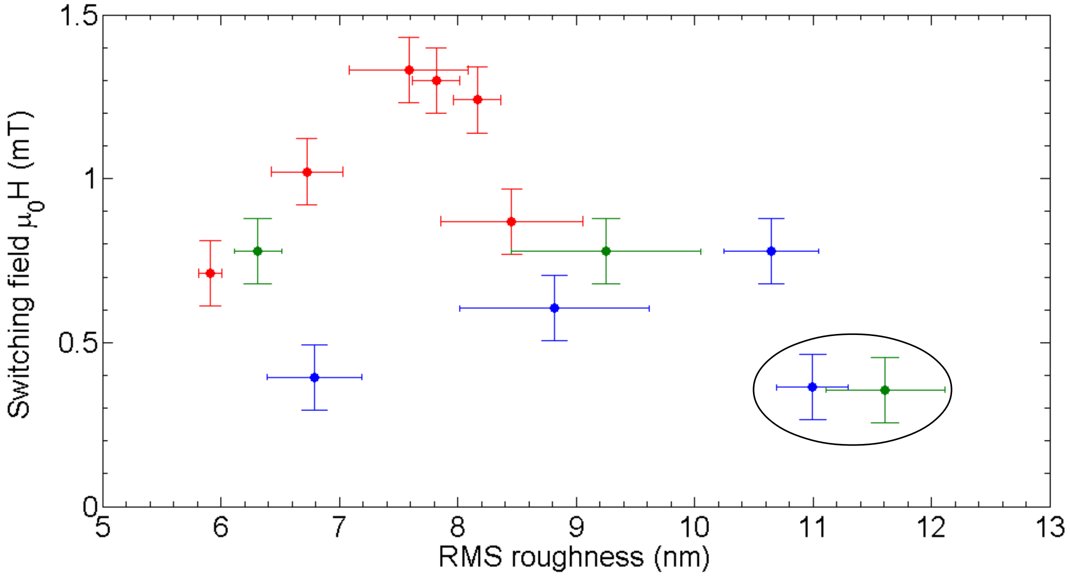

Figure 3.10: Switching field vs. root mean squared roughness. Red, blue and green represent the high, medium and low finite length shape anisotropy factors shown in figure 3.8. The two circled data points represent structures with large defects which, according to OOMMF simulations, reduce the switching field.

regular angular spacing) were simulated. Figure 3.12a shows one of the simulated nanostructures, a 40 nm defect on the edge of an ellipse that is 525 nm by 175 nm. Figure 3.12b and c show the magnetization configuration just before and just after the magnetization is reversed. Other than defects located at the exact end of the long axis of the nanostructure, defects of similar size show a similar effect on the switching field. The switching field was also shown to decrease with increasing defect diameter as shown in table 3.1.

The remaining data in figure 3.10 suggests that switching field increases with increasing RMS roughness, but clearly more statistics are needed to make a definitive statement about the trend. Switching field has been shown in the literature to increase with an increase in edge roughness in permalloy nanostructures [15, 16, 19]. This is thought to occur because of the demagnetizing effect. At

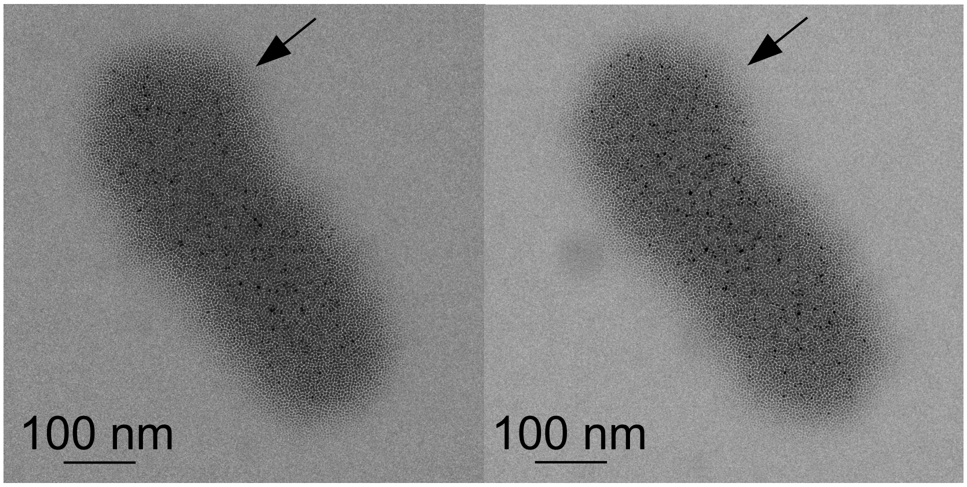

Figure 3.11: TEM images of two structures from circled data points in figure 3.10. Note that each structure has a large defect in the top right.

Table 3.1: OOMMF simulations of nanomagnet coercivity for varying defect size and location on a 525 nm× 175 nm×20 nm permalloy ellipse.

Defect position relative to long axis (rad)	μ_0H$_C$ of 10 nm defect (mT)	μ_0H$_C$ of 20 nm defect (mT)	μ_0H$_C$ of 40 nm defect (mT)
$\pi/2$	76.5	58	45.5
$2\pi/5$	46.5	45	43.5
$3\pi/10$	46.5	46.5	42.5
$\pi/5$	46.5	46	43.5
$\pi/10$	46.5	46.5	45.5
0	66	76.5	76.5

large applied magnetic fields, the magnetization is thought to be fairly uniform throughout both rough and smooth nanostructures. As the applied magnetic field approaches the switching field, the magnetization in structures with rough edges rotates slightly to minimize the stray field. The energy required to rotate the magnetization along the rough edges otherwise may have been used to nucleate the reversal [15,16,19], and therefore the switching field is increased.

In the case of the OOMMF simulation, the magnetization rotation occurs mainly in the region of the large defect as shown in figure 3.12b. But, rather than

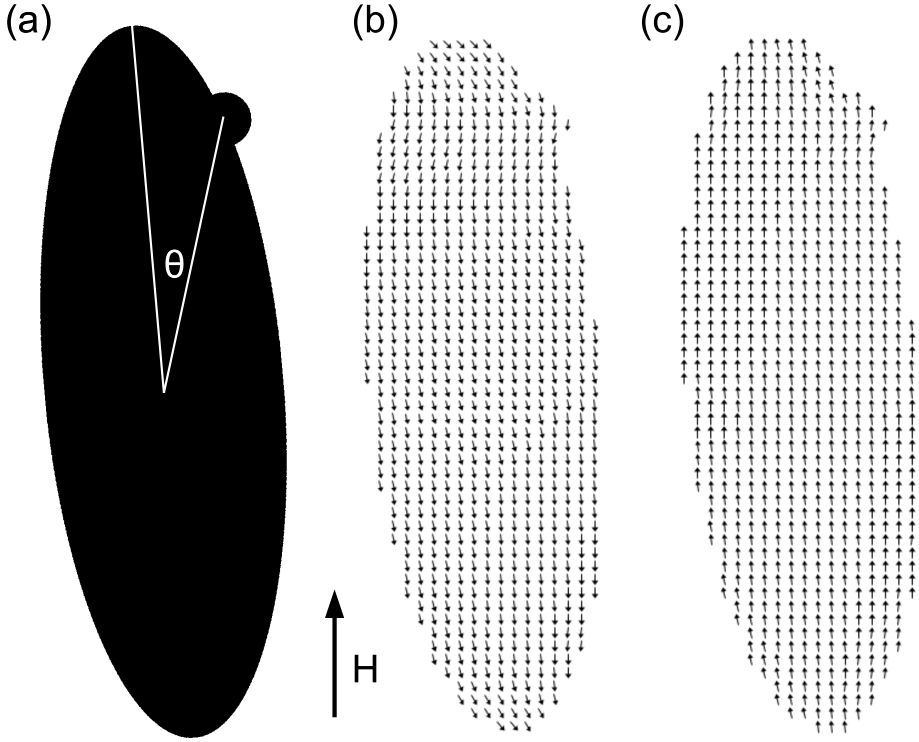

Figure 3.12: Simulated structures are 525 nm × 175 nm × 20 nm. (a) Mask for OOMMF simulation with a 40 nm wide defect. θ is the defect location angle. (b) Magnetization distribution before magnetization reversal. (c) Magnetization distribution after magnetization reversal. For images (b) and (c) individual vectors represent an average of the magnetization within region of the vector.

increasing the switching field, the large defect appears to decrease it. It is possible that because the magnetization in the region near the large defect requires a significant local rotation when the applied magnetic field is near the switching field (to minimize stray magnetic field). The energy that would otherwise be evenly distributed to minimize the stray field for all rough edges of a structure is concentrated in one location. This concentrated region of magnetization rotation might reduce the energy barrier required to nucleate a magnetization reversal.

3.2.3 Other factors

Interaction between neighbouring magnetic nanostructures can also increase SFD [23] but, as discussed in section 2.2, the nanostructures explored here are separated enough that the variation in the magnetostatic energy is negligible.

In Co/Pd dots, SFD is thought to be caused by varying grain orientation, and therefore varying magnetocrystalline anisotropy, within the nanostructure [24]. The magnetocrystalline anisotropy of permalloy is close to zero and therefore crystallographic orientation should not affect the switching field as the magnetocrystalline energy is negligibly low.

The sample analyzed in this chapter was sent to the Canadian center for electron microscopy at McMaster University for Lorentz mode TEM characterization. This measurement was designed to confirm that the distribution of the switching field was not influenced by the stray field from the MFM tip. Unfortunately, no Lorentz mode TEM contrast was visible. This may have been due to the low saturation magnetization of the sample and the sensitivity of the Lorentz mode TEM not being high enough.

3.3 Summary

The switching field of nanomagnets with similar finite length shape anisotropy factors were compared to their edge roughness as measured by TEM. More experimental results are needed to make conclusive statements regarding the impact of edge roughness and finite length shape anisotropy factor on the switching field distribution, but the results proposed here suggest that there may be an increase in switching field with an increase in edge roughness for nanostructures

Table 3.2: Table of switching field data.

(Row, Column)	Switching field (mT)	Width (nm)	Length field (nm)	$\frac{\text{Length}}{\text{Width}}$	Shape anisotropy factor/Width (nm^{-1})	Edge roughness (nm)
(1,2)	0.4 ± 0.1	212±3	562±3	2.65±0.04	0.0038±0.0001	6.8±0.4
(1,3)	0.8 ± 0.1	223±3	556±3	2.49±0.03	0.0036±0.0001	9.3±0.8
(1,4)	1.2 ± 0.1	200±3	547±3	2.74±0.04	0.0040±0.0001	8.2±0.2
(1,5)	0.8 ± 0.1	228±3	555±3	2.43±0.03	0.0035±0.0001	6.3±0.2
(2,1)	1.3 ± 0.1	194±3	562±3	2.89±0.04	0.0042±0.0001	7.8±0.2
(2,2)	1.3 ± 0.1	199±3	571±3	2.87±0.04	0.0041±0.0001	7.6±0.5
(2,3)	0.6 ± 0.1	211±3	552±3	2.62±0.04	0.0038±0.0001	8.8±0.8
(2,4)	0.8 ± 0.1	211±3	552±3	2.62±0.04	0.0038±0.0001	10.6±0.4
(2,5)	0.9 ± 0.1	198±3	539±3	2.72±0.04	0.0041±0.0001	8.5±0.6
(3,1)	1.0 ± 0.1	199±3	582±3	2.93±0.04	0.0041±0.0001	6.7±0.3
(3,2)	0.7 ± 0.1	197±3	552±3	2.81±0.04	0.0041±0.0001	5.9±0.1
(3,4)	0.4 ± 0.1	225±3	553±3	2.46±0.03	0.0036±0.0001	11.6±0.5
(3,5)	0.4 ± 0.1	215±3	569±3	2.64±0.04	0.0038±0.0001	11.0±0.3

with similar finite length shape anisotropy factors.

4

Advances in magnetic force microscopy

4.1 Tip induced artifacts in magnetic force microscopy

While imaging an array of 20 nm thick, 1 μm diameter permalloy dots on a SiN membrane using magnetic force microscopy, an interesting tip-related artifact was observed.

The dots were fabricated by evaporating permalloy though a nanostencil made using standard photolithography, which circumvents the effect of gallium implantation on permalloy growth as discussed in section 2.3. The magnetization of the dots were saturated by applying a 60 mT in-plane magnetic field.

4.1.1 Observation of MFM ring over permalloy dot

The permalloy dot sample was scanned using a smart tip (SC-35-M) cantilever with a spring constant of 2.8 N/m and a resonance frequency of 67.5 kHz. The cantilever had a quality factor of approximately 10000 under high vacuum conditions at room temperature.

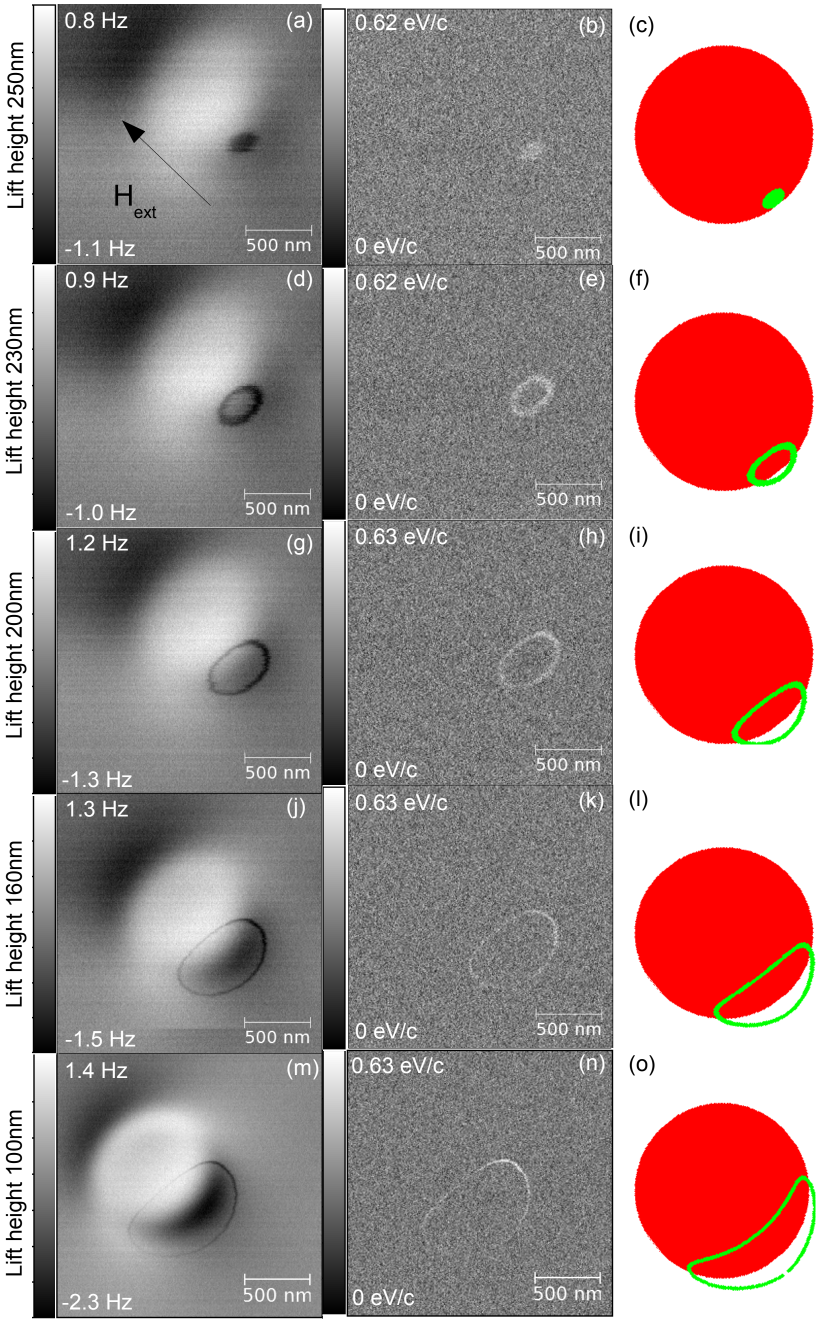

Figure 4.1: MFM frequency shift, dissipation and OOMMF simulation of stray magnetic field of permalloy dot on SiN membrane (left, center and right columns respectively). Note ring in frequency shift and dissipation channels. Oscillation amplitude is 10 nm with a lift height indicated on the left of each image row. All frequency shift and dissipation images are taken in an applied field of 60 mT. OOMMF simulation shows the x-y location where the z component of the stray field from the is equal to -14± 0.3 mT.

When the MFM tip was lifted above a dot and scanned, an artifact was observed in the MFM frequency shift and dissipation channels, as shown in figure 4.1. The left column is the frequency shift signal and the centre column is the dissipation signal. Note that the rings found in the dissipation channel were also found in the frequency shift channel and the size of the rings changed depending on the lift height of the cantilever above the sample.

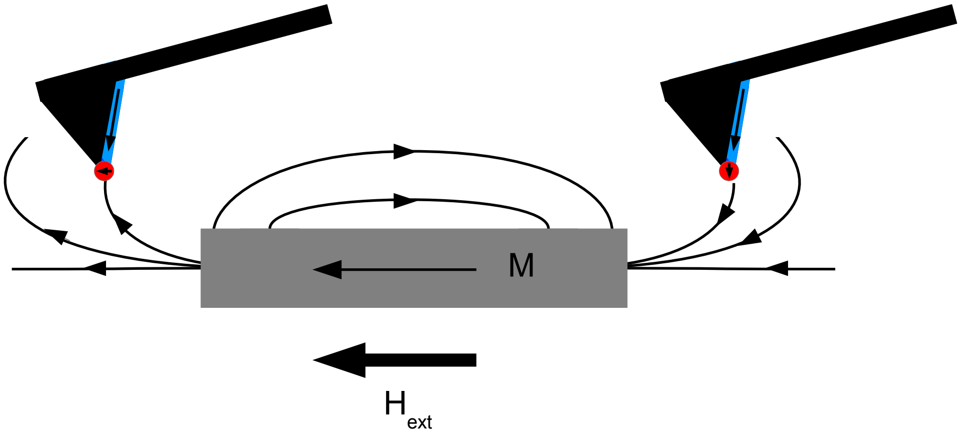

Figure 4.2: A schematic drawing of a one micrometer diameter permalloy dot in an 60 mT applied field. Blue represents the NiCo magnetic coating magnetized in the tip direction. Red represents the magnetically soft region on the tip that is suggested to be the cause of the rings in the frequency shift and dissipations from figure 4.1.

The ring artifacts shown in figure 4.1 were independent of the specific dot scanned and were always observed on the same side of the dot. We therefore propose that the artifact was caused by the influence of the stray field from the dot on the MFM tip [126]. Dissipation in FM-AFM (and therefore frequency shift mode MFM) is the result of a phase delayed force on the cantilever. It is probable that this phase delayed force was caused by a magnetization rotation of a small region on the MFM cantilever between two different magnetization states. We suggest that there was a small domain of magnetic material on the tip that changed magnetization direction when the stray field from the permalloy dot added to the stray field from the magnetized cantilever, as seen in the right cantilever of figure 4.2.

When the MFM cantilever was far from the artifact inducing end of the permalloy dot, the external applied magnetic field aligned the magnetization of the magnetically soft tip region with the applied field. The overall change in tip magnetization was not significant, as the contrast in the MFM (frequency shift) signal did not change, within experimental error, inside the dissipation rings. This suggests that the volume of the magnetically soft region on the tip was small compared to the magnetically hard tip region. As the MFM tip oscillated up and down across the boundary where this change was favorable, the magnetically soft tip region changed between the two states at the same frequency as the cantilever oscillation. Due to the coercivity of the magnetic volume, this change did not happen completely in-phase with the cantilever oscillation and therefore there was a phase-delayed force on the cantilever. This phase-delayed force was seen in the dissipation channel, as shown in figure 4.1. There was also a component that was in-phase with the cantilever oscillation, hence there was also contrast in the frequency shift channel, as shown in figure 4.1. The ratio of in-phase to out of phase components will depend on the coercivity of the reversing volume.

4.1.2 Simulation of permalloy dot magnetization and stray magnetic field

To verify the magnetically soft tip region hypothesis, a 20 nm thick, 1 μm diameter permalloy dot was simulated using OOMMF. The simulated stray field

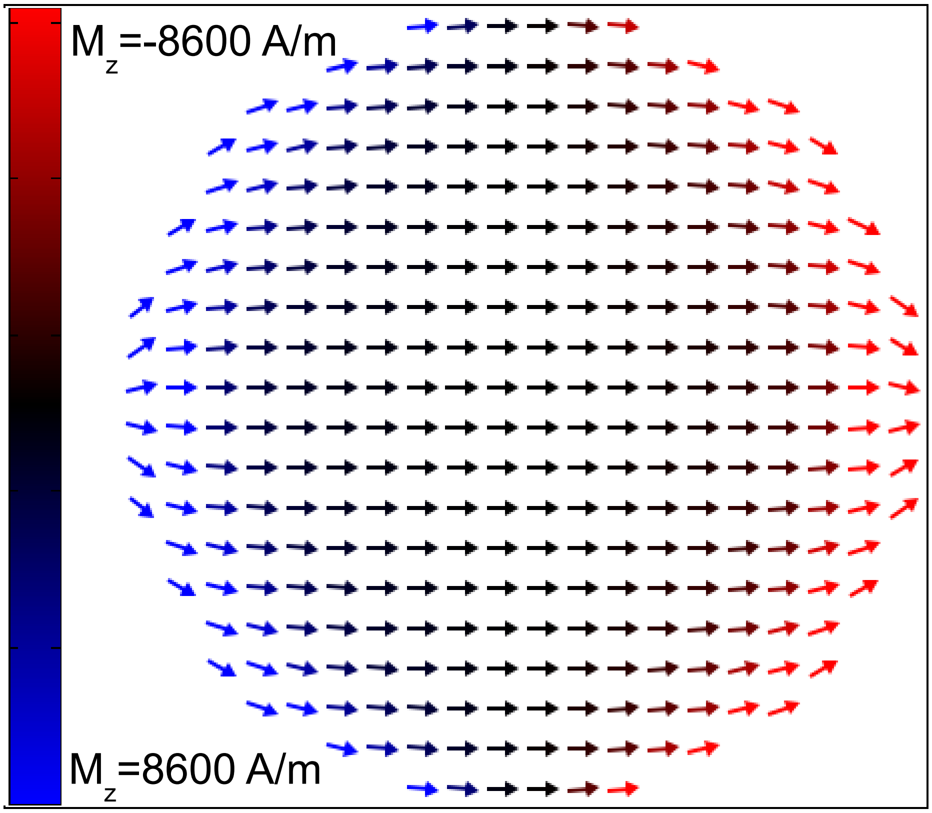

Figure 4.3: OOMMF simulation of the magnetization configuration of a 1 μm diameter 20 nm thick permalloy structure in a 60 mT magnetic field. The maximum vector length corresponds to the saturation magnetization of permalloy (860 kA/m). The colour represents the magnitude of the magnetization pointing out of the plane.

of the permalloy dot was compared to the dissipation rings measured using MFM to determine if a surface of stray magnetic field matches the surface made by the dissipation rings.

The material parameters used in the simulation were: saturation magnetization 860 kA/m, exchange stiffness 13×10^{-12} J/m and magnetocrystalline anisotropy 0 J/m^3 and a cubic cell with a side length of 5 nm. The simulation volume was large enough so that the stray field from the magnet could be calculated above the dot.

Figure 4.3 shows the magnetization configuration of the permalloy dot in a 60 mT applied field. The z component of the stray field 250 nm above the nanostructure of 14 ± 0.5 mT was selected to match the size of the ring shown experimentally in figure 4.1a. This value of the stray field was also used at the other lift heights shown in the left column of figure 4.1, and shows fairly good agreement with size and shape of the rings shown in the experimental data.

Figure 4.4 shows a 3D image of the surface with a z component of the stray field equal to 14 ± 0.5 mT in blue. Red represents the permalloy dot location, yellow represents the experimental data, and green represents the simulated data at the same heights as the experimental data.

Note that the experimental values agree much more closely with the simulated values at higher lift heights. This is most likely due to the stray field from the tip influencing the magnetization of the permalloy dot at lower lift heights, causing the magnetization configuration in the permalloy dot to differ from the simulated configuration. Such a change in magnetization configuration would result in a different location of the magnetic field at which the soft tip region will flip.

Although it is possible that the tip region changing magnetization configuration under the stray field from the permalloy dot was made of CoNi (the magnetic coating material on SC-35-M cantilevers), it is more likely that a small volume of permalloy was attached to the tip. The CoNi film coercivity is approximately 100 mT, which is too high to easily change the orientation. Additionally, the region of CoNi at the tip would have to be spatially isolated from the remainder of the CoNi film such that it was not exchange coupled to the rest of the CoNi film. It is more likely that the tip picked up a small piece of permalloy during the approach

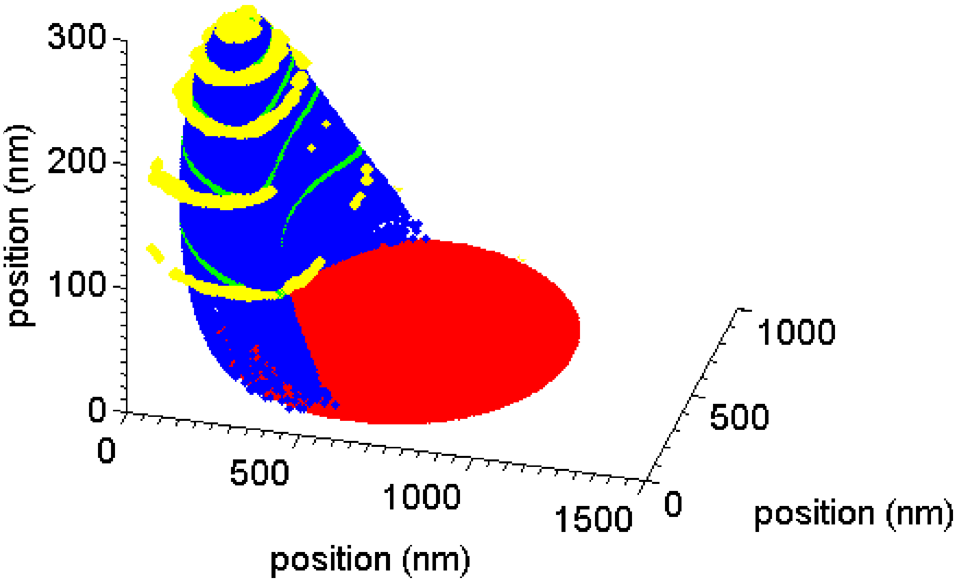

Figure 4.4: 3D image of the surface of constant z component of the stray field for a 1 μm diameter, 20 nm thick permalloy structure (red) in a 60 mT magnetic field. Blue represents the simulated z component of the stray field that is equal to -14 ± 0.5 mT. Yellow represents the experimental dissipation rings from figure 4.1. Green represents the simulated data at the lift height of the experimental data.

or during topography scanning.

4.1.3 Tip induced ring artifacts in MFM summary

An MFM imaging artifact that might lead to misinterpretation of MFM images was demonstrated. The ring artifact was attributed to a magnetically soft region on the MFM tip that changed magnetization configuration when influenced by the stray magnetic field of a 1 μm diameter, 20 nm thick permalloy dot. The artifact was observed in both frequency shift and dissipation signals with relative weights depending on the coercivity of the reversing region. The stray magnetic field of the dot was simulated and compared to the artifact which showed a similar shape. This artifact might be exploited to allow for 3D mapping of magnetic fields, with specialized design of MFM tip magnetization.

4.2 Variable field magnetic force microscopy

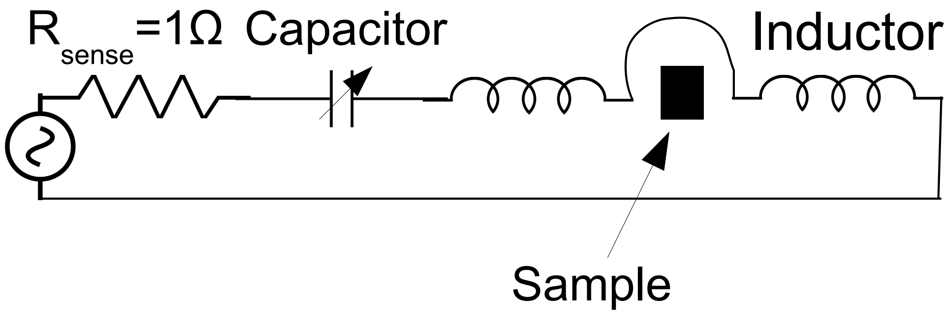

Figure 4.5: Schematic drawing of the RLC circuit used to apply an AC magnetic field to the sample. The poles of the inductors (solenoids) are placed on either side of the sample so the magnetic field from each solenoid is applied in the same direction. A variable capacitor sets the resonance of the circuit and the sensing resistor allows for the measurement of the current.

A problem with using MFM to measure the coercivity of a nanomagnet array is that it is difficult to collect enough robust, reliable data for statistical analysis of the SFD. This is because the experiment is time limited by non-idealities such as drift and creep (adjusting the position of the piezo to change the magnetic field). Half a hysteresis loop with 0.1 mT steps between 0 and 1.5 mT (required for the array discussed in chapter 3) consists of 16 images. Each images takes approximately 40 minutes (15 minutes to wait for creep to minimize, 20 min imaging and 5 min for changing the magnetic field), for a total of 11 hours to acquire half of a hysteresis loop. To accurately measure the distribution of the switching field of an individual nanostructure, smaller magnetic field steps and a significant number of hysteresis loops would be required.

A new MFM technique is developed here that involves applying an AC magnetic field to the sample that is large enough to reverse the magnetization of the sample, but still small enough that it is less than the coercivity of the tip (the coercivity of the SC-35-M MFM tips is greater than 79 kA/m [125]). The frequency of this applied magnetic field is locked to the frequency of the cantilever oscillation with a phase shift, allowing for the detection of nanomagnet switching induced dissipation in the MFM signal.

Similar to the tip induced ring artifacts in MFM, the ratio between frequency shift and dissipation will depend on the coercivity of the reversing volume (this time the nanomagnet). This technique has the potential to measure the switching field more than a thousand times a second, allowing for a measurement of the switching field distribution of an individual nanomagnet as well as the switching field relative to other nanomagnets in an array.

4.2.1 Producing an AC magnetic field

Typical MFM cantilever resonant frequencies are approximately 59-97 kHz [125]. To apply a magnetic field at these frequencies, a resonant RLC circuit was built (as shown in figure 4.5), where the electromagnet is the inductor and the capacitors serve to tune the RLC resonance to match the resonance of the cantilever.

The magnetic field, B, inside a solenoid is given by,

$$B = \mu n I, \tag{4.1}$$

where μ is the permeability of the core material, n is the wire turn density, and I is the current that passes through the wire.

Because these measurements take place in vacuum, the power dissipated in the solenoid (the only component of the RLC circuit that is inside the vacuum system) must be reduced to a level where the heat generated can be dissipated. Minimizing the power dissipation in the solenoid while maintaining a high field poses a significant design problem. The power dissipated in a wire is given by $P = I^2R$. Power can be minimized by reducing the resistance of the wire at the desired frequency or the current can be minimized. Minimizing the current conflicts with maximizing the field produced by the solenoid. Therefore, the resistance will be minimized.

The AC resistance in wires is caused by two effects at this frequency: the proximity effect [127] and the skin effect [127–129], as shown in figure 4.6a and b respectively. Both involve a reduction in the cross sectional area of the current carrying portion of the wire, which increases its resistance. The proximity effect is the result of induced eddy currents from neighbouring wires causing a reduction in current on one side of the wire and an enhancement of current on the other side of the wire. This reduces the cross sectional area of the current carrying portion of the wire, which increases its resistance. Similarly, the skin effect causes a reduction in the area of the current carrying portion of the wire, which is the result of eddy currents caused by changes of the wire's own current, thereby increasing its resistance.

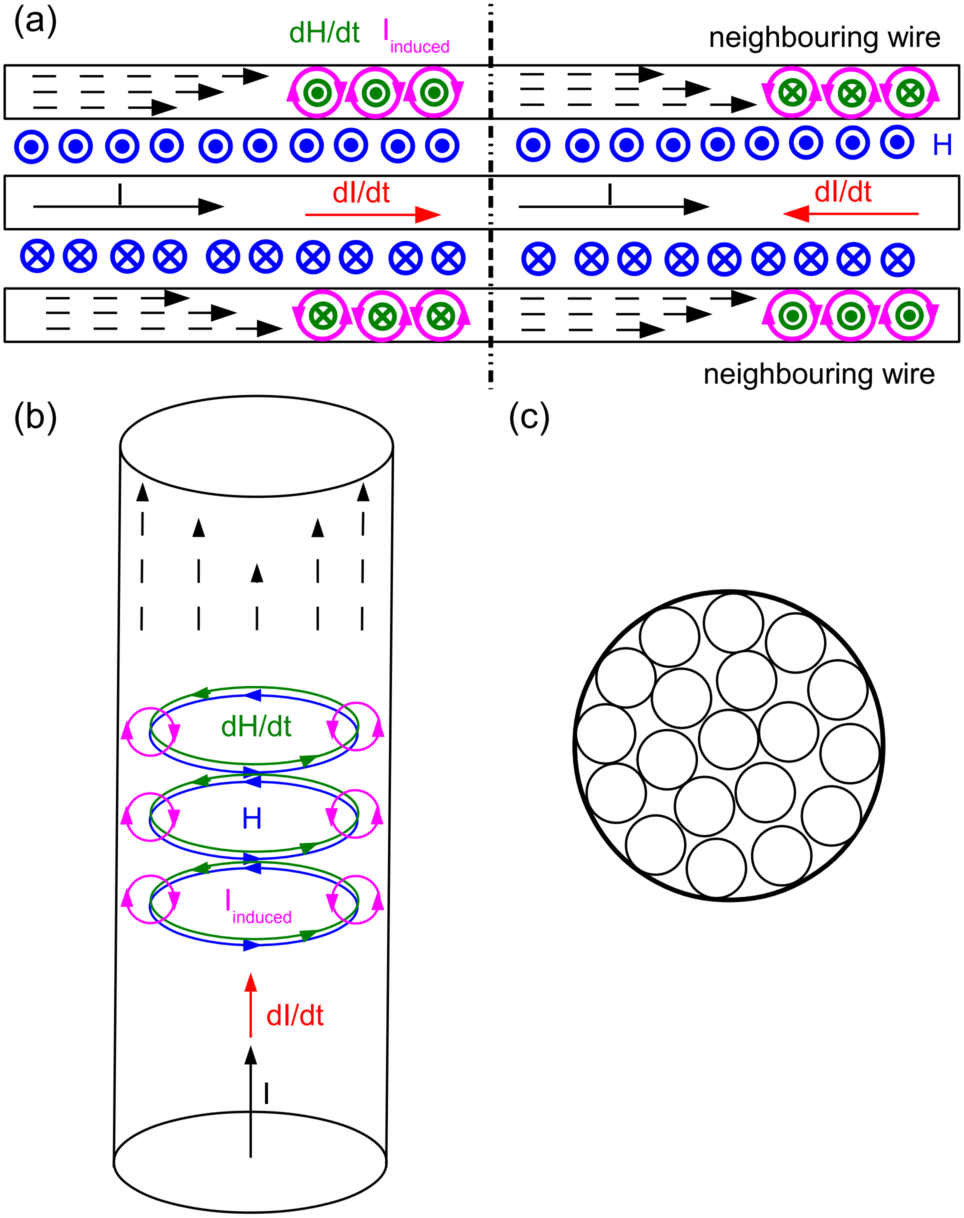

Figure 4.6: (a) Proximity effect of neighbouring solenoid wires on wire current. Black vectors represent current being carried in the wire. Red vectors represent the direction of the derivative of current with respect to time. Blue represents the direction of the magnetic field caused by the current in the wires. Green represents the change in field as a result of the change in current. Pink represents the induced current that is a result of Lenz's law. (b) Similarly, the skin effect causes a reduction in the area of the current carrying portion of the wire, increasing its resistance. (c) Cross sectional schematic of Litz wire in which a series of small wires, that are not electrically contacted to each other, are wound in a bundle.

To mitigate the increase in resistance, Litz wire [130] (40 strands of served 44 AWG) can be used as shown in figure 4.6. Litz wire is a bundle of insulated wires that is wound such that the individual wires exchange radial positions along the length of the bundle so that each wire is in each position in the bundle along the length. This distributes the increased resistance caused by the proximity effect equally among the wires, minimizing the effect. The small insulated wire is selected so that its diameter is less than the skin depth at the desired frequency, which reduces the skin effect. The proximity effect also limits the solenoid (inductor) to one layer of Litz wire.

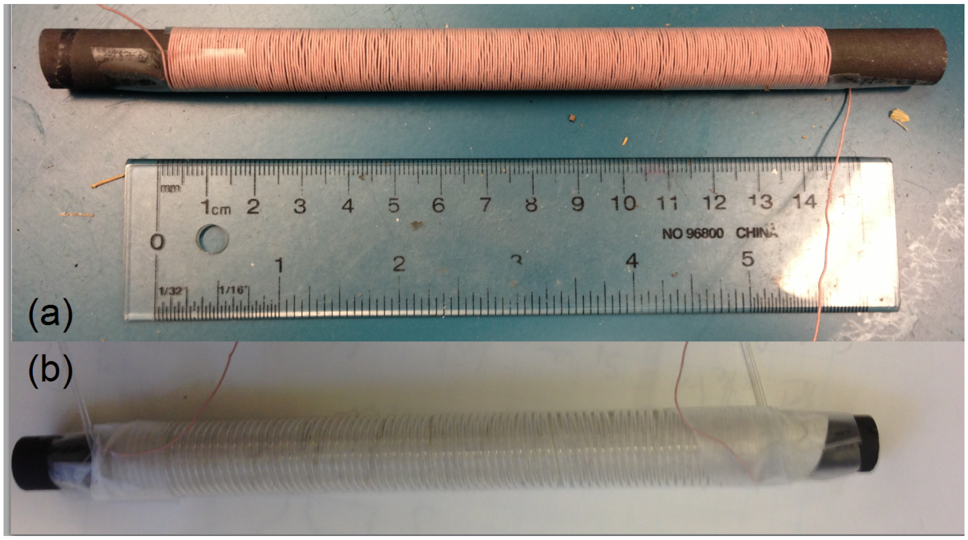

Figure 4.7: (a) Ferrite core wound with Litz wire (b) Litz wire covered with thermally conductive, electrically insulating tape and is then wound with Teflon tubes used for water cooling.

A ferrite rod (R-050750-33, made of iron oxide and MnZn, permeability of $800\mu_0$, with operating frequencies between 0.01 and 400 MHz, from cwsbytemark.com) was chosen as the core material for the inductor because it has a high magnetic permeability at frequencies in the range of interest (typical cantilever resonances between 58 - 97 kHz [125]). This high magnetic permeability results in an increased magnetic field, as shown in equation 4.1.

The actual permeability of a rod is less than the bulk value due to the demagnetizing field [131]. The demagnetizing field causes the magnetization near the ends of the rod not to be aligned with the rod axis. By increasing the length to diameter ratio, the demagnetizing factor has less of an influence on the total permeability. Rod length was limited by the space available in the vacuum chamber. Therefore, ferrite rods 19.05 cm in length and 12.7 mm in diameter (aspect ratio of 15) were used. The magnetization that is not aligned with the rod axis results in a stray field that leaks from the side of the rod.

The alternating stray field can induce eddy currents in the current carrying wires that increases their resistance. For this reason, the core is not wound completely to the end (figure 4.7a). The AC resistance at 65 kHz of the RLC circuit was approximately 15 Ω when the two cores (shown in figure 4.7a) were separated by 9.5 mm. This resulted in approximately 100 W being dissipated in the RLC circuit with a Q factor of approximately 30. This is a large improvement when compared to 26 gauge copper wire two layers thick that had an AC resistance of 800 Ω at 50 kHz. The power dissipated in the non Litz wire RLC circuit would be approximately 5000 W for a similar current.

Heat generated by the solenoids is removed using a water cooling system. Water is pumped into the vacuum system though feed-throughs in Teflon tubes. These tubes are thermally contacted to the electromagnets though electrically insulating, thermally conductive tape as shown in figure 4.7b.

An additional design constraint is that the AC magnetic field will induced eddy currents in any metal pieces within the magnetic field. These eddy currents cause heating, which results in drift in the microscope components. To measure the influence of eddy currents on microscope drift the aluminum microscope head was placed over top of the sample with the fiber optic interferometer approached to the back of a cantilever. The AC magnetic field was then turned on and the interferometer signal drifted at a rate of 5 nm per second.

To reduce microscope drift, a new microscope head and sample holder were built using insulating Delrin to minimize the use of metal. This reduced the drift to 1.6 nm per second, the remainder of which is presumably a result of the inductors heating up and radiatively heating the microscope head. When the system is turned on and allowed to thermally stabilize for an hour, the drift reduces to a controllable level of approximately 0.5 nm per second. At this rate the fiber position must be adjusted infrequently enough (approximately every 4-5 minutes) that images can be acquired.

4.2.2 MFM dissipation in an AC magnetic field

Dissipation in MFM cantilevers has been studied previously [132–134] and is the result of non-conservative interactions between the stray magnetic field of the tip and the sample. MFM has also been previously performed in a variable magnetic field to measure AC magnetic field sources [135–138]. However, we present a new technique in which an external AC magnetic field is used to reverse the magnetization of a sample.

As the applied field reverses the magnetization of a nanomagnet sample, the stray field of the nanomagnet will also reverse direction. Due to hysteresis of the nanomagnet, there will be a phase delay on the reversal of the stray magnetic field. The resulting phase delayed force is detectable in the dissipation channel of the nc-AFM signal, as will be described in detail below [38]. Nanomagnets with

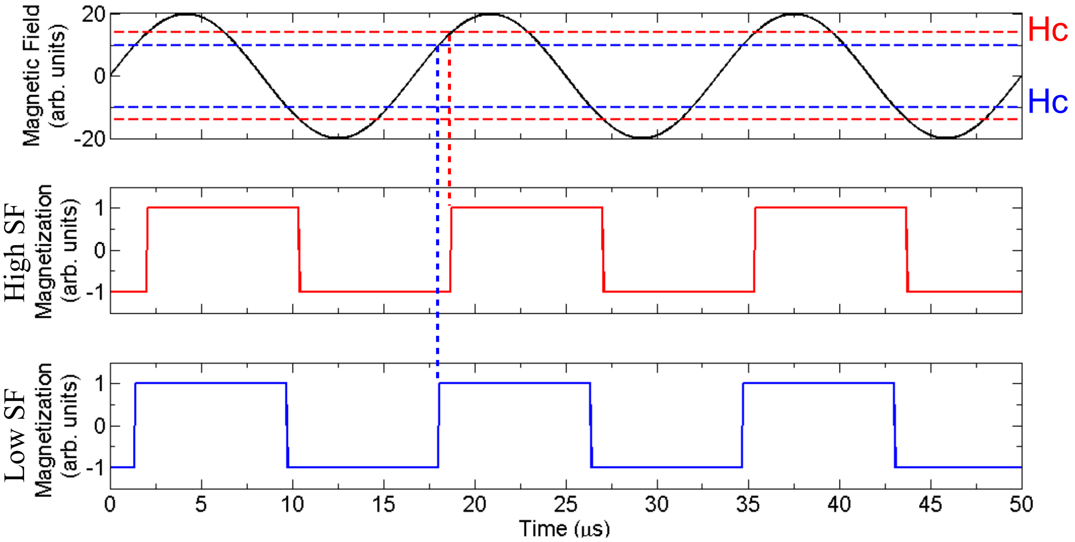

Figure 4.8: The applied field (black) switches the magnetization of the nanostructures depending on their switching field. The phase shift of the magnetization compared to the applied field is higher for the nanostructure with a larger switching field (red) when compared to the lower switching field (blue). Because the applied field is locked to the cantilever oscillation, and the force on the cantilever depends on the magnetization direction. It will have in-phase and out of phase components that depend on the nanomagnet coercivity. The magnetization is assumed to reverse in a step at the coercive field.

a larger switching field should produce a larger signal in the dissipation channel (the phase between the cantilever oscillation and magnetization reversal is higher), as shown in figure 4.8. It is also important to note that the period of the applied field is much larger than magnetization reversal times (on the order of 10 ns) [18], allowing sample nanomagnets to switch completely during each magnetic field oscillation.

The equation of motion of a damped harmonic oscillator that is subject to an external driving force (F_{exc}) and a force due to the stray field of a reversing nanomagnet (F_{mag}) is given by,

$$m\ddot{z} + \gamma_0 \dot{z} + k(z - z_0) = F_{exc}(t) + F_{mag}(t), \tag{4.2}$$

where z is the position of the cantilever, γ_0 is the intrinsic damping of the cantilever, k is the spring constant and m is the mass of the cantilever. Assuming that the magnetization of the cantilever tip is uniform in the z direction and the oscillation amplitude is small compared to the change in the gradient of the stray field, the force from the stray field on the cantilever can be approximated by a monopole [139] given by,

$$F_{mag}(t) = q_M \frac{dH}{dz} z_w e^{-i\omega t} (\cos\phi + i \sin\phi), \tag{4.3}$$

where q_M is the magnetic charge of the cantilever, ω is the oscillation frequency of the cantilever and the field and z_w is the cantilever oscillation amplitude. ϕ is the relative phase between the applied field and the magnetization direction (as shown in figure 4.8) and is given by,

$$\phi = \arctan\left(\frac{H_c}{H_{max}}\right), \tag{4.4}$$

where H_{max} is the maximum amplitude of the applied magnetic field. By assuming a solution of the form,

$$z(t) = z_0 + z_w exp(-i\omega t), \tag{4.5}$$

and rearranging equation 4.2, one arrives at the following expression,

$$-\omega^2 + \frac{1}{m}\left(k - q_M \frac{dH}{dz}\cos\phi\right) - \frac{i\omega}{m}\left(\gamma_0 + \frac{q_M}{\omega}\frac{dH}{dz}\sin\phi\right) = \frac{1}{m}\left(G_{real} + iG_{imag}\right), \tag{4.6}$$

and therefore the change in spring constant (Δk), which is related to frequency shift, can be related to to the coercivity of the nanomagnet by,

$$\Delta k = q_M \frac{dH}{dz} \cos\phi. \tag{4.7}$$

Similarly, the change in dissipation ($\Delta\gamma$), can be related to the coercivity of the nanomagnet by,

$$\Delta\gamma = \frac{q_M}{\omega} \frac{dH}{dz} \sin\phi. \tag{4.8}$$

Because many interactions can lead to changes in spring constant (Δk), we use changes in dissipation ($\Delta\gamma$) to detect changes in the nanomagnet coercivity.

4.2.3 Experimental configuration

The goal of the variable field MFM is to measure the relative coercivity of an array of nanomagnets. To determine the sensitivity of the technique, the minimum detectable change in coercivity was estimated for different cantilever lift heights.

The minimum detectable change in coercivity will result in a change in dissipation that is greater than the thermal noise of the cantilever. The minimum thermal dissipation noise ($\Delta\gamma_{min}$) of the cantilever for our setup is calculated to be 15 pNs/m (bandwidth 181 Hz, oscillation amplitude 20nm) [31]. The minimum detectable change in coercivity is obtained by differentiating equation 4.8 with respect to coercivity and solving for the change in coercivity while setting the change in dissipation equal to the minimum thermal dissipation noise as follows,

$$\Delta H_{c_{min}} = \frac{\Delta\gamma_{min}\omega H_{max}}{q\cos\left(H_c/H_{max}\right)} \frac{1}{dH/dz}. \tag{4.9}$$

Table 4.1: Theoretical calculations for the sensitivity of variable field MFM. Sensitivity calculated at half of the maximum field to ensure saturation of the nanostructures.

Lift height	Minimum detectable change in coercivity (A/m)	Minimum detectable change in coercivity $\times\mu_0$ (mT)
180 nm	14000	18
80 nm	2000	2.5
30 nm	340	0.42
10 nm	50	0.063

The simulation of the stray magnetic field of a permalloy nanomagnet (shown in figure 1.6), was used to estimate dH/dz for different cantilever lift heights. Assuming that the coercivity is 30 mT and the maximum applied magnetic field is 60 mT, the minimum detectable change in coercivity is estimated and shown in table 4.1.

For the input parameters used, a small lift height of approximately 30 nm is necessary to detect a 0.4 mT change in coercivity (the coercivity of the array discussed in chapter 3 varied by approximately 1 mT). Depending on the sample, it might be necessary to cool the system to cryogenic temperatures or decrease the detection bandwidth which improves nc-AFM sensitivity as mentioned in section 1.2. An improvement in sensitivity will result in a decrease to the minimum detectable change in coercivity. This allows for a higher cantilever lift height and therefore a smaller influence of the MFM tip on the sample.

A problem arises when applying an AC magnetic field at the cantilever resonance frequency. Commercially available MFM cantilevers have a magnetic coating on the cantilever beam as well as on the tip. This causes the cantilever to oscillate when the AC magnetic field is applied. An attempt to dampen the unwanted oscillations was made using a PLL, but was unsuccessful. This is because higher cantilever oscillation modes were also excited, causing the cantilever to oscillate uncontrollably at large amplitudes. A possible solution is to design a cantilever such that only the tip is magnetically coated and its magnetization points as close to perpendicular to the applied field as possible (normal to the sample). This would drastically reduce the amplitude of oscillation at the cantilever resonance frequency in the AC magnetic field.

We therefore developed an alternative method where the AC magnetic field is applied at a much lower frequency (1 kHz), far from any mechanical resonance of the cantilever. A lock-in amplifier is used to detect the cantilever's frequency shift at the applied field frequency as well as the phase of this interaction relative to the applied field. The MFM cantilever can then be either raster scanned at a constant lift height to image or held to image above a specific structure to record a dissipation spectrum as a function of the amplitude of the oscillating applied magnetic field.

Figure 4.9 shows the apparatus for variable field MFM. Here the capacitance of the RLC circuit is tuned so that it has a resonance at approximately 1 kHz. Lock-in amplifier number 1 is then replaced with a PLL with input frequency set to the resonance frequency of the RLC circuit and output amplitude either set to a constant value for scanning mode or modulated for spectroscopy mode, both of which are described below. The variable field MFM technique was tested with an array of permalloy nanostructures made using electron beam lithography and electron beam evaporation.

Scanning mode uses a field that is at constant amplitude (55 mT), which is larger than the coercivity of the nanomagnets of interest ($\sim$10 mT). The sample is scanned at a constant height and lock-in amplifier number 2 (from figure 4.9)

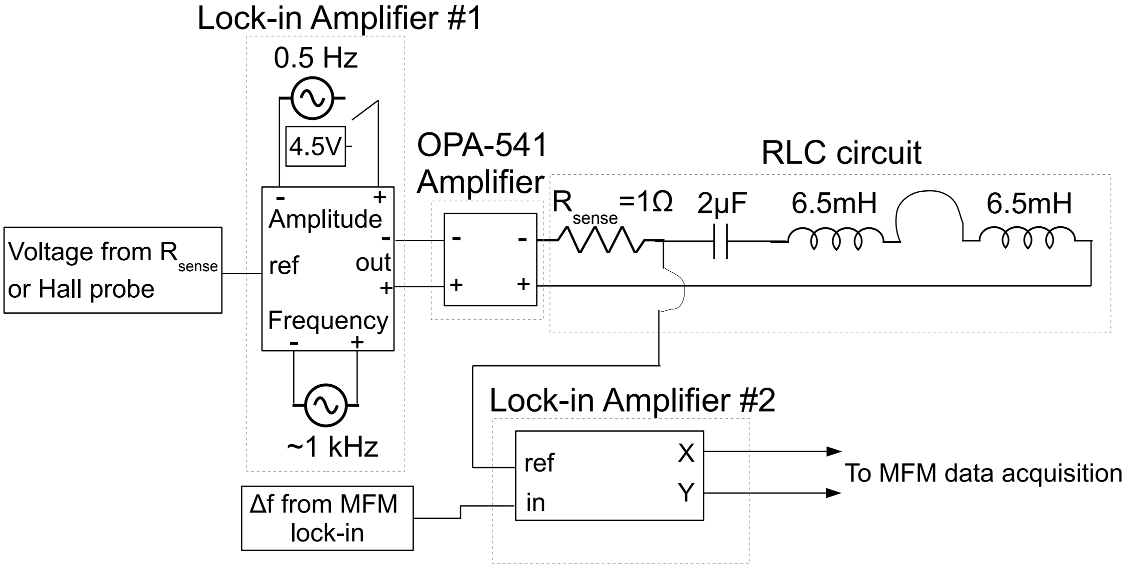

Figure 4.9: Schematic of VF-MFM. The RLC circuit consists of, Litz wound ferrite core electromagnets (inductors) used to apply the magnetic field, and a series of capacitors. Lock-in amplifier number 1 is used to find the resonance frequency of the RLC circuit using either the magnetic field or the current as a reference. Subsequently lock-in amplifier number 1 outputs a 4.5 V, 1 kHz sine wave for scanning mode or a 1 kHz, 4.5 V sine wave that is modulated at 0.5 Hz for spectroscopy mode. The output of the lock-in amplifier is amplified to ± 60 V using an OPA-541 chip. Lock-in amplifier number 2 is used to measure amplitude and phase of the resonance frequency of the MFM cantilever frequency at the magnetic field frequency. The magnetic field frequency is measured using a hall probe or by measuring the current that passes through the electromagnets.

is used to measure the amplitude and phase of the frequency shift relative to the magnetic field (or drive current). The phase between the applied magnetic field and the frequency shift will depend on the coercivity of the magnets being scanned, provided the applied magnetic field is larger than the coercivity.

Preliminary scanning mode data of electron beam evaporated permalloy nanostructures defined by electron beam lithography is shown in figure 4.10. In general, the expected contrast is visible in both amplitude and phase channels. The frequency shift at the applied magnetic field frequency (figure 4.10a) is higher over the ends of the nanostructures, as expected. This suggests that the nanostruc-

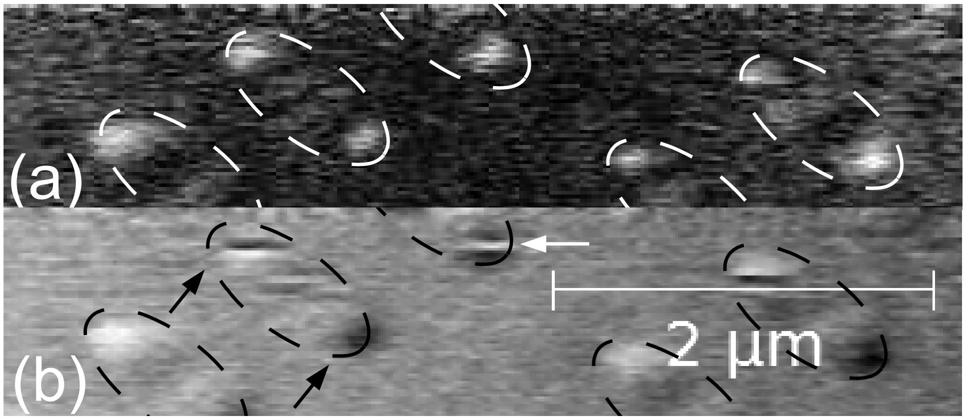

Figure 4.10: Variable field magnetic force microscopy images of 20 nm of electron beam evaporated permalloy with nanostructures defined by electron beam lithography. (a) is the amplitude of the frequency shift signal at the frequency of the applied field. (b) is the phase between the frequency shift signal and the applied field. Black arrows indicate ends of a nanostructure and white arrow represents a region of contrast inversion.

tures are indeed reversing magnetization direction and the stray field from the nanostructure is influencing the cantilever oscillation dynamics.

In the phase image (figure 4.10b), there appears to be opposite contrast on each end of the nanostructure. This opposite contrast is as expected because the interaction between the north pole of the nanomagnet and the magnetized cantilever is 180° out of phase relative to the cantilever oscillation (compared to the the south pole), resulting in a change in sign of the phase shift measured.

Unfortunately, there was a significant amount of thermal drift during these measurements, caused by the electromagnets heating up as well as eddy current heating in the remaining metal microscope components (such as foil that shields piezo voltage from the tip-sample junction). This made it very difficult to make repeated measurements over a specific location so that the amplitude of the change in-phase could be compared to the DC switching field distribution (as measured in section 3.1). There are also what seem to be inversions in the phase contrast over a few of the nanostructures, as indicated by the white arrow shown in figure 4.10b. This has yet to be explained and further work is needed to understand the detailed mechanisms at play.

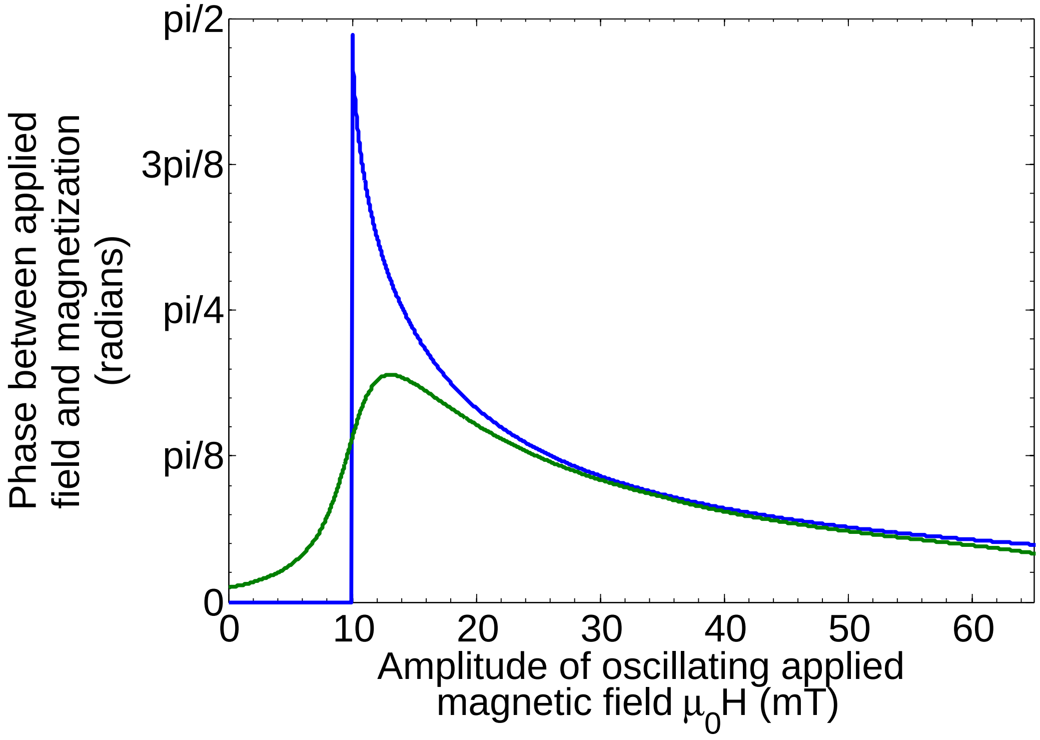

Figure 4.11: Blue: Simulated phase between applied field and magnetization direction. Green: Blue data convolved with a Lorentzian with width of 3 mT.

Spectroscopy mode involves modulating the amplitude of the applied magnetic field (between 0 and 65 mT) while the MFM tip is held at a fixed distance above one end of a nanostructure. The amplitude of the oscillating applied magnetic field is modulated at a frequency of 0.5 Hz and a lock-in amplifier is again used to measure the amplitude and phase of the frequency shift signal, at the frequency of the applied magnetic field. Because the nanomagnet switches magnetization direction only when the applied magnetic field exceeds the coercivity of the

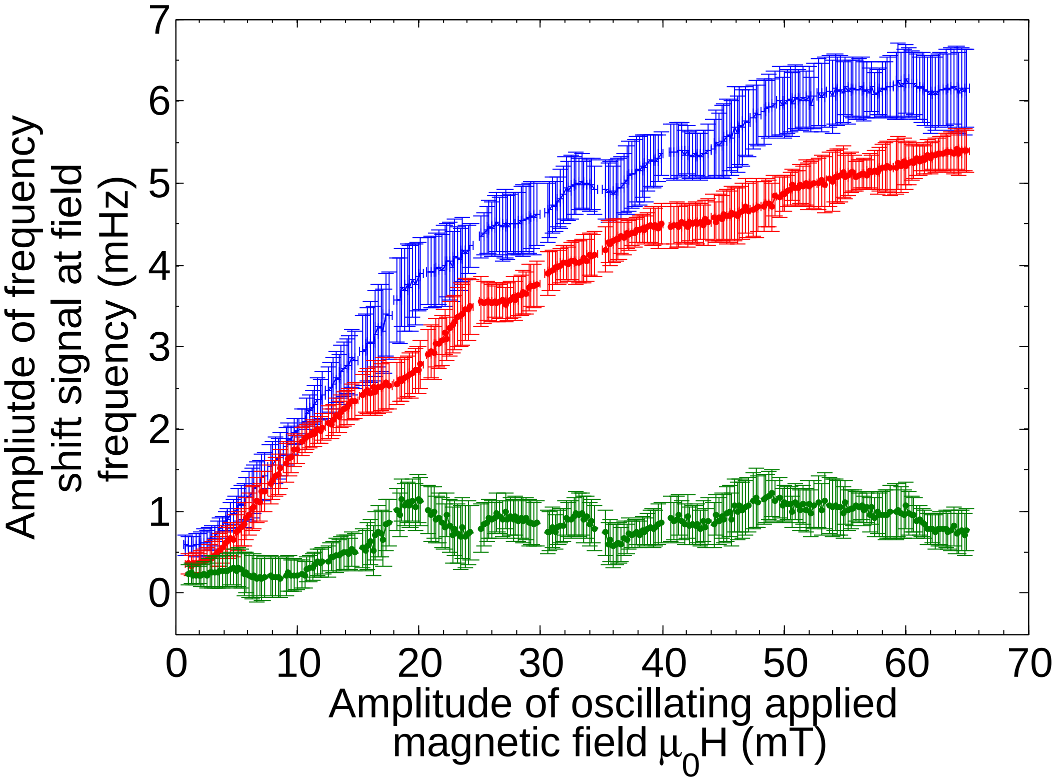

Figure 4.12: Amplitude of the frequency shift signal at the applied field frequency as a function of the amplitude of the applied field. Blue data taken 15 nm above the permalloy nanostructure and red data is taken 4 μm from the nanostructures. Green data is the blue data with the background (red data) subtracted.

nanomagnet, there should be a sharp increase in the phase when the amplitude of the applied field reaches the coercivity.

Figure 4.11 shows a plot of the idealized phase (blue) between applied field and the magnetization direction. Note that the largest phase difference occurs when the oscillation amplitude of the field is equal to the coercivity. As the applied magnetic field amplitude exceeds the nanomagnet coercivity, magnetization reversal of the nanomagnet occurs at a phase that is less then 90° out of phase with the applied field and thus the phase decreases.

Spectroscopy mode data was acquired for many periods of the modulating

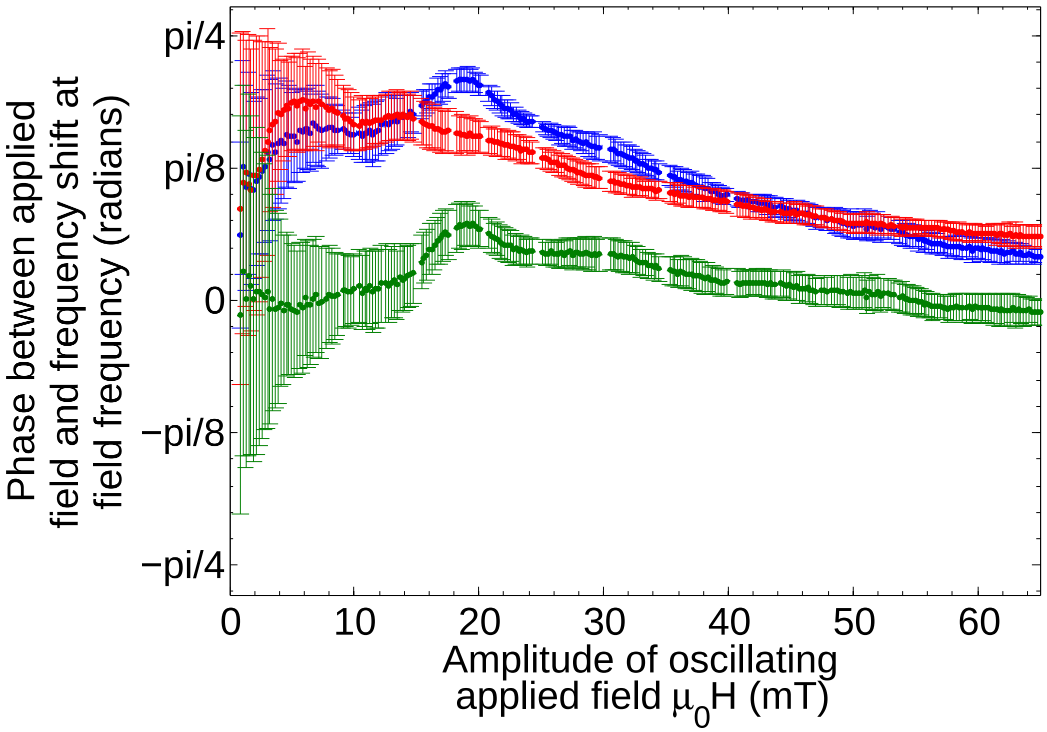

Figure 4.13: Phase between frequency shift signal and the applied field frequency as a function of the amplitude of the applied field. Blue data taken 15 nm above the permalloy nanostructure and red data is taken 4 μm from the nanostructures and is acquired at the same time as the data shown in figure 4.12. The green data is the blue data with the red background subtracted.

field and amplitude and phase were averaged to produce figures 4.12 and 4.13 respectively. Error bars represent the standard deviation of the averaged curves. The background signal, which is a result of the MFM tip interacting with the AC field, is subtracted from the data recorded with the tip held 35 nm above one end of a permalloy nanostructure, as shown in green in figure 4.13.

Spectroscopy data shows a peak in the phase at an applied magnetic field amplitude of approximately 19 mT. The phase peak does not go to 90 degrees, nor is it as sharp as the simulated curve shown in figure 4.11, but it does follow approximately the same shape as the Lorentzian convolved green simulated curve, suggesting that the nanomagnets indeed begin switching magnetization at magnetic field amplitudes of approximately 19 mT. The background subtracted amplitude signal increases at approximately the same magnetic field (19 mT) and is constant within error for higher applied magnetic fields. This is expected as higher fields should not increase the amplitude of the stray field (and thus the frequency shift) of the nanostructure. The magnetization (and stray field) reversal should continue for all amplitudes of the oscillating applied magnetic field that are larger than the nanomagnet coercivity.

A limitation of the spectroscopy technique is that the nanomagnets are not generally saturated in between each reversal so the magnetization state is not switched between well defined magnetization states. For this reason, it is expected that the scanning mode technique may be more useful for comparing the switching field distribution of arrays of nanomagnets.

4.2.4 Variable field MFM Summary

A technique to measure the relative switching fields of an array of nanomagnets in a single scan was investigated. Preliminary data shows that the technique is sensitive enough to detect the reversal of a nanomagnet, but further study is required so that sensitive measurements can be made to compare the switching field of an array of nanomagnets.

5

Conclusions and outlook

5.1 Conclusions

The overarching goal of this work was to gain insight into the most important factors influencing the switching field distribution in permalloy nanomagnets.

The unexpected behaviour of nanostructures fabricated using electron beam evaporation though FIB milled nanostencils led to an in depth study of factors influencing their growth, structure and functional characteristics. Implanted gallium ions were identified as the culprit of these unexpected behaviours, with potential far reaching implications for FIB milled stencil users everywhere.

Once a permalloy nanostructure array with a measurable stray magnetic field was finally fabricated, the SFD was measured and analyzed for shape and roughness correlation using experimental data and simulations. A clear trend was not observed, most likely due to the low sample size, but preliminary data suggests that before focusing efforts on reducing edge roughness, the finite length shape anisotropy factor must be well controlled.

A ring artifact found in both frequency shift and dissipation images during MFM scans was attributed to a soft magnetic region on the MFM tip. The relative signal contrast in dissipation and frequency shift channels is suspected to be caused by the coercivity of the soft magnetic region. The position of the rings were compared to an OOMMF simulation of the z component of the stray field from a 1 μm permalloy dot and showed good agreement. This phenomenon might have potential applications in 3D mapping of the stray magnetic field of a nanomagnet.

A new technique was developed in which an AC magnetic field is applied to an array of permalloy nanomagnets. A MFM cantilever is scanned above the nanomagnet, and a lock-in amplifier is used to measure the phase between the cantilever resonant frequency shift and applied magnetic field. When the applied field oscillation amplitude exceeds the nanomagnet coercivity, the cantilever dynamics are influenced. The phase between frequency shift and applied magnetic field depends on the nanomagnet coercivity (switching field), which should allow for the measurement of the relative switching field of an entire array of nanomagnets in a single variable field MFM scan as well as measure the distribution of switching field of an individual nanomagnet. Preliminary results show that there is a measurable phase difference between the frequency shift and the applied magnetic field. This is an important step towards measuring the switching field distribution of arrays of nanomagnets.

5.2 Future horizons

5.2.1 Investigating the role of coupling on SFD

The creation of larger arrays of nanomagnets open up some interesting experimental possibilities for studying the coupling of neighbouring nanomagnets. A large sample, on the order of 100 μm $\times$ 100 μm, could be fabricated using an electron beam writer on a free standing SiN membrane. As in experiments presented previously, indexing with missing structures would allow the exact region of investigation to be identified within a 40 μm scan size. The spatially resolved switching field distribution could be measured either using standard MFM in a DC magnetic field or the newly developed variable field MFM technique. To confirm that the switching field and the switching field distribution is not being influenced by the magnetic cantilever, MOKE could be performed provided the array is sufficiently large. Because of the increased sample size, the measurement of interactions between nanomagnet elements using first order reversal curves (FORC) [140–143] would be possible. FORC consists of saturating the magnetization in a large magnetic field. The magnetic field is then reduced to a value H_a and the magnetization of the nanostructures are measured as a function of applied magnetic field (H_b) as the field is increased back to the saturating magnetic field. By looking at how $M(H_a, H_b)$ changes as a function of H_a and H_b, a measurement of the coupling of neighbouring nanomagnets can be made. Because FORC measures the amount of coupling between neighbouring nanomagnets, the influence of element separation (nanomagnet coupling) could be compared to other causes of SFD.

5.2.2 Artificially narrowing SFD with FIB

It would also be interesting to try and artificially narrow the switching field distribution of an array of nanomagnets using a focused ion beam so that defects could be corrected in MQCA or MRAM devices. It has been shown that by implanting gallium ions, the coercivity of permalloy can be increased [144]. After the switching field distribution is measured using MFM, nanomagnets with low coercivity could be implanted with gallium ions using a FIB and the edges of the nanomagnets with high coercivity might be smoothed, thereby narrowing the overall switching field distribution.

5.2.3 Investigation of MQCA

Magnetic quantum cellular automata (MQCA) is a novel computer architecture [7] where ferromagnets are used to transmit signals [7, 145] and perform logic operations [146] using less power than conventional electronics [9]. Electron beam lithography could be used to define chains of nanomagnets that are coupled though dipolar interaction, allowing the reliability of these chains to be tested. The same could be done for logic gates. FIB might be used to repair defects by implanting ions (increasing the coercivity) or to change the shape of problematic portions of the MQCA circuit by milling.

5.2.4 Variable field MFM development

Finally, further study into the variable field magnetic force microscopy technique is necessary. By designing MFM cantilevers without magnetic coating on the cantilever beam and a minimal amount of magnetically hard coating at the tip, the magnetic material induced oscillations of the cantilever will be drastically reduced. This could be performed using a FIB to mill away unwanted regions as discussed in section 2.1. It might then be possible to perform the variable field MFM experiment on resonance while looking at dissipation and frequency shift to measure the relative switching field. Next it is necessary to do a controlled experiment where the switching field of an array of nanomagnets is measured using standard MFM followed by variable field MFM so that the switching field measured using the two techniques can be compared. It would also be interesting to perform this technique at low temperatures, which should improve the minimum detectable change in coercivity shown in table 4.1, but would be very challenging to remove the heat generated by the electromagnets.

5.2.5 Further study of factors influencing SFD

The sensitivity of SFD to edge roughness and shape anisotropy could be investigated further by fabricating nanostructures with different sizes and shapes. By studying how edge roughness influences SFD for over a broader range of shapes and sizes than those presented here, it might be possible to develop nanostructures with a switching field that is less sensitive to changes in edge roughness.

In addition, factors such as temperature and the dependence of film morphology on substrate should be explored. Integration of nanomagnetic structures in real world electronics may require elevated operation temperatures and silicon substrate based fabrication.

Although the detailed origins of the SFD in permalloy nanomagnets are still not fully understood, progress has been made in our abilities to both fabricate and characterize permalloy nanomagnet arrays.

A

Apparatus

A new controller was installed using publicly available, Gnome X Scanning Microscopy (GXSM) [147, 148], software. This low cost controller allowed for up to 8 simultaneously acquired inputs.

A.1 DC magnetic field

A home built magnetic force microscope [46, 149] was updated so that in-plane magnetic fields could be applied in high vacuum conditions without heating the sample and microscope head. Heating of the sample and microscope head cause the fiber cantilever position to drift. The home built microscope head, fiber walker and permanent magnet assembly is shown in figure A.1. The left magnet assembly is shown in exploded view. A micromotor (Faulhaber 1224SR series motor and Faulhaber 12/4 planetary gear head, in purple) turns an anti-backlash worm gear (brown). This worm gear is attached to the NdFeB permanent magnets.

To vary the in-plane magnetic field at the sample position the NdFeB permanent magnets are rotated. The motors rotate the two magnets in opposite direction (one clockwise the other counter clockwise), allowing a continuous transition from pointing in the same direction (parallel to the soft iron cores shown in blue in figure A.1) for the maximum field direction, to being anti-parallel to each other

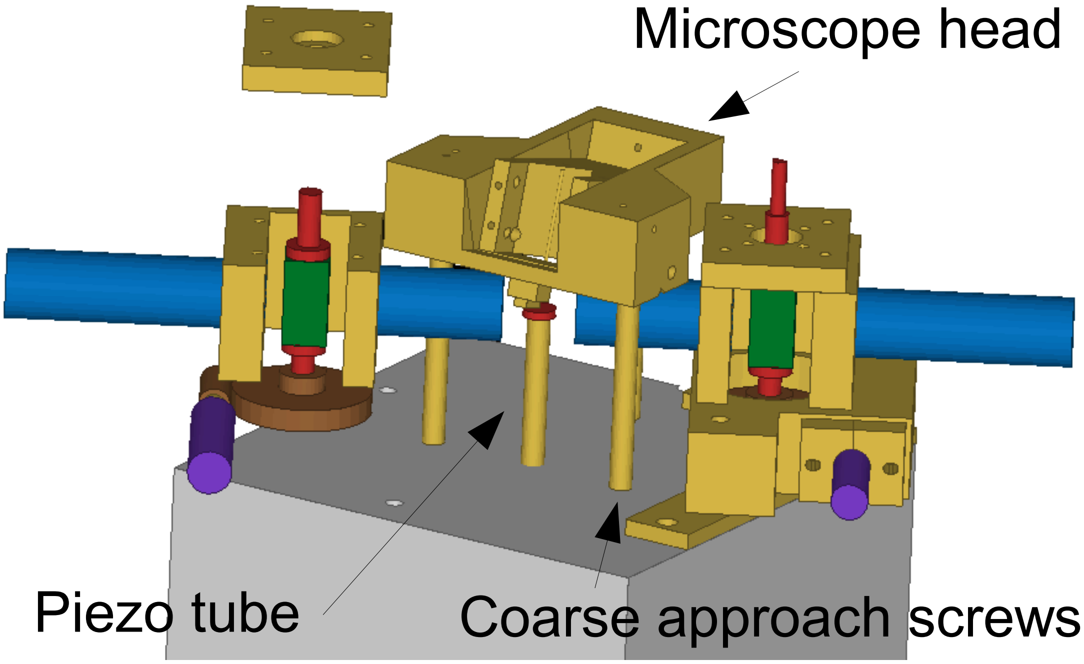

Figure A.1: Home built magnetic force microscopy apparatus used to apply a DC magnetic field. Blue is soft iron poles, green is NdFeB permanent magnet, Brown is worm gear assembly, purple are motors. Microscope head and fiber walker are shown in yellow in the center of the image. The red circle in the center of the image is the sample location which sits on top of a piezo tube. Parts of the left assembly have been removed so that all the components are visible.

for zero applied field, to pointing opposite directions (180°) for the maximum negative magnetic field.

The maximum magnetic field configuration is shown in figure A.2a. The left and right magnets in figure A.2a are rotated clockwise and counter-clockwise respectively to reduce the amplitude of the in-plane magnetic field until they are rotated by a total of 90° where 0 mT in-plane magnetic field is applied shown in figure A.2b. The design of the permanent magnet field assembly and the figure A.2 were made by Dr. Jan Sandtner and Dr. Hannes Bleuler from the Institute de microtechnique, École Polytechnique Federale de Lausanne.

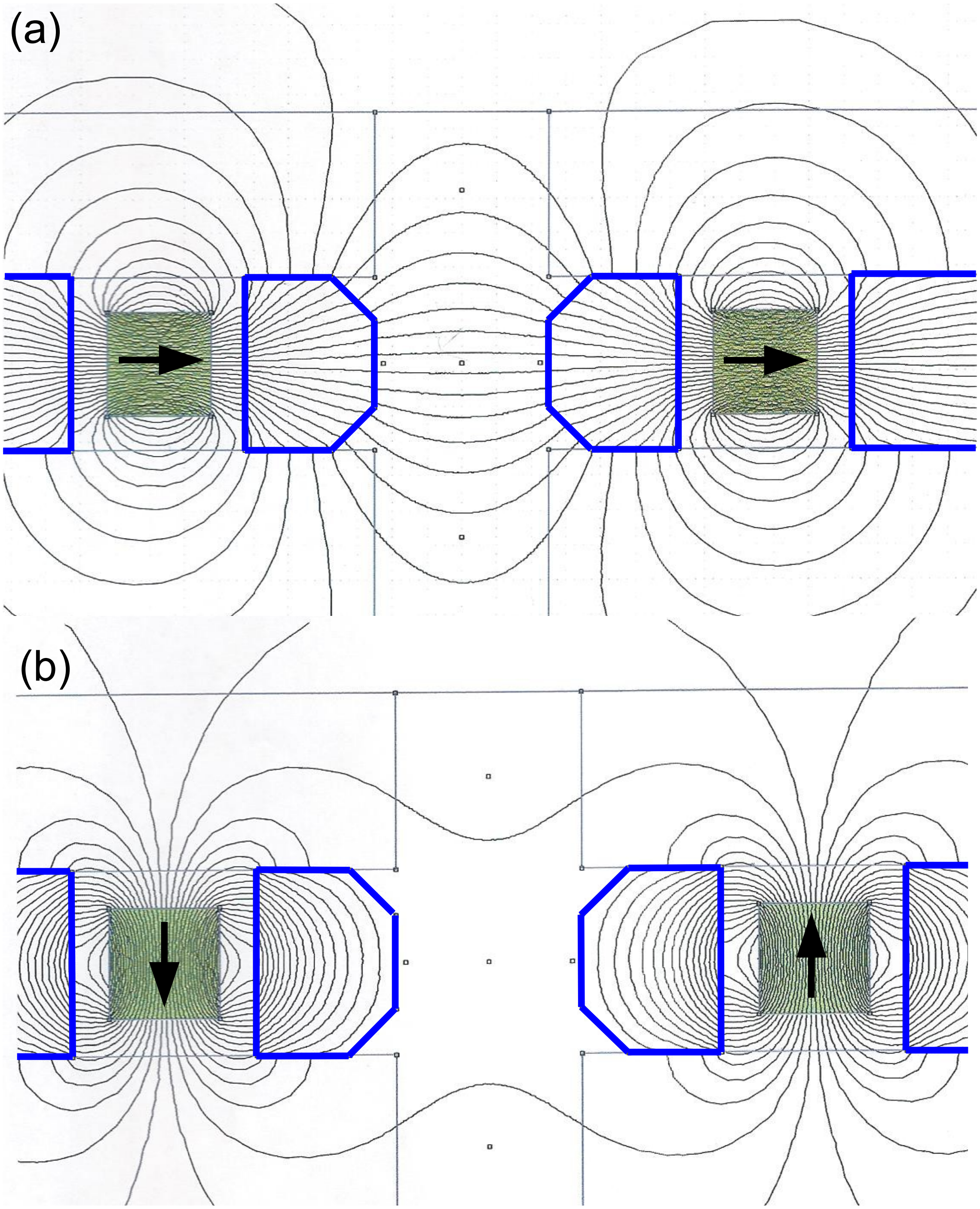

Figure A.2: Top view of a simulation showing the magnetic field lines when magnets are (a) aligned collinear (for the high in-plane magnetic field configuration) and (b) aligned anti-parallel to each other (for the 0 applied field configuration). Figure from Dr. Jan Sandtner and Dr. Hannes Bleuler from the Institute de microtechnique, École Polytechnique Federale de Lausanne. Vectors were added to indicate magnetization direction of NdFeB magnets (in green). Region enclosed in blue are iron poles. Black represents magnetic field lines.

In order to calibrate the applied magnetic field in our experiment, the field distribution at maximum field, as a function of distance from the left pole face, was measured using a hall probe as shown by the red points in figure A.3. Originally the field strength at the centre of the two pole faces was not at the desired field strength, so iron shoes were glued to the faces of the NbFeB magnets (as per the suggestions of Dr. Jan Sandtner) to increase the field strength at the center of the two poles. These iron shoes are shown schematically in the inset of figure A.3.

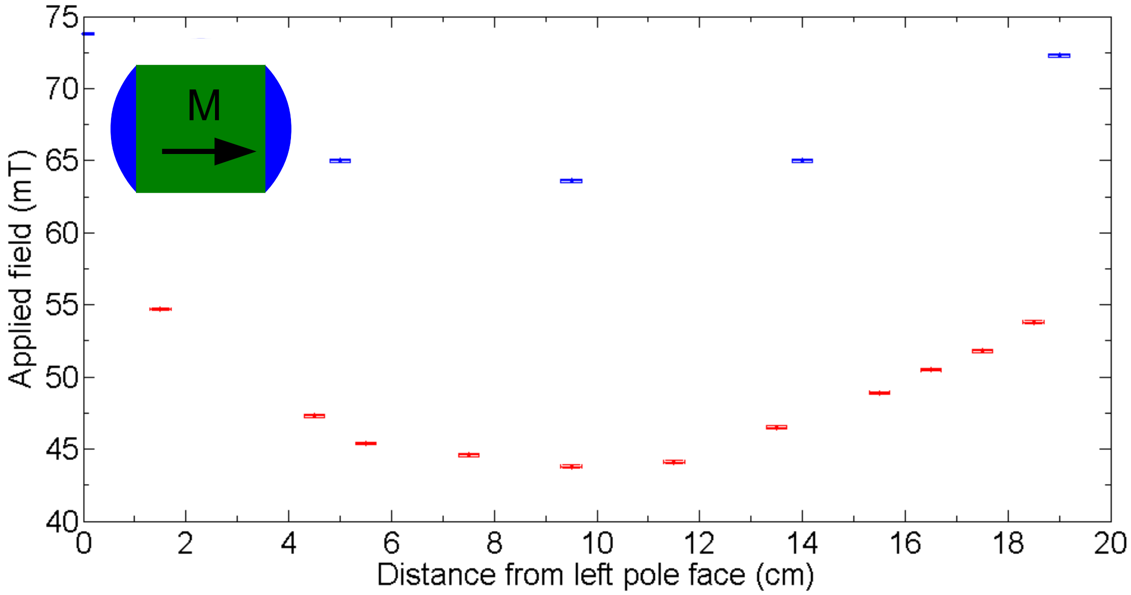

Figure A.3: Measured magnetic field as a function of distance from left iron pole. Red data points represent field before iron shoes are added to the sides of the NdFeB magnets as shown in the inset. Blue data points represent the field after shoes are added. Inset illustrates NdFeB magnet in green and iron shoes attached to both sides of the NdFeB magnet.

By fitting a parabola to the field as a function of distance from the left pole face (blue data points in figure A.3), the field was found to change by 0.03 mT for a 5 mm displacement from the center of the pole faces. Over the length scale of the magnetic arrays (20 μm), the field is much more uniform than the switching field distribution which means the spatial non-uniformity in the applied magnetic field does not have an influence on the switching field of the measured nanomagnets.

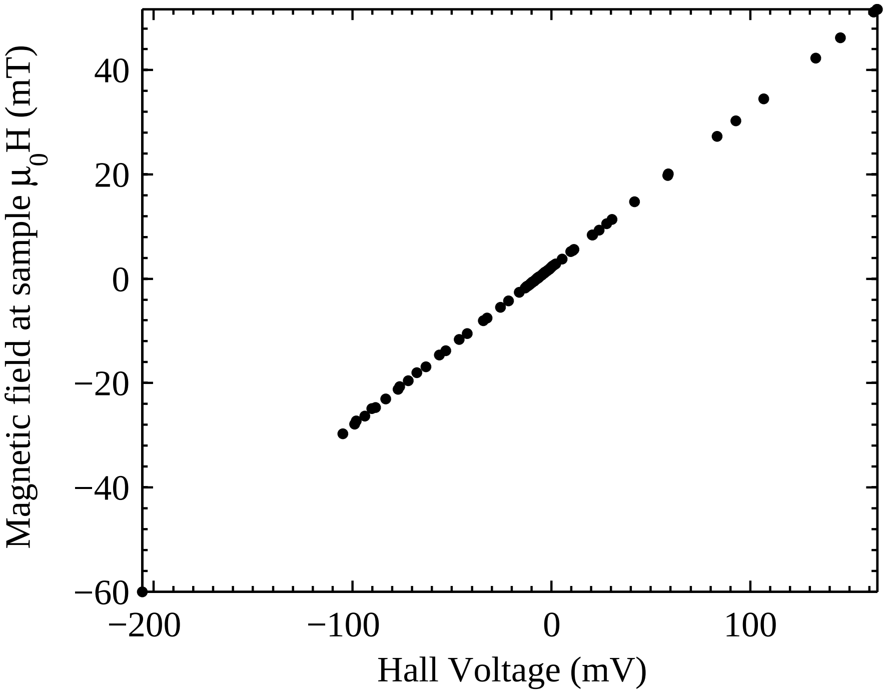

Figure A.4: Magnetic field at centre of iron poles as a function of hall probe voltage. Hall probe is located on the face of the soft iron poles shown in figure A.1.

To measure the field as a function of the position between the magnets during an MFM experiment, two hall probes were mounted on the soft iron pole faces. The magnetic field at the sample position was measured as a function of the hall probe voltage shown in figure A.4. The magnetic field at the sample position as a function of hall voltage is given by,

$$\mu_0 H(mT) = (-0.3022 \pm 0.0001) V_{avg}(mV) + (2.19 \pm 0.08) \qquad \text{(A.1)}$$

where V_{avg} is the average of the hall voltages on the two pole faces.

A.2 Interferometer positioning and setup

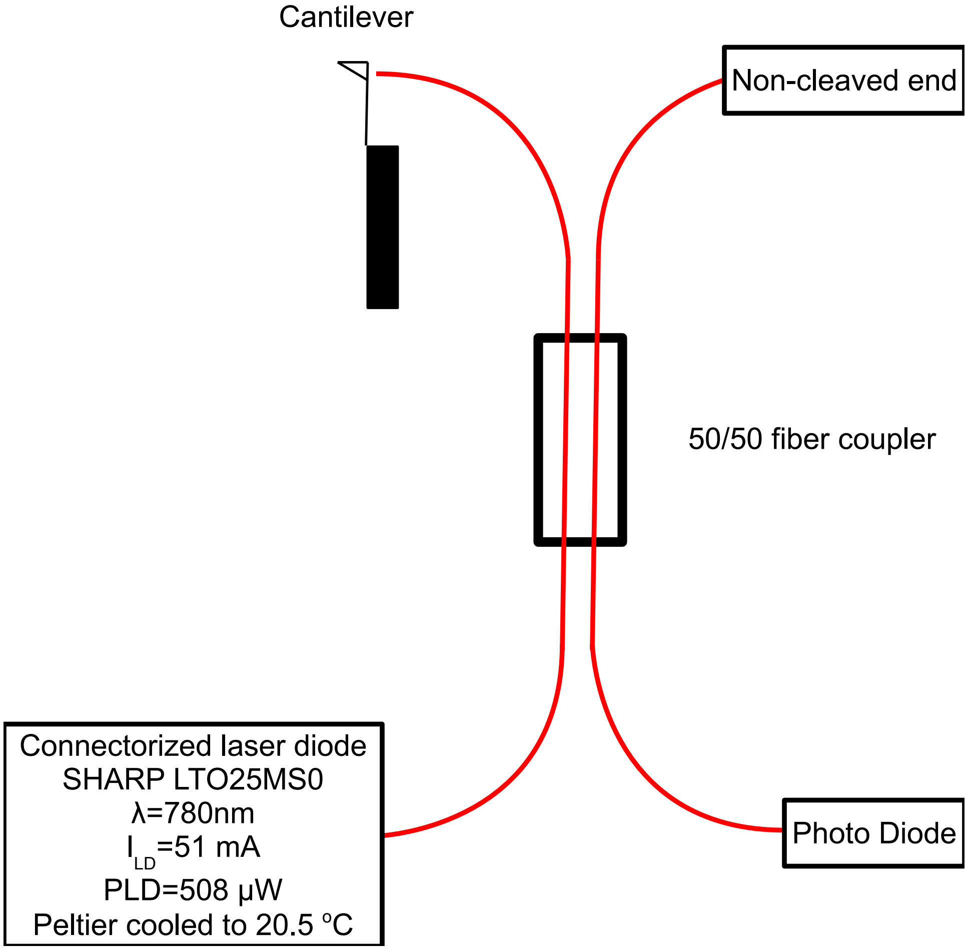

Figure A.5: Schematic of the interferometer setup. A connectorized laser diode with a wavelength of 780 nm directs laser light through a single mode optical fiber. The interference between light reflected off of the cantilever and light reflected off of the fiber-air interface is measured at the photo diode.

To measure the resonance frequency of the cantilever a fiber optic interferometer was used. It consists of a connectorized laser diode with a wavelength of 780 nm and a power of 508 μW. The laser light passes through a 50/50 splitter and then to a cleaved fiber. The cleaved fiber is brought close to the cantilever (typically less then 50 μm) so that the light that leaves the cleaved fiber end is reflected off of the cantilever and then re-enters the fiber (fiber walker positioning apparatus shown in below). This light interferes with light that is reflected off of the fiber-air interface. This interference depends on the fiber-cantilever separation, and is detected at the photo-diode after the light passes through the 50/50 splitter shown in figure A.5. Because the optical fiber is kept stationary, the fiber-cantilever separation gives a measure of the cantilever deflection. The end of the fiber leaving the 50/50 splitter that is not used is not cleaved to reduce the back reflection. This reduces the background light detected by the photodiode, and both improves the signal to noise and protects the diode from saturation. Because the wavelength of laser light depends on the temperature of the laser diode, a Peltier cooling element was placed on the laser diode casing that was connected using thermal paste to a heat sink to maintain a constant temperature of 20.5 °C.

So that the fiber optic interferometer position could be adjusted a fiber optic interferometer walker was designed, machined and assembled as shown in exploded view in figure A.6. The fiber optic interferometer walker allows the fiber-cantilever position to be adjusted by steps as small as 10 nm and as large as hundreds of micrometers. The large range is necessary so that the fiber can be retracted and the cantilever precisely positioned over the sample, as described in section 2.3. The small step size allows the fiber cantilever position to be reliably positioned in the center of an interference fringe.

The fiber optic cable is secured in a cylinder that is screwed into the slider. The slider is shown in figure A.6. Three stacks of shear piezoelectric elements (EBL2 from EBL products, Inc.) apply pressure on 3 sides of the slider. By ramping the piezo stack applied voltage slowly to approximately 100 V, the piezo stacks shear pushes the slider. The voltage is then quickly brought back to -100 V, causing

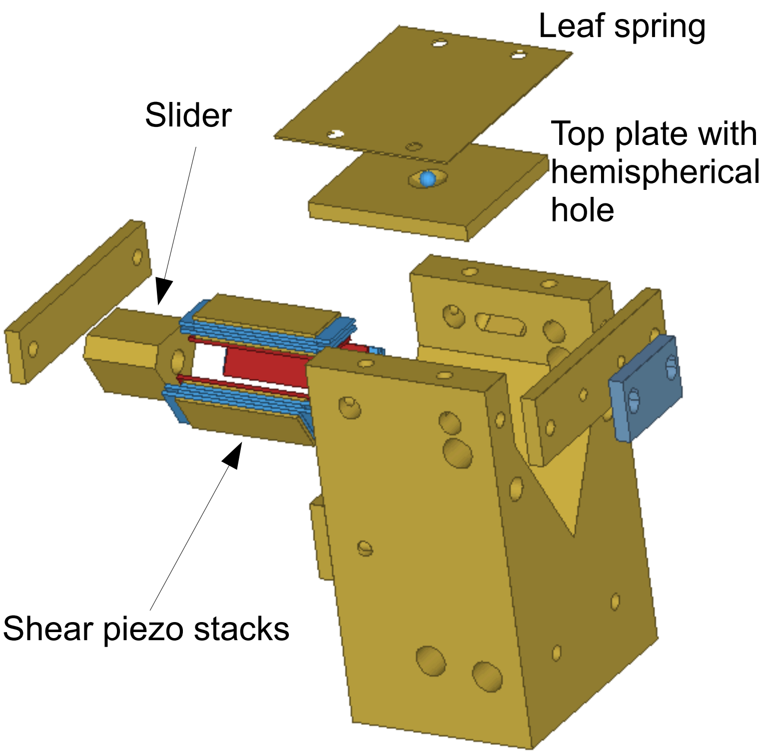

Figure A.6: Exploded view of fiber optic interferometer walker. blue represents shear piezo stacks, red represents sapphire plates that are stacked onto alumina plates. The top plate has a spherical hole with a ball that is smaller in diameter then then the diameter of the hole.

the piezo stacks to rapidly shear in the opposite direction. The slider holding the fiber slips remaining in the same position. This sawtooth pattern is repeated to move the slider in a stick-slip fashion in one direction. The leaf spring (shown in A.6) is used to adjust the pressure so that the slider moves the fiber smoothly both towards and away from the cantilever.

The piezo stacks are made by gluing alternating stacks of shear piezo and copper foil using H20E epoxy. On the base and top of the stack a piece of alumina is glued. Sapphire plates are then glued to the three faces of the slider. The first stack is glued to the top plate using Stycast 2850 FT thermally conductive epoxy and the epoxy is allowed to cure. Next the bottom two stacks are glued in place with all the components assembled, this insures that the faces will be parallel once the epoxy has cured. The piezo, alumina and sapphire pieces were cut using a diamond tip saw. To maintain the piezo walker alignment while being able to adjust the clamping force of the slider, a spherical sapphire ball sits in semi-spherical hole in the top plate with a larger diameter. This also reduces torque on the top piezo stack.

Due to the high capacitance of the piezo stacks, and the need for a high bandwidth to create a sharp sawtooth pattern a high bandwidth transformer was used to amplify the drive signal. A potential design improvement would be to make 6 smaller piezo stacks in stead of 3 larger piezo stacks. This would drastically reduce the capacitance of the stacks, making them easier to drive but would complicate the gluing process due to the additional number of stacks that would be glued at once.

A.3 Variable field AFM apparatus

As mentioned in section 4.2 eddy currents in the microscope components cause them to heat up, which causes microscope drift. To minimize the drift another piezo walker and microscope head machined out of Delrin. This was done to reduce the eddy currents caused by the variable magnetic field. These eddy currents caused the conductive parts of the original microscope head to heat up, causing them to expand. When the microscope head expanded, the fiber-cantilever gap changed, causing the interference detection signal to drift.

To prevent the possibility of the sample holder expanding due to eddy current induced heating a new insulating sample holder was also machined out of

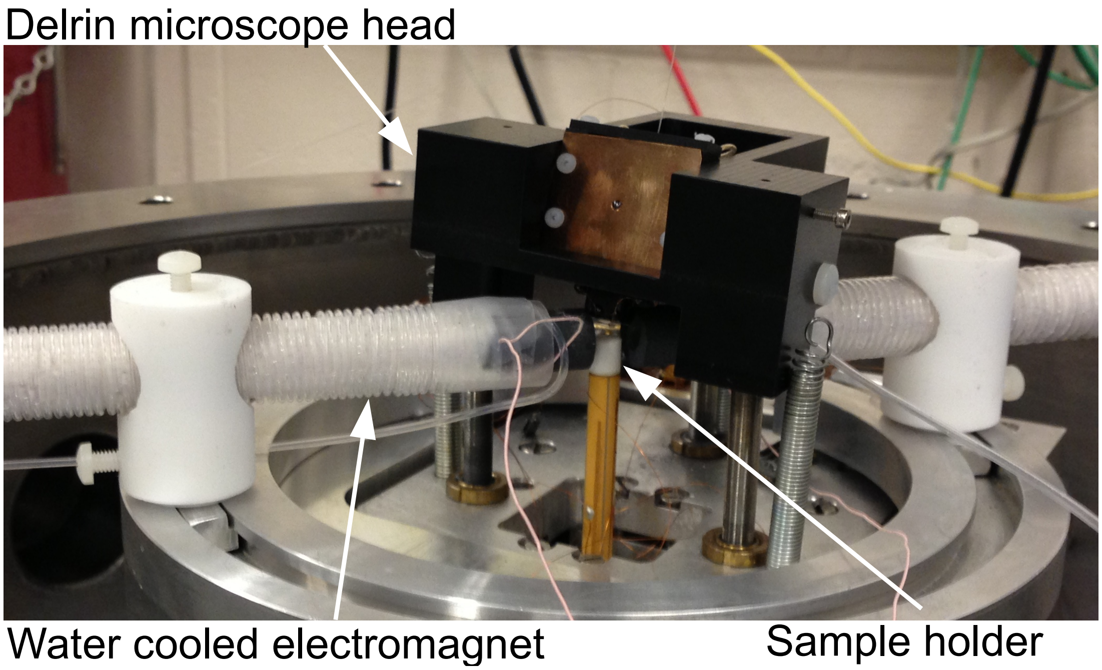

Figure A.7: Microscope set up for variable field MFM. Delrin microscope head with water cooled electromagnets made by wrapping Litz wire around a ferrite core. Macor sample holder with thin copper grounding piece.

Macor. A grounded copper plate was necessary to shield the electric field, caused by the 300 V being applied to the piezo tube, from the tip and sample. A picture of the assembled Delrin microscope head with insulating sample holder is shown in figure A.7.

These changes successfully resulted in a decrease in the interferometer drift from 5 nm per second to 0.5 nm per second.

A.4 Phase-locked loop

A PLL is used to measure the resonance frequency change in the AFM cantilever as shown in figure A.8. It consists of a phase detector (multiplier and a low-pass filter in which the cutoff frequency is below twice the operating frequency of

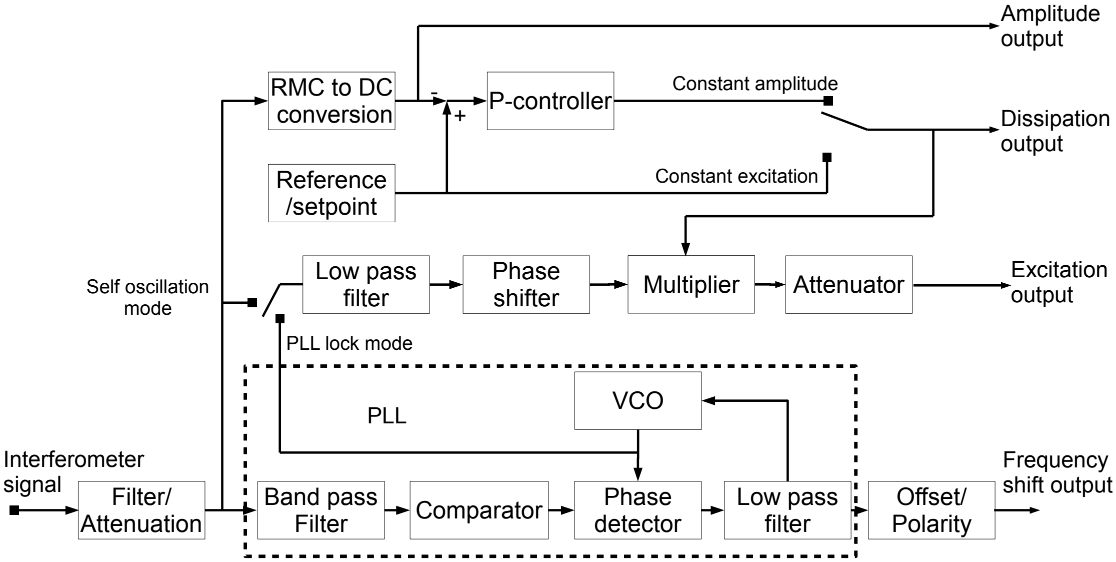

Figure A.8: Schematic of control loop that measures the cantilever resonance frequency shifts, amplitude of cantilever oscillation, and dissipation in the cantilever. The resonance frequency shift of the cantilever is measured using a PLL block. The frequency of the cantilever excitation can be either from the interferometer (deflection) signal (self oscillation mode) or using the output from the VCO in the PLL (PLL lock mode). The amplitude of the signal can either be kept constant using a controller (constant amplitude) or can be driven with a constant drive signal (constant excitation).

the cantilever) and a voltage controlled oscillator (VCO) [150]. At steady state the output frequency of the VCO is the same as the cantilever frequency. The input to the VCO is zeroed when the cantilever is in free oscillation with no interaction. When there is an interaction between the cantilever's tip and sample, the frequency shift is measured from the input to the VCO [150].

B

Edge detection

The following are bright field TEM images of the nanostructures analyzed in section 3 and the results of the edge detection procedure.

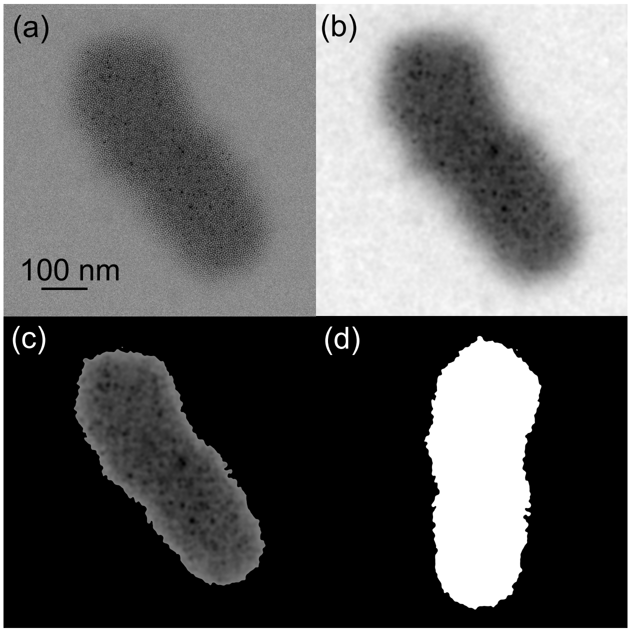

Figure B.1: (a)TEM image of nanostructure in row 3 column 4 with a coercivity of 0.36 mT. (b) TEM image convolved with a Gaussian. (c) Edge detection using a threshold of 0.5. (d) Result of the edge detection procedure.

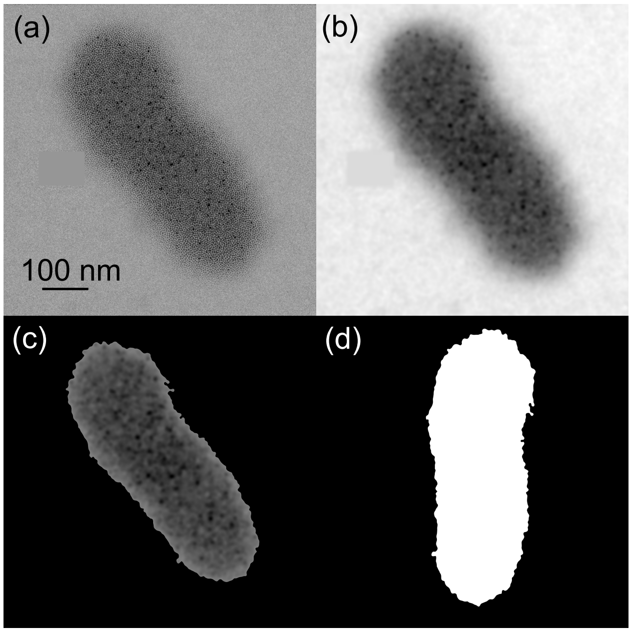

Figure B.2: (a)TEM image of nanostructure in row 3 column 5 with a coercivity of 0.36 mT. (b) TEM image convolved with a Gaussian. (c) Edge detection using a threshold of 0.5. (d) Result of the edge detection procedure.

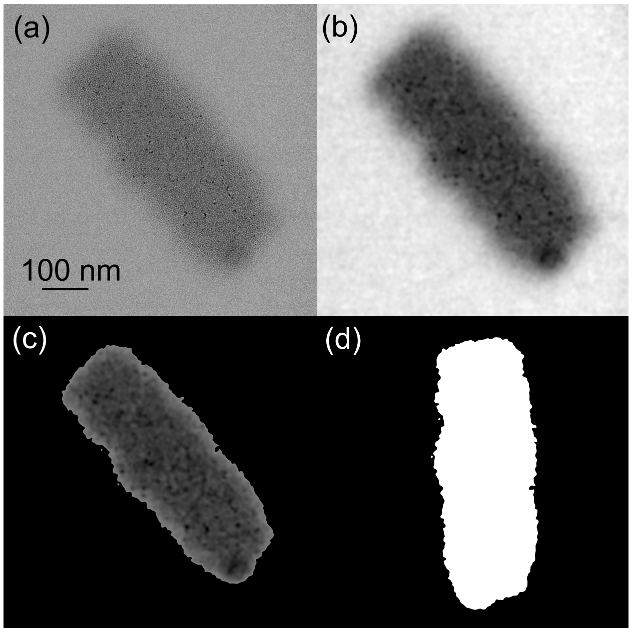

Figure B.3: (a)TEM image of nanostructure in row 1 column 2 with a coercivity of 0.39 mT. (b) TEM image convolved with a Gaussian. (c) Edge detection using a threshold of 0.5. (d) Result of the edge detection procedure.

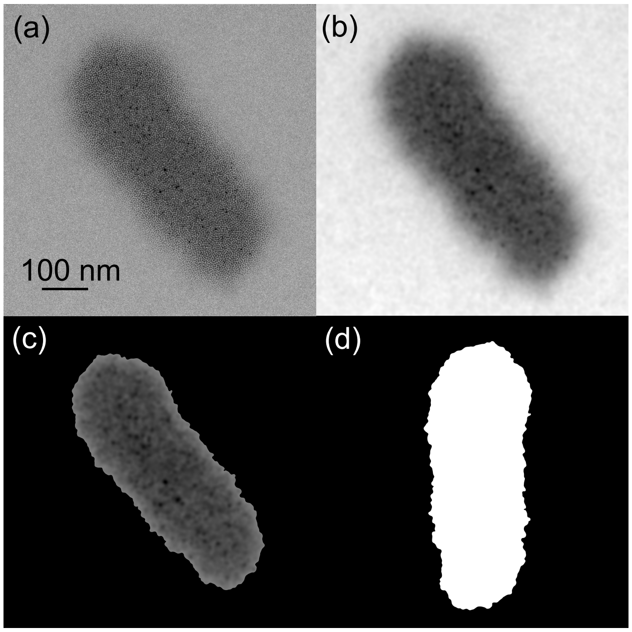

Figure B.4: (a)TEM image of nanostructure in row 2 column 3 with a coercivity of 0.61 mT. (b) TEM image convolved with a Gaussian. (c) Edge detection using a threshold of 0.5. (d) Result of the edge detection procedure.

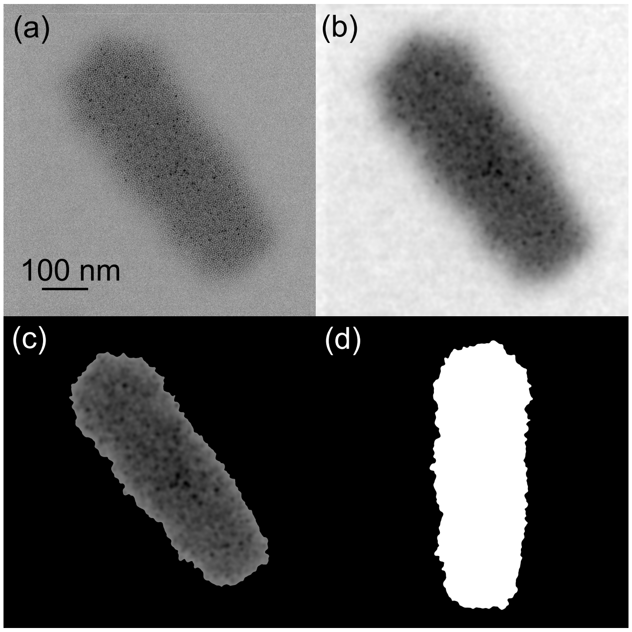

Figure B.5: (a)TEM image of nanostructure in row 3 column 2 with a coercivity of 0.71 mT. (b) TEM image convolved with a Gaussian. (c) Edge detection using a threshold of 0.5. (d) Result of the edge detection procedure.

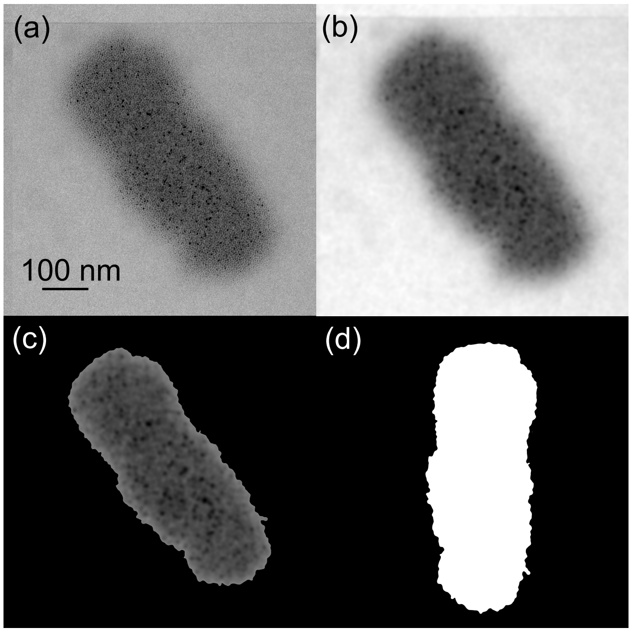

Figure B.6: (a)TEM image of nanostructure in row 1 column 3 with a coercivity of 0.78 mT. (b) TEM image convolved with a Gaussian. (c) Edge detection using a threshold of 0.5. (d) Result of the edge detection procedure.

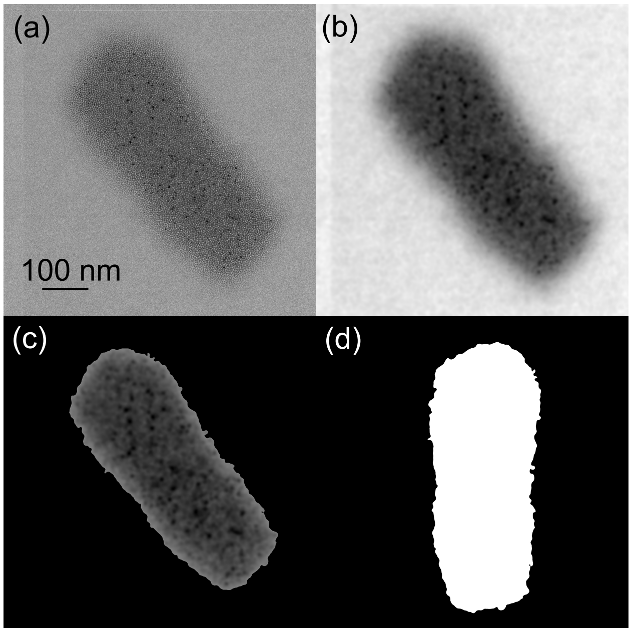

Figure B.7: (a)TEM image of nanostructure in row 1 column 5 with a coercivity of 0.78 mT. (b) TEM image convolved with a Gaussian. (c) Edge detection using a threshold of 0.5. (d) Result of the edge detection procedure.

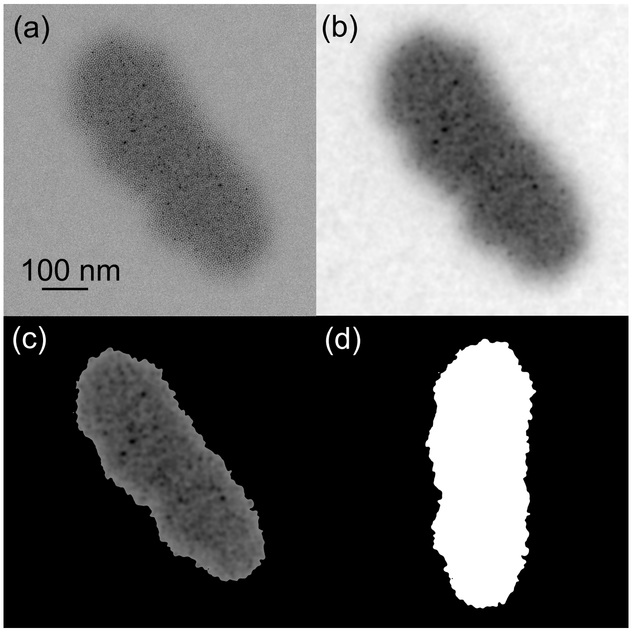

Figure B.8: (a)TEM image of nanostructure in row 2 column 4 with a coercivity of 0.78 mT. (b) TEM image convolved with a Gaussian. (c) Edge detection using a threshold of 0.5. (d) Result of the edge detection procedure.

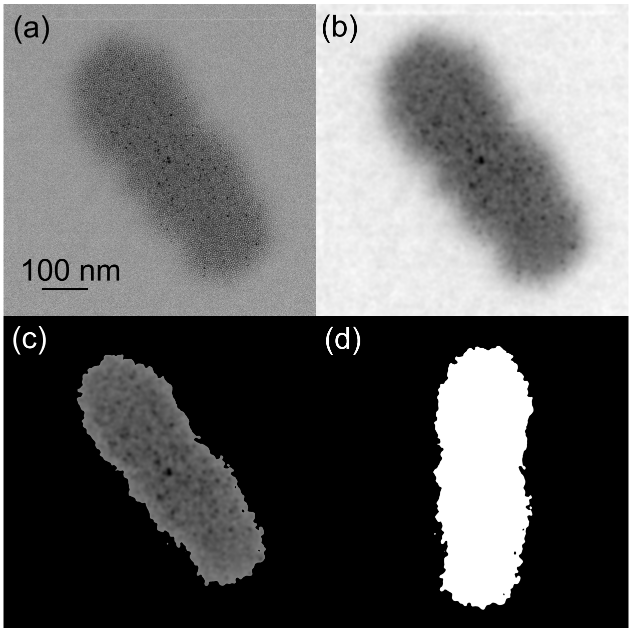

Figure B.9: (a)TEM image of nanostructure in row 2 column 5 with a coercivity of 0.87 mT. (b) TEM image convolved with a Gaussian. (c) Edge detection using a threshold of 0.5. (d) Result of the edge detection procedure.

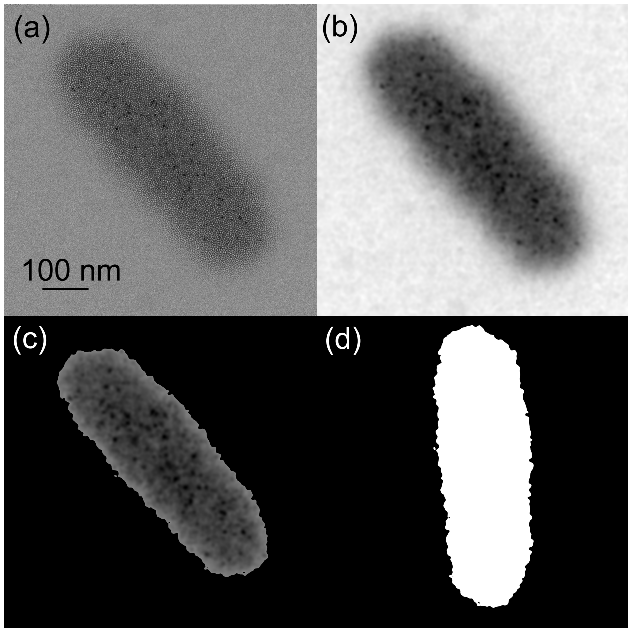

Figure B.10: (a)TEM image of nanostructure in row 3 column 1 with a coercivity of 1.02 mT. (b) TEM image convolved with a Gaussian. (c) Edge detection using a threshold of 0.5. (d) Result of the edge detection procedure.

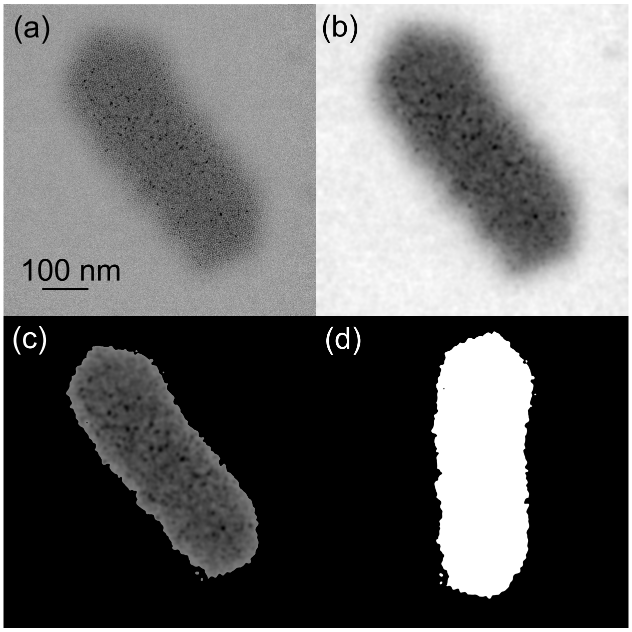

Figure B.11: (a)TEM image of nanostructure in row 1 column 4 with a coercivity of 1.24 mT. (b) TEM image convolved with a Gaussian. (c) Edge detection using a threshold of 0.5. (d) Result of the edge detection procedure.

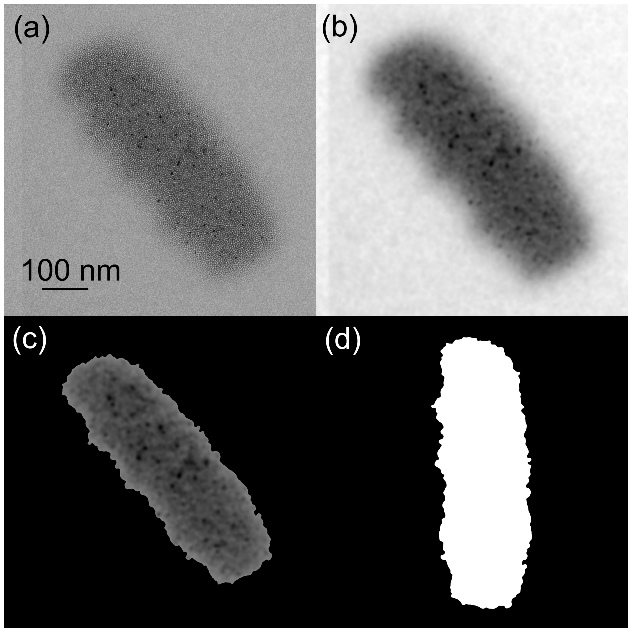

Figure B.12: (a)TEM image of nanostructure in row 2 column 1 with a coercivity of 1.30 mT. (b) TEM image convolved with a Gaussian. (c) Edge detection using a threshold of 0.5. (d) Result of the edge detection procedure.

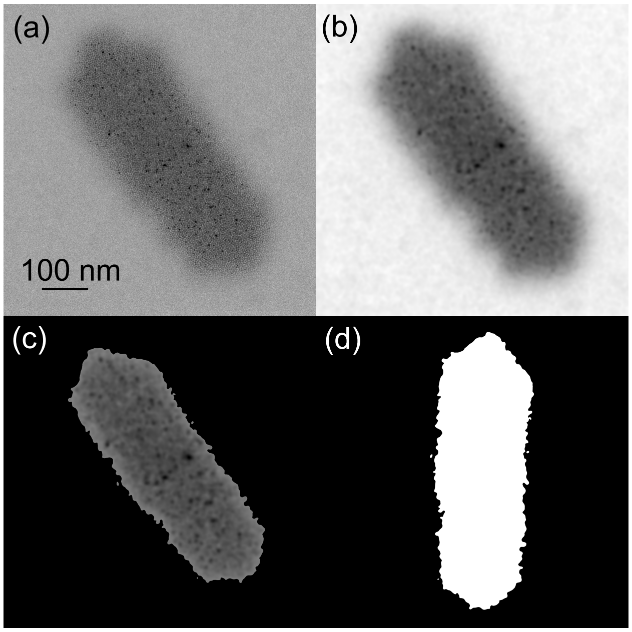

Figure B.13: (a)TEM image of nanostructure in row 2 column 2 with a coercivity of 1.33 mT. (b) TEM image convolved with a Gaussian. (c) Edge detection using a threshold of 0.5. (d) Result of the edge detection procedure.

Bibliography

[1] GA Prinz. Magnetoelectronics applications. *Journal of Magnetism and Magnetic Materials*, 200(January):57–68, 1999.

[2] M Julliere. Tunneling between ferromagnetic films. *Physics Letters A*, 54(3):225–226, 1975.

[3] T Miyazaki and N Tezuka. Giant Magnetic Tunneling Effect in Fe/Al2O3/Fe Junction. *Journal of Magnetism and Magnetic Materials*, 139:L231–L234, 1995.

[4] JS Moodera, LR Kinder, TM Wong, and R Meservey. Large magnetoresistance at room temperature in ferromagnetic thin film tunnel junctions. *Physical Review Letters*, 74(16):3273–3276, 1995.

[5] S. Parkin, C. Kaiser, A. Panchula, K. Roche, and M. Samant. Magnetically engineered spintronic sensors and memory. *Proceedings of the IEEE*, 91(5):661–680, May 2003.

[6] Youfeng Zheng and Jian-Gang Zhu. Switching field variation in patterned submicron magnetic film elements. In *The 41st annual conference on magnetism and magnetic materials*, volume 81, pages 5471–5473, Atlanta, Georgia (USA), April 1997. AIP.

[7] R. P. Cowburn. Room Temperature Magnetic Quantum Cellular Automata. *Science*, 287(5457):1466–1468, February 2000.

[8] R. Engel-Herbert, S. A. Haque, and T. Hesjedal. Systematic investigation of Permalloy nanostructures for magnetologic applications. *Journal of Applied Physics*, 101(9):09F503, 2007.

[9] G Bernstein, A Imre, V Metlushko, A Orlov, L Zhou, L Ji, G Csaba, and W Porod. Magnetic QCA systems. *Microelectronics Journal*, 36(7):619–624, July 2005.

[10] A. Orlov, A. Imre, G. Csaba, L. Ji, W. Porod, and G. H. Bernstein. Magnetic Quantum-Dot Cellular Automata: Recent Developments and Prospects. *Journal of Nanoelectronics and Optoelectronics*, 3(1):55–68, March 2008.

[11] M T Bryan, D Atkinson, and R P Cowburn. Edge roughness and coercivity in magnetic nanostructures. *Journal of Physics: Conference Series*, 17:40–44, January 2005.

[12] W Wernsdorfer. Magnetization reversal in individual nanoparticles: macroscopic quantum tunneling of magnetization. *Magnetics, IEEE . . .*, 34(4), 1998.

[13] M Schneider. Magnetisation reversal of thin submicron elliptical permalloy elements. *Journal of Magnetism and Magnetic Materials*, 257(1):1–10, February 2003.

[14] M Schneider, J Liszkowski, M Rahm, W Wegscheider, D Weiss, H Hoffmann, and J Zweck. Magnetization configurations and hysteresis loops of small permalloy ellipses. *Journal of Physics D: Applied Physics*, 36(18):2239–2243, September 2003.

[15] MT Bryan, D. Atkinson, and RP Cowburn. Experimental study of the influence of edge roughness on magnetization switching in Permalloy nanostructures. *Applied Physics Letters*, 85(16):3510, 2004.

[16] M T Bryan, D Atkinson, and R. P. Cowburn. Edge roughness and coercivity in magnetic nanostructures. *Journal of Physics: Conference Series*, 17:40–44, January 2005.

[17] Jason Gadbois and JG Zhu. Effect of edge roughness in nano-scale magnetic bar switching. *Magnetics, IEEE Transactions on*, 31(6):3802–3804, 1995.

[18] J G Deak and R H Koch. The effect of edge roughness on magnetization reversal in micron-sized permalloy thin films. *Journal of Magnetism and Magnetic Materials*, 213(1-2):25–31, April 2000.

[19] J. W. Lau, R. D. McMichael, M. A. Schofield, and Y. Zhu. Correlation of edge roughness to nucleation field and nucleation field distribution in patterned Permalloy elements. *Journal of Applied Physics*, 102(2):023916, 2007.

[20] Rok Dittrich, Thomas Schrefl, André Thiaville, Jacques Miltat, Vassilios Tsiantos, and Josef Fidler. Comparison of Langevin dynamics and direct energy barrier computation. *Journal of Magnetism and Magnetic Materials*, 272-276:747–749, May 2004.

[21] Han-Ting Wang, S. Chui, a. Oriade, and J. Shi. Temperature dependence of the fluctuation of the switching field in small magnetic structures. *Physical Review B*, 69(6):064417, February 2004.

[22] JBC B C Engelen, M Delalande, AJ J le Fèbre, T Bolhuis, T Shimatsu, N Kikuchi, L Abelmann, and JC C Lodder. Thermally induced switching field dis-

tribution of a single CoPt dot in a large array. *Nanotechnology*, 21(3):035703, January 2010.

[23] K. J. Kirk, J. N. Chapman, S. McVitie, P. R. Aitchison, and C. D. W. Wilkinson. Interactions and switching field distributions of nanoscale magnetic elements. *Journal of Applied Physics*, 87(9):5105, 2000.

[24] J. W. Lau, R. D. McMichael, S. H. Chung, J. O. Rantschler, V. Parekh, and D. Litvinov. Microstructural origin of switching field distribution in patterned CoPd multilayer nanodots. *Applied Physics Letters*, 92(1):012506, 2008.

[25] June W Lau and Justin M Shaw. Magnetic nanostructures for advanced technologies: fabrication, metrology and challenges. *Journal of Physics D: Applied Physics*, 44(30):303001, August 2011.

[26] Jr W. F. Brown. Virtues and weaknesses of the domain concept. *Reviews of Modern Physics*, 17(336), 1945.

[27] U Hartmann. Origin of Brown's coercive paradox in perfect ferromagnetic crystals. *Physical Review B*, 36(4):2331–2333, 1987.

[28] GP Zhao and XL Wang. Nucleation, pinning, and coercivity in magnetic nanosystems: An analytical micromagnetic approach. *Physical Review B*, pages 2–5, 2006.

[29] G. P. Zhao, M. G. Zhao, H. S. Lim, Y. P. Feng, and C. K. Ong. From nucleation to coercivity. *Applied Physics Letters*, 87(16):162513, 2005.

[30] C.J. Chen. *Introduction to Scanning Tunneling Microscopy*. Oxford University Press, New York, 1993.

[31] S. Morita, R. Wiesendanger, and E. Meyer. *Noncontact Atomic Force Microscopy*. Springer, Berlin 2002, 2002.

[32] P. Girard, M. Ramonda, and R. Arinero. Dynamic atomic force microscopy operation based on high flexure modes of the cantilever. *Review of Scientific Instruments*, 77(9):096105, 2006.

[33] Q Zhong, D Inniss, K Kjoller, and VB Elings. Fractured polymer/silica fiber surface studied by tapping mode atomic force microscopy. *Surface Science Letters*, 290, 1993.

[34] T R Albrecht, P. Grutter, D Horne, and D Rugar. Frequency modulation detection using high-Q cantilevers for enhanced force microscope sensitivity. *Journal of Applied Physics*, 69(2):668, 1991.

[35] Franz J Giessibl, Yasuhiro Sugawara, Seizo Morita, and Hirotaka Hosoi. *Nanotribology and Nanomechanics I*. Number 4. Springer Berlin Heidelberg, Berlin, Heidelberg, 2011.

[36] S. Hembacher, F.J. Giessibl, and J. Mannhart. Evaluation of a force sensor based on a quartz tuning fork for operation at low temperatures and ultrahigh vacuum. *Applied surface science*, 188(3-4):445–449, March 2002.

[37] M Nonnenmacher, M. P. OBoyle, and H. K. Wickramasinghe. Kelvin probe force microscopy. *Applied Physics Letters*, 58(25):2921, 1991.

[38] Aleksander Labuda, Yoichi Miyahara, Lynda Cockins, and Peter H. Grütter. Decoupling conservative and dissipative forces in frequency modulation atomic force microscopy. *Physical Review B*, 84(12):125433, September 2011.

[39] U. Durig, H. R. Steinauer, and N. Blanc. Dynamic force microscopy by means of the phase-controlled oscillator method. *Journal of Applied Physics*, 82(8):3641, 1997.

[40] Y. Martin and H. K. Wickramasinghe. Magnetic imaging by force microscopy with 1000 AŁ resolution. *Applied Physics Letters*, 50(20):1455, 1987.

[41] Y. Martin, C. C. Williams, and H. K. Wickramasinghe. Atomic force microscope force mapping and profiling on a sub 100Åscale. *Journal of Applied Physics*, 61(10):4723, 1987.

[42] R Wiesendanger. Magnetic Force Microscopy (MFM). In Roland Wiesendanger and H.-J. Guntherodt, editors, *Scanning tunneling microscopy II*, volume 28, chapter 5. Springer, Verlag Berlin Heidelberg, 1992.

[43] H Hopster and HP Oepen. Magnetic Force Microscopy: Images of Nanostructures and Contrast Modeling. In *Magnetic Microscopy of Nanostructures*, chapter Chapter 11, pages 225–251. 2004.

[44] J. Mallinson. On the Properties of Two-Dimensional Dipoles and Magnetized Bodies. *IEEE Transactions on Magnetics*, 17(5):2453–2460, September 1981.

[45] Xiaobin Zhu, P. Grutter, V. Metlushko, and B. Ilic. Systematic study of magnetic tip induced magnetization reversal of e-beam patterned permalloy particles. *Journal of Applied Physics*, 91(10):7340, 2002.

[46] Xiaobin Zhu. *Magnetic Force Microscopy Studies of Submicron and Nanoscale Magnet Arrays*. PhD thesis, McGill University, 2002.

[47] Jannis Lübbe, Matthias Temmen, Holger Schnieder, and Michael Reichling. Measurement and modelling of non-contact atomic force microscope cantilever properties from ultra-high vacuum to normal pressure conditions. *Measurement Science and Technology*, 22(5):055501, May 2011.

[48] B. Mokaberi and A.A.G. Requicha. Drift compensation for automatic nanomanipulation with scanning probe microscopes. *IEEE Transactions on Automation Science and Engineering*, 3(3):199–207, July 2006.

[49] S O Reza Moheimani. Invited review article: accurate and fast nanopositioning with piezoelectric tube scanners: emerging trends and future challenges. *The Review of scientific instruments*, 79(7):071101, July 2008.

[50] O.M. El-Rifai and K. Youcef-Toumi. Creep in piezoelectric scanners of atomic force microscopes. *Proceedings of the 2002 American Control Conference (IEEE Cat. No.CH37301)*, 5:3777–3782, 2002.

[51] S. Krause, G. Herzog, T. Stapelfeldt, L. Berbil-Bautista, M. Bode, E. Y. Vedmedenko, and R. Wiesendanger. Magnetization Reversal of Nanoscale Islands: How Size and Shape Affect the Arrhenius Prefactor. *Physical Review Letters*, 103(12):1–4, 2009.

[52] M.J. Donahue and D.G. Porter. OOMMF User's Guide, Version 1.0. *Interagency Report NISTIR 6376, National Institute of Standards and Technology, Gaithersburg, MD*, 1999.

[53] JE Miltat and MJ Donahue. Numerical micromagnetics: finite difference methods. *Handbook of Magnetism and . . .* , pages 1–23, 2007.

[54] Thomas L Gilbert. A Phenomenological Theory of Damping in Ferromagnetic Materials. *IEEE Transactions on Magnetics*, 40(6):3443–3449, 2004.

[55] S Mizukami. Ferromagnetic resonance linewidth for NM/80NiFe/NM films (NM=Cu, Ta, Pd and Pt). *Journal of Magnetism and Magnetic Materials*, 226-230:1640–1642, May 2001.

[56] W.F. Brown Jr and W.F. Brown. Thermal fluctuations of a single-domain particle. *Physical Review*, 130(5):1677–1686, 1963.

[57] H Kronmüller. General micromagnetic theory. *Handbook of Magnetism and Advanced . . .* , 2007.

[58] DR Lide and TJ Bruno. *CRC handbook of chemistry and physics*. Number curve c. 93 edition, 2012.

[59] J.A.C Bland and B. Heinrich. *Ultrathin Magnetic Structures I*. Springer-Verlag, Berlin/Heidelberg, 2005.

[60] AJ Newell. A generalization of the demagnetizing tensor for nonuniform magnetization. *Journal of Geophysical . . .* , 98(7):9551–9555, 1993.

[61] John D. Jackson. *Classical Electrodynamics Third Edition*. 1998.

[62] D Donnelly and B Rust. The fast Fourier transform for experimentalists. Part I. Concepts. *Computing in Science & Engineering*, pages 80–88, 2005.

[63] D Donnelly and B Rust. The fast Fourier transform for experimentalists. Part II. convolutions. *Computing in Science & Engineering*, (3):92–95, 2005.

[64] Zhi-Min Liao, Yi Lu, Hong-Zhou Zhang, and Da-Peng Yu. Hysteresis magnetoresistance and micromagnetic modeling of Ni microbelts. *Journal of Magnetism and Magnetic Materials*, 322(15):2231–2234, August 2010.

[65] S.W. Yuan and H.N. Bertram. Size effects of switching fields of thin Permalloy particles. *. . . , IEEE Transactions on*, 28(5):3171–3173, 1992.

[66] E. C. Stoner and E. P. Wohlfarth. A Mechanism of Magnetic Hysteresis in Heterogeneous Alloys. *Philosophical Transactions of the Royal Society A: Mathematical, Physical and Engineering Sciences*, 240(826):599–642, May 1948.

[67] TR Koehler and DR Fredkin. Micromagnetic modeling of permalloy particles: thickness effects. *Magnetics, IEEE Transactions on*, 27(6):4763–4765, 1991.

[68] S Polisetty, J Scheffler, S Sahoo, Yi Wang, T Mukherjee, Xi He, and Ch Binek. Optimization of magneto-optical Kerr setup: analyzing experimental assemblies using Jones matrix formalism. *The Review of scientific instruments*, 79(5):055107, 2008.

[69] D A Allwood, Gang Xiong, M D Cooke, and R P Cowburn. Magneto-optical Kerr effect analysis of magnetic nanostructures. *Journal of Physics D: Applied Physics*, 36(18):2175–2182, September 2003.

[70] ZQ Qiu and SD Bader. Surface magneto-optic Kerr effect (SMOKE). *Journal of magnetism and magnetic materials*, 200:664–678, 1999.

[71] J Zak, ER Moog, C Liu, and SD Bader. Universal approach to magneto-optics. *Journal of Magnetism and Magnetic . . .* , 89:107–123, 1990.

[72] J. Zak, E. R. Moog, C. Liu, and S. D. Bader. Fundamental magneto-optics. *Journal of Applied Physics*, 68(8):4203, 1990.

[73] H Hopster and HP Oepen. *Magnetic microscopy of nanostructures*. 2004.

[74] M. A. Akhter, D. J. Mapps, Y. Q. Ma Tan, Amanda Petford-Long, and R. Doole. Thickness and grain-size dependence of the coercivity in permalloy thin films. *Journal of Applied Physics*, 81(8):4122, 1997.

[75] RF Egerton. Analytical Electron Microscopy. In *Physical Principles of Electron Microscopy: An Introduction to TEM, SEM, and AEM*, chapter Chapter 6, pages 155–175. 2005.

[76] DB Williams and CB Carter. Transmission electron microscopy: a textbook for materials science. In *Transmission electron microscopy: a textbook for materials science*. 2009.

[77] A Thompson, D Attwood, E Gullikson, M Howells, KJ Kim, J Kirz, J Kortright, I Lindau, Y Liu, P Pianetta, A Robinson, J Scofield, J Underwood, G Williams, and H Winick. *X-ray data booklet*. 2009.

[78] B. Fultz and J.M. Howe. *Transmission Electron Microscopy and Diffractometry of Materials*. Springer Berlin Heidelberg, Berlin, Heidelberg, 2008.

[79] CC Ahn. Transmission electron energy loss spectrometry in materials science and the EELS atlas. chapter EELS Quant, pages 49–96. 2006.

[80] H.R. Verma. X-Ray Photoelectron Spectroscopy. In *Atomic and nuclear analytical methods: XRF, Mössbauer, XPS, NAA and ion-beam spectroscopic techniques*, chapter Chapter 5, pages 213–241. 2007.

[81] Alexander V. Naumkin, Anna Kraut-Vass, Stephen W. Gaarenstroom, and Cedric J. Powell. NIST X-ray Photoelectron Spectroscopy Database, 2012.

[82] LA Giannuzzi. The focused ion beam instrument. In *Introduction to focused ion beams: instrumentation, theory, techniques and practice*, chapter Chapter 1, pages 1–12. 2004.

[83] MY Ali, Wayne Hung, and Fu Yongqi. A review of focused ion beam sputtering. *International Journal of Precision Engineering ...*, 11(1):157–170, April 2010.

[84] C. Vieu. Evidence of depth and lateral diffusion of defects during focused ion beam implantation. *Journal of Vacuum Science & Technology B: Microelectronics and Nanometer Structures*, 16(4):1919, July 1998.

[85] G. Spoldi, S. Beuer, M. Rommel, V. Yanev, A.J. Bauer, and H. Ryssel. Experimental observation of FIB induced lateral damage on silicon samples. *Microelectronic Engineering*, 86(4-6):548–551, April 2009.

[86] M. Rommel, G. Spoldi, V. Yanev, S. Beuer, B. Amon, J. Jambreck, S. Petersen, A. J. Bauer, and L. Frey. Comprehensive study of focused ion beam induced lateral damage in silicon by scanning probe microscopy techniques. *Journal of Vacuum Science & Technology B: Microelectronics and Nanometer Structures*, 28(3):595, 2010.

[87] K Arshak and M Mihov. Focused ion beam lithography-overview and new approaches. *Microelectronics, . . .* , 2(May):16–19, 2004.

[88] Aleksander Labuda, Jeffrey R Bates, and Peter H Grütter. The noise of coated cantilevers. *Nanotechnology*, 23(2):025503, January 2012.

[89] R. L. Kubena. FET fabrication using maskless ion implantation. *Journal of Vacuum Science and Technology*, 19(4):916, November 1981.

[90] G. M. Shedd, H. Lezec, A. D. Dubner, and J. Melngailis. Focused ion beam induced deposition of gold. *Applied Physics Letters*, 49(23):1584, 1986.

[91] L.a. Giannuzzi and F.a. Stevie. A review of focused ion beam milling techniques for TEM specimen preparation. *Micron*, 30(3):197–204, June 1999.

[92] Steve Reyntjens and Robert Puers. A review of focused ion beam applications in microsystem technology. *Journal of Micromechanics and . . .* , 11(4):287–300, July 2001.

[93] John Melngailis. Focused ion beam technology and applications. *Journal of Vacuum Science & Technology B: Microelectronics and Nanometer Structures*, 5(2):469, March 1987.

[94] Mandar M. Deshmukh, DC C. Ralph, M. Thomas, and J. Silcox. Nanofabrication using a stencil mask. *Applied Physics Letters*, 75(11):1631, 1999.

[95] J Brugger, JW Berenschot, S Kuiper, W Nijdam, B Otter, and M Elwenspoek. Resistless patterning of sub-micron structures by evaporation through nanostencils. *Microelectronic Engineering*, 53(1-4):403–405, June 2000.

[96] L Gross, R R Schlittler, G Meyer, and R Allenspach. Magnetologic devices fabricated by nanostencil lithography. *Nanotechnology*, 21(32):325301, August 2010.

[97] SY Chou. Patterned magnetic nanostructures and quantized magnetic disks. *Proceedings of the IEEE*, 85(4):652–671, April 1997.

[98] J.I Martn, J Nogués, Kai Liu, J.L Vicent, and Ivan K Schuller. Ordered magnetic nanostructures: fabrication and properties. *Journal of Magnetism and Magnetic Materials*, 256(1-3):449–501, January 2003.

[99] C. A. Ross, Henry I. Smith, T. Savas, M. Schattenburg, M. Farhoud, M. Hwang, M. Walsh, M. C. Abraham, and R. J. Ram. Fabrication of patterned media for high density magnetic storage. *Journal of Vacuum Science & Technology B: Microelectronics and Nanometer Structures*, 17(6):3168, 1999.

[100] J Köhler, M Albrecht, C.R Musil, and E Bucher. Direct growth of nanostructures by deposition through an Si3N4 shadow mask. *Physica E: Low-dimensional Systems and Nanostructures*, 4(3):196–200, July 1999.

[101] O Vazquez-Mena, L G Villanueva, V Savu, K Sidler, P Langlet, and J Brugger. Analysis of the blurring in stencil lithography. *Nanotechnology*, 20(41):415303, October 2009.

[102] A Linklater and J Nogami. Defining nanoscale metal features on an atomically clean silicon surface with a stencil. *Nanotechnology*, 19(28):285302, July 2008.

[103] Shawn Fostner, Sarah A. Burke, Jessica Topple, Jeffrey M. Mativetsky, Jean Beerens, and Peter Grutter. Silicon nanostencils with integrated support structures. *Microelectronic Engineering*, 87(4):652–657, April 2010.

[104] G.M. Kim, M.A.F. van den Boogaart, and J Brugger. Fabrication and application of a full wafer size micro/nanostencil for multiple length-scale surface patterning. *Microelectronic Engineering*, 67-68:609–614, June 2003.

[105] Stefan Egger, Adelina Ilie, Yiton Fu, Jeffrey Chongsathien, Dae-Joon Kang, and Mark E Welland. Dynamic shadow mask technique: a universal tool for nanoscience. *Nano letters*, 5(1):15–20, January 2005.

[106] L. Gross, R. R. Schlittler, G. Meyer, a. Vanhaverbeke, and R. Allenspach. Fabrication of ultrathin magnetic structures by nanostencil lithography in dynamic mode. *Applied Physics Letters*, 90(9):093121, 2007.

[107] Percy Zahl, Martin Bammerlin, Gerhard Meyer, and Reto R. Schlittler. All-in-one static and dynamic nanostencil atomic force microscopy/scanning tunneling microscopy system. *Review of Scientific Instruments*, 76(2):023707, 2005.

[108] W. T. Tsang and A. Y. Cho. Molecular beam epitaxial writing of patterned GaAs epilayer structures. *Applied Physics Letters*, 32(8):491, 1978.

[109] R Alvarezsanchez, J Costakramer, and F Briones. Analytical model for shape anisotropy in thin-film nanostructured arrays: Interaction effects. *Journal of Magnetism and Magnetic Materials*, 307(2):171–177, December 2006.

[110] EY Tsymbal. Theory of magnetostatic coupling in thin-film rectangular magnetic elements. *Applied Physics Letters*, 77(17):2740, 2000.

[111] RA Pollak and CH Bajorek. Surface composition and chemistry of evaporated Permalloy films observed by x-ray photoemission spectroscopy and by Auger electron spectroscopy. *Journal of Applied Physics*, 46(3):1382–1388, 1975.

[112] M.D. Cooke, D.A. Allwood, and D. Atkinson. Thin single layer materials for device application. *... and magnetic materials*, 257(2-3):387–396, February 2003.

[113] P. Potapov, S. Kulkova, D. Schryvers, and J. Verbeeck. Structural and chemical effects on EELS L3,2 ionization edges in Ni-based intermetallic compounds. *Physical Review B*, 64(18):184110, October 2001.

[114] K. R. Carson. Composition Gradients in NiFe Alloy Films Produced by Vapor Deposition from a Tungsten Boat. *Journal of Vacuum Science and Technology*, 7(6):573, November 1970.

[115] B. Fultz and J.M. Howe. *Transmission Electron Microscopy and Diffractometry of Materials*. Springer Berlin Heidelberg, Berlin, Heidelberg, 2008.

[116] V. F. Bochkarev and E. Yu. Buchin. The effect of electromagnetic fields on the process of formation of ultrathin Fe-Ni films during their deposition under a plasma-stimulated deposition. *Russian Microelectronics*, 38(3):165–170, May 2009.

[117] Sascha Sadewasser and Thilo Glatzel, editors. *Kelvin Probe Force Microscopy*, volume 48 of *Springer Series in Surface Sciences*. Springer Berlin Heidelberg, Berlin, Heidelberg, 2012.

[118] Jeffrey M. Mativetsky, Yoichi Miyahara, Shawn Fostner, Sarah a. Burke, and Peter Grutter. Use of an electron-beam evaporator for the creation of nanostructured pits in an insulating surface. *Applied Physics Letters*, 88(23):233121, 2006.

[119] T Jones, J Sawler, and D. Venus. Simple, calibrated deposition monitor incorporated into an electron beam evaporator. *Review of Scientific Instruments*, 64(7):2008, 1993.

[120] J Ingo Flege, Axel Meyer, Jens Falta, and Eugene E. Krasovskii. Self-limited oxide formation in Ni(111) oxidation. *Physical Review B*, 84(11):10, September 2011.

[121] H. V. Atkinson. A review of the role of short-circuit diffusion in the oxidation of nickel, chromium, and nickel-chromium alloys. *Oxidation of Metals*, 24(3-4):177–197, October 1985.

[122] Henri Jansen, Han Gardeniers, Meint De Boer, Miko Elwenspoek, and Jan Fluitman. A survey on the reactive ion etching of silicon in microtechnology. *Journal of Micromechanics and Microengineering*, 6(1):14–28, March 1996.

[123] N Chekurov, K Grigoras, a Peltonen, S Franssila, and I Tittonen. The fabrication of silicon nanostructures by local gallium implantation and cryogenic deep reactive ion etching. *Nanotechnology*, 20(6):065307, February 2009.

[124] M Schneider, H Hoffmann, and J Zweck. Magnetisation reversal of thin submicron elliptical permalloy elements. *Journal of Magnetism and Magnetic Materials*, 257(1):1–10, February 2003.

[125] Asylum Research SC-35-M. http://www.asylumresearch.com/Probe/SC-35-M, SmartTip, 2013.

[126] Oscar Iglesias-Freire, Jeffrey R. Bates, Yoichi Miyahara, Agustina Asenjo, and Peter H. Grutter. Tip-induced artifacts in magnetic force microscopy images. *Applied Physics Letters*, 102(2):022417, 2013.

[127] Xi Nan, C R Sullivan, and Charles R Sullivan. An Improved Calculation of Proximity-Effect Loss in High-Frequency Windings of Round Conductors. (June):853–860, 2003.

[128] F. Tourkhani and P. Viarouge. Accurate analytical model of winding losses in round Litz wire windings. *IEEE Transactions on Magnetics*, 37(1):538–543, 2001.

[129] C.R. Sullivan. An equivalent complex permeability model for litz-wire windings. *Fourtieth IAS Annual Meeting. Conference Record of the 2005 Industry Applications Conference, 2005.*, 3:2229–2235, 2005.

[130] A Reatti and F. Grasso. Solid and Litz-wire winding non-linear resistance comparison. In *Proceedings of the 43rd IEEE Midwest Symposium on Circuits and Systems (Cat.No.CH37144)*, volume 1, pages 466–469. IEEE, 2000.

[131] R. M. Bozorth. Demagnetizing Factors of Rods. *Journal of Applied Physics*, 13(5):320, 1942.

[132] Roger Proksch, Ken Babcock, and Jason Cleveland. Magnetic dissipation microscopy in ambient conditions. *Applied Physics Letters*, 74(3):419, 1999.

[133] Y Liu and P. Grutter. Magnetic dissipation force microscopy studies of magnetic materials. *Journal of applied physics*, 83(11):7333–7338, 1998.

[134] M Roseman and P Gru. Magnetic imaging and dissipation force microscopy of vortices on superconducting Nb films. 188:416–420, 2002.

[135] Zhenghua Li, Kodai Hatakeyama, Genta Egawa, Satoru Yoshimura, and Hitoshi Saito. Stroboscopic imaging of an alternating magnetic field from a perpendicular magnetic recording head by frequency-modulated magnetic force microscopy. *Applied Physics Letters*, 100(22):222405, 2012.

[136] Wei Lu, Zhenghua Li, Kodai Hatakeyama, Genta Egawa, Satoru Yoshimura, and Hitoshi Saito. High resolution magnetic imaging of perpendicular magnetic recording head using frequency-modulated magnetic force microscopy with a hard magnetic tip. *Applied Physics Letters*, 96(14):143104, 2010.

[137] H. Saito, H. Ikeya, G. Egawa, S. Ishio, and S. Yoshimura. Magnetic force microscopy of alternating magnetic field gradient by frequency modulation of tip oscillation. *Journal of Applied Physics*, 105(7):07D524, 2009.

[138] Hitoshi Saito, Wei Lu, Kodai Hatakeyama, Genta Egawa, and Satoru Yoshimura. High frequency magnetic field imaging by frequency modulated magnetic force microscopy. *Journal of Applied Physics*, 107(9):09D309, 2010.

[139] Hitoshi Saito, Jin Chen, and Shunji Ishio. Principle of magnetic field analysis by MFM signal transformation and its application to magnetic recording media. *Magnetics, IEEE Transactions on*, 35(5):3992–3994, 1999.

[140] Christopher R. Pike, A.P. Andrew P. Roberts, and Kenneth L. K.L. Verosub. Characterizing interactions in fine magnetic particle systems using first order reversal curves. *Journal of Applied Physics*, 85(9):6660, 1999.

[141] C. Pike and A. Fernandez. An investigation of magnetic reversal in submicron-scale Co dots using first order reversal curve diagrams. *Journal of Applied Physics*, 85(9):6668, 1999.

[142] F. Bearon, L. Clime, M. Ciureanu, D. Menard, RW Cochrane, and A. Yelon. First-Order Reversal Curves Diagrams of Ferromagnetic Soft Nanowire Arrays. *ieeexplore.ieee.org*, 42(10):3060–3062, 2006.

[143] Fanny Béron, David Ménard, and Arthur Yelon. First-order reversal curve diagrams of magnetic entities with mean interaction field: A physical analysis perspective. *Journal of Applied Physics*, 103(7), 2008.

[144] D. Ozkaya L, R. M. Langford, W. L. Chan, and a. K. Petford-Long. Effect of Ga implantation on the magnetic properties of permalloy thin films. *Journal of Applied Physics*, 91(12):9937, 2002.

[145] MCB Parish and M. Forshaw. Magnetic cellular automata (MCA) systems. *IEE Proceedings-Circuits, Devices and Systems*, 151(5):480–485, 2004.

[146] A Imre, G Csaba, L Ji, A Orlov, GH H Bernstein, and W Porod. Majority Logic Gate for Magnetic Quantum-Dot Cellular Automata. *Science (New York, N.Y.)*, 311(January):205–208, 2006.

[147] Percy Zahl, Thorsten Wagner, Rolf Moller, and Andreas Klust. Open source scanning probe microscopy control software package GXSM. *Journal of Vacuum Science & Technology B: Microelectronics and Nanometer Structures*, 28(3):C4E39, 2010.

[148] Percy Zahl, Markus Bierkandt, Stefan Schroder, and Andreas Klust. The flexible and modern open source scanning probe microscopy software package GXSM. *Review of Scientific Instruments*, 74(3):1222, 2003.

[149] Yanzhang Liu. *Magnetic Dissipation Force Microscopy*. PhD thesis, McGill University, 1997.

[150] ÁM Bueno, JM Balthazar, and JRC Piqueira. Phase-locked loop application to frequency modulation - Atomic Force Mirroscope. *Proceedings of the 9th Brazilian Conference on Dynamics, Control and their Applications*, pages 343–348, 2010.